Depth Discrimination of an Acoustic Source Based on Modal Energy Distribution

by

Yan Apelfeld

B.Sc.T.E., Electrical Engineering (1996)
Tel Aviv University
Submitted to the Department of Mechanical Engineering
in partial fulfillment of the requirement for the degree of

Master of Science in Ocean Engineering
at the
Massachusetts Institute of Technology

February 2007

Signature of author.....

Department of Mechanical Engineering

January 7, 2007

Certified by.....

Professor Henrik Schmidt

Professor of Mechanical and Ocean Engineering

Thesis Supervisor

Accepted by.....

Professor Lallit Anand

Chairman, Department Committee on Graduate Students

Depth discrimination of an acoustic source based on modal energy distribution

by

Yan Apelfeld

Submitted to the Department of Mechanical Engineering
in partial fulfillment of the requirement for the degree of

Master of Science in Ocean Engineering

Abstract

The new method of acoustic source depth discrimination in a shallow water environment is investigated. The investigation is concentrated mainly in 500Hz and 1kHz sources in the range-independent and range-dependent environments. Efficiency and robustness of the method is studied and suggestions for the method's optimization are provided.

The results of many simulation cases are presented and discussed. The results suggest that for the sources of 500Hz and 1kHz the depth discrimination method can provide an accurate estimate of the target's type: surface or submerged. The method can be useful for applications for which exact depth location is unnecessary and a target's category estimate is sufficient. The method is based on the fact that the modal energy distribution changes in accordance with a source depth category. Guidelines to achieve correct results are developed and presented. Method stability and robustness are examined.

The range-independent case results suggest existence of 'shadow' areas where the standard method may provide a misleading depth estimate. Alternative methods are suggested to overcome the problem.

The range-dependent case results suggest relatively poor performances of the method for a downslope environment. However, the upslope case results show superior performances than even in the range-independent case.

Thesis Supervisor: Professor Henrik Schmidt

Title: Professor of Mechanical and Ocean Engineering

Acknowledgments

This part of the work probably will be the hardest one. There are so many people to thank and yet I have to include it in a relatively small number of sentences.

I want to start by expressing my sincere appreciation to Prof. Henrik Schmidt, my advisor, for leading me through my thesis research. Thank you for making it so intellectually pleasant experience and for giving me such a wonderful opportunity to study so interesting subject. I was amazed by your personality and professional skills. Even now after knowing you for almost 18 months it is still difficult for me to apprehend that human mind can be so productive in so many areas. I was really lucky to work under your guidance.

I want to thank Prof. Nicholas C. Makris for introducing me a world of acoustics. Thank you for making it so insightful and diverse. Usually the first experiences are the strongest one and based on them our future attitude is defined . You definitely made me to love this subject!

My special thanks to Prof. Arthur Baggeroer and Dr. James Lynch for helping me to study so much in such a short period of time. I wouldn't believe that it can be possible if it wasn't happened to me.

I thankful for the opportunity to be surrounded by so many talented students. Our discussions were so helpful and enlighten so many times. I think that you are making MIT so unique place.

My sincere appreciations to all Israel Navy's officers that trusted me and helped me to get such a wonderful opportunity to study so interesting subject from some of the brightest minds in this scientific area. I thankful to Rear Admiral Omri Dagul for your trust and for your letter of recommendation, to Captain Yoav Turgeman and Captain Itzhak Maya for your trust and your efforts, to Commander Sappir Goren for your understanding and your tremendous help to fulfill my dream, to Commander Shlomi Azar to letting me in your 'closed' community, to Lt. Commander Eran Naftali and Lt. Commander Omri Pedatzur for your help and friendly advice.

I would like to thank to Prof. Yakov Gavan and Prof. Gadi Golan for your recommendation letters and above all for providing me necessary scientific skills. Without them I wouldn't write these lines.

And now lines of admire to most important person in my life, my own discovery, my miracle, my lovely wife Ilana. I completely sure and no one can't convince me in otherwise, without your support I couldn't do it. Only you know about all the tiny crisis's that you was able to run away from me. I can only be thankful to God to having you by my side. You are my island of sanity. You are my protecting shield. You are my Magen David!!!

Contents

List of Figures

List of Tables

Chapter 1

Introduction

This research has been motivated by a need for a robust classification method of acoustic sources. Robust classification clues can reduce false alarms. This is particularly critical in autonoumos systems, where is a succesful target classification will prevent unnecessary execution cycles.

Acoustic source localization in the ocean waveguide is a subject that has been discussed widely by the acoustic community. Different methods and approaches to the source location estimation have been suggested[1, 2, 3, 4]. The methods can be generally split in two main categories.

The first category has been based on the modal decomposition or the mode filtering of the pressure field at the receiver location[1, 2]. By using a normal mode theory expression for the pressure field which includes source location information and relies on normal modes' orthogonality, a source position could be retrieved from the received pressure field. All this based on the assumption that normal modes functions could be calculated.

The second category of methods has been based on Matched Field Processing theory[3, 4]. By using various propagation models a theoretical pressure field estimate for different source locations can be calculated. The best match (maximum correlation) between the received and the calculated pressure will indicate the source location. In both cases the precise waveguide geometry and the environmental data estimate such as a sound speed profile are necessary to make an accurate estimate of the source location.

Although complete information about a source location such as bearing, range and depth are of major interest in many applications, there are some areas in which the first degree estimate is needed. So it will be possible to categorize sources into submerged or surface targets. One of these areas is AUV applications for which target legitimacy recognition as a submerged or surface source could be extremely useful.For these AUV operational scenarios a fast estimation method is required as a substitute to the classic depth estimate approach. The requirement of the source depth allocation is exchanged by the requirement to categorize the target as a submerged or surface source.

In the current chapter the main idea behind the discrete depth estimation technique will be introduced. The research goals and the thesis structure will also be presented.

1.1 Background

As was already mentioned before, a relatively fast technique for the source discrete depth estimation is required. Although the classic approach of modal decomposition or MFP (Matched Field Processing) could be used for this purpose as well, there is no need in the exact depth location estimation. Therefore to apply these classic techniques to the problem in some sense could be described as an overuse of computational resources.

The basic idea for the discrete depth estimation is based on the assumption that a submerged source in a shallow water environment will excite more low modes than the surface source. This assumption will be shown as true in the next chapters by presenting simulation results of pressure field analysis based on a KRAKEN propagation model [5]. If the assumption is true, the relationship between the energy which concentrated in the low order and high order modes could be an indicator of the source location. Therefore by calculating this relationship which will be defined as a submergence index (SI) we can evaluate if the

source is submerged or not. Although the idea of SI can be very useful for our discussion it is incomplete as long as there is a need to make modal decomposition of the total pressure field as a part of the decision making about source depth. Therefore a different approach to analyze received pressure field is required.

Every normal mode function can be represented as a pair of quasi-plane waves propagating with some specific grazing angle (to the horizontal plane of propagation). The propagation angle is directly related to a mode number[6]. H.V. Chouchan used the same property to filter out unnecessary modes by steering the nulls of the array to their direction[7]. A plane wave representation of each mode can be very useful for SI calculations and can allow us to avoid the mode filtering process. Instead of a modal analysis of the pressure field, propagation angles distribution will be used as a base for SI calculations.

For applications of the current thesis interest a towed horizontal array will be the preferred choice for the target (acoustic source) detection and estimation. Under assumptions of equally spaced hydrophones of approximately half wavelength distance to satisfy appropriate spatial spacing requirements and assuming source location close to the array end-fire, the general procedure for SI calculation will be as follows:

- make pressure field measurements at specific array depth
- apply relatively smooth window function to suppress steep grazing angles contribution to the total field
- apply relatively smooth window function to suppress shallow grazing angles contribution to the total field
- calculate averaged ratio of two post-windowing results (pre-averaged SI result)
- repeat the steps for different array depth (sample the water-column in pre-defined depth values)
- calculate final submergence index (SI) value by the averaging all pre-averaged SI results
- categorize target depth based on the SI value.

Although the suggested above algorithm is relatively simple, many issues should be resolved to make it applicable. One of these issues is the averaging requirement. The optimal number of stratifying levels should be defined to give the correct result on one hand and to minimize processing time on the other. The surface target depth should be defined as a function of the wavelength so it will be a frequency dependent parameter. The criteria for the splitting angle space should be found in order to assure appropriate separation between a submerged and surface target. The influence of different windowing functions should be checked. It is also crucial to check the robustness of the algorithm for a variety of frequencies. As a number of modes in a water-column will increase with higher frequencies some effects of constructive/ destructive interference could be expected. Range dependent environment cases, specially wave propagation along a downslope/ upslope bottom, could be interesting study cases assuming mode coupling in the wedge environment[8, 9].

These issues will be discussed in the next chapters.

1.2 Thesis outline.

In chapter 2 of the thesis mathematical derivation of the modal theory will be summarized and other concepts such as array steering, modal energy conversion or mode coupling will be introduced. The main physical aspects of shallow water acoustics will be discussed.

In chapter 3 the numerical simulations results will be presented. The results will support the main assumption concerning dependence of modal energy distribution and depth location in the water-column. Parameter settings that were used to stabilize previously introduced algorithm will be described. The simulation results which will be extensively presented will indicate that the algorithm is robust enough for various geometry arrangements and for diverse environmental parameters. Source frequency influence on the results of calculations and some specific scenarios will be discussed in depth, including analysis based on the normal mode theory.

In chapter 4 range dependent shallow water environment cases will be discussed in the presence of the wedge-shaped bottom. Specific parts of the chapter will be dedicated to the mode coupling effect on SI calculations. Criteria for geometric limitations on the slope angles will be defined based on the simulation

results. Cases of slope angles will be presented and will be compared to a perfectly horizontal ocean bottom. The differences would be studied and explored using mode coupling theory.

In chapter 5 summary and conclusions of the research will be presented and applications will be discussed.

Chapter 2

Shallow water wave propagation, normal modes.

In the current chapter we will summarize the concepts of shallow water acoustics by using method of the normal modes as a mathematical representation of the pressure field in a water-column. We will describe

two common models of the shallow water environment: the hard bottom case and Pekeris waveguide. The Lloyd mirror effect will be discussed briefly.

2.1 Normal modes for perfectly reflecting (hard) bottom case

We could start the normal mode method derivation by using mathematical approach which is based on a solution of the two dimensional Helmholtz equation for the radial symmetry case. But it will be more appropriate to start with a more intuitive physical approach. Brekhovskikh and Lysanov[6], and Officer[10] have shown the physical aspects of the problem in their books. We will use Brekhovskikh and Lysanov approach in our discussion.

We begin from a case of an omnidirectional point source emitting a spherical wave which is propagating into a halfspace (no bottom boundary) and can be represented in a simplified form (time dependence suppressed) as a superposition of plane waves

$$p = \frac{1}{r}\exp(ikr) = \frac{i}{2\pi}\int\int_{-\infty}^{\infty}\frac{1}{k_z}\exp\left[i\left(k_x x + k_y y + k_z z\right)\right]dk_x dk_y \tag{2.1}$$

where $r = \sqrt{(x^2+y^2+z^2)}$ and $k_x, k_y, k_z$are wavenumber components in the direction of axis x, y, z respectively. The expression 2.1 is true if the source located at the origin.

Now we will change the geometry and add a bottom boundary at $z = h$, where is an h is a water-column depth. The source will be relocated from the origin to the depth $z_0$and $z_0 > z$, so the source location is deeper than the receiver . This will change the general expression for the propagating wave to the receiver directly to the $\exp\left[i\left(k_x x + k_y y + k_z(z_0 - z)\right)\right]$.But the bottom boundary will be a reflection surface for the propagation wave and the expression for a bottom single-interacted wave will be $R\exp\left[i\left(k_x x + k_y y + k_z(2h - z_0 - z)\right)\right]$, where R is a reflection coefficient with the bottom boundary and it's a function of the incidence angle, the bottom and the water properties. We will assume a top boundary to be a pressure release surface which is a good approximation for the air-water interface. Based on this assumption the $R = -1$ (phase change of π), so the top reflected way is $-\exp\left[i\left(k_x x + k_y y + k_z(z_0 + z)\right)\right]$. Finally the bottom and the top reflected wave will be $-R\exp\left[i\left(k_x x + k_y y + k_z(2h - z_0 + z)\right)\right]$

Since there is an infinite number of top-bottom reflections we can represent it geometrically using the method of images. We are looking at the wavepath projection in z direction as a function of the boundary interaction's number. We can generalize that an additional top-bottom reflection will add $2hk_z$ factor to the phase. Each of the waves (direct and multi-reflected) will contribute to the total pressure at the receiver, so

the pressure field expression will be

$$p(r,z) = \frac{i}{2\pi}\int\int_{-\infty}^{\infty}\frac{1}{k_z}\exp\left[i\left(k_x x + k_y y\right)\right] * \\ * \left\{\exp\left[ik_z\left(z_0 - z\right)\right] + R\exp\left[ik_z\left(2h - z_0 - z\right)\right] - \exp\left[ik_z\left(z_0 + z\right)\right] - R\exp\left[ik_z\left(2h - z_0 + z\right)\right]\right\} * \\ *\sum_{l=0}^{\infty}\left(-R\right)^l\exp\left(ik_z 2hl\right)dk_x dk_y \tag{2.2}$$

The expression 2.2 can be simplified by using a trigonometric expansion property of exponential functions and a formula of infinite trigonometric series

$$p(r,z) = \frac{1}{\pi}\int\int_{-\infty}^{\infty}\frac{1}{k_z}\frac{\exp\left[i\left(k_x x + k_y y\right)\right]\sin k_z z\left\{\exp\left(ik_z z_0\right) + R\exp\left[ik_z\left(2h - z_0\right)\right]\right\}}{1 + R\exp\left(2ik_z h\right)}dk_x dk_y \tag{2.3}$$

Next we substitute parameters (polar coordinates transform) into the 2.3 :
$\xi \equiv \sqrt{k_x^2 + k_y^2}$, $k_x = \xi\cos\varphi$, $k_y = \xi\sin\varphi$, $\alpha \equiv k_z = \sqrt{k^2 - \xi^2}$,
where $\varphi$is an angle of the propagation (90^o to the wavefront) and $x = r\cos\psi$, $y = r\sin\psi$
we will get:

$$p(r,z) = \frac{1}{\pi}\int_0^{2\pi}\int_0^{\infty}\frac{1}{\alpha}\frac{\exp\left[i\xi r\cos\left(\varphi - \psi\right)\right]\sin\alpha z\left\{\exp\left(i\alpha z_0\right) + R\exp\left[i\alpha\left(2h - z_0\right)\right]\right\}}{1 + R\exp\left(2i\alpha h\right)}\xi d\xi d\varphi \tag{2.4}$$

We will use an integral representation of the zero order Bessel function from Abramowitz[11]:
$J_0(x) = \frac{1}{\pi}\int_0^{\pi}\cos\left(z * \sin\theta\right)d\theta$ to simplify the 2.4 to a singe integral form

$$p(r,z) = \int_0^{\infty} 2J_0\left(\xi r\right)\frac{1}{\alpha}\frac{\sin\alpha z\left\{\exp\left(i\alpha z_0\right) + R\exp\left[i\alpha\left(2h - z_0\right)\right]\right\}}{1 + R\exp\left(2i\alpha h\right)}\xi d\xi \tag{2.5}$$

By using relationship between Bessel and Hankel functions $J_0\left(\xi r\right) = \frac{1}{2}\left(H_0^{(1)}\left(\xi r\right) + H_0^{(1)}\left(\xi r\right)\right)$for 2.5 and by rearranging it for a more uniform representation, we are finally getting an integral form expression for the pressure field in a layered water-column:

$$p(r,z) = \int_{-\infty}^{\infty} H_0\left(\xi r\right)\frac{1}{\alpha}\frac{\sin\alpha z\left\{\exp\left[-i\alpha\left(h - z_0\right)\right] + R\exp\left[i\alpha\left(h - z_0\right)\right]\right\}}{\exp\left(-i\alpha h\right)\left[1 + R\exp\left(2i\alpha h\right)\right]}\xi d\xi \tag{2.6}$$

We have to remember that 2.6 has been derived based on the assumption that a source is deeper than a receiver. For an opposite case we just need to replace z with z_0 and vice verse.

Our assumption at the beginning of this chapter was that the bottom is perfectly reflecting surface, so $R = 1$. Therefore the expression 2.6 can be simplified to the

$$p(r,z) = \int_{-\infty}^{\infty} H_0\left(\xi r\right)\frac{\sin\alpha z * \cos\left[\alpha\left(h - z_0\right)\right]}{\alpha\cos\left(\alpha h\right)}\xi d\xi \tag{2.7}$$

We will use Cauchy residues theorem[12] to simplify an expression 2.7 to a summation form. We are looking for poles of the equation

$$\cos\left(\alpha h\right) = 0$$
$$\alpha_n = \frac{\pi}{h}\left(n - \frac{1}{2}\right),\ n = 1, 2, 3...$$

by using a previously defined relation between α and ξ we will get the roots

$$\xi_n = \pm\sqrt{k^2 - \left(\frac{\pi^2}{h^2}\left(n-\frac{1}{2}\right)^2\right)} \tag{2.8}$$

Let's assume that a wavenumber k has a small positive imaginary part, so a small attenuation exists. This assumption will move the roots of the equation, ξ_n, from a real positive and negative axis to a first and third quadrant respectively. We will integrate in the upper half plane. By using Cauchy residues theorem we can simplify 2.7 to a sum of residues.

$$p(r,z) = \frac{2\pi i}{h}\sum_{m=1}^{\infty}\sin(\alpha_n z)\sin(\alpha_n z_0)\,H_0^{(1)}(\xi_n r) \tag{2.9}$$

The expression 2.9 represents a total pressure field as a sum of normal modes for a hard bottom and a soft top case. Usually we are interested in knowing a pressure field expression far away (relatively to the wavelength) from a source location, $\xi_n r \gg 1$. For these cases we can use a first term only of a Hankel function expansion (asymptotic form): $H_0^{(1)}(\xi r) \approx \sqrt{\frac{2}{\pi\xi r}}\exp\left[i\left(\xi r - \frac{\pi}{4}\right)\right]\left[1+\frac{1}{8i\xi r}+...\right]$. An asymptotic form of the 2.9 will be:

$$p(r,z) \approx \frac{2i}{h}\sum_{n=1}^{\infty}\sqrt{\frac{2\pi}{\xi_n r}}\sin(\alpha_n z)\sin(\alpha_n z_0)\exp\left[i\left(\xi_n r - \frac{\pi}{4}\right)\right] \tag{2.10}$$

We can learn from the 2.10 that a total pressure field is a function of a source depth $\sim \sin(\alpha_n z_0)$ (exciting function), a receiver depth and a range to the receiver $\sim \sqrt{\frac{1}{\pi\xi_n r}}\sin(\alpha_n z)\exp\left[i\left(\xi_n r - \frac{\pi}{4}\right)\right]$ (normal mode). A normal mode function can be decomposed to a standing wave at z direction and a propagating at range. Using an exponential form representation for sin function will bring us to a plane wave representation with a propagating angle of $\chi_n = \arcsin\left(\frac{\alpha_n}{k}\right)$ relatively to a horizontal direction:

$$p_n \sim \sqrt{\frac{1}{r}}\left\{\exp\left[i\left(\xi_n r + \alpha_n z\right)\right] - \exp\left[i\left(\xi_n r - \alpha_n z\right)\right]\right\} \tag{2.11}$$

A normal mode representation as a plane wave propagating with specific angle will be very useful for our future discussion.

From 2.11 a normal modes' amplitude will decay with $\frac{1}{\sqrt{r}}$ through a range. We also can conclude that as long as a wavenumber is positive no attenuation in the media is expected, therefore from 2.11 aroused that $\frac{\pi}{kh}\left(n-\frac{1}{2}\right) \geq 1$will be a condition for a non-attenuated mode propagation. By substitute $k = \frac{\omega}{c}$in the previous expression we can define a frequency criteria ("cutoff") for a non-attenuated mode propagation:

$$f_{cutoff_n} = \frac{c}{2h}\left(n-\frac{1}{2}\right) \tag{2.12}$$

After deriving a normal modes expression for a hard bottom case through a intuitive physical approach and exploring some of it's properties, we will discuss in the next section more general form of a normal modes representation by looking for a solution to the wave equation.

2.2 Pekeris waveguide model

A formal derivation of a normal mode representation could be found in many literature sources. We will use a Frisk's [13] derivation form to the wave equation solution. We will assume symmetry in a azimuthal direction and stratified media in a z (vertical) direction. It is natural, under the given conditions, to choose cylindrical coordinates.

2.2.1 Wave equation as Sturm-Liouville problem

We are starting by writing an inhomogeneous wave equation with a source location at $r = 0, \theta = 0, z = z_0$:

$$\rho(z) \bigtriangledown \cdot \left[\frac{1}{\rho(z)} \bigtriangledown p(r,\theta,z)\right] + k^2(z)\, p(r,\theta,z) = -4\pi \frac{\delta(r)}{r}\delta(\theta)\delta(z-z_0) \tag{2.13}$$

which can be simplified to:

$$\frac{1}{r}\frac{\partial}{\partial r}\left[r\frac{\partial p(r,z)}{\partial r}\right] + \frac{\partial^2 p(r,z)}{\partial z^2} + \rho(z)\frac{\partial}{\partial z}\left[\frac{1}{\rho(z)}\right]\frac{\partial p(r,z)}{\partial z} + k^2(z)p(r,z) = -4\pi\frac{\delta(r)}{r}\delta(\theta)\delta(z-z_0)$$

by using a symmetry property to get rid of $\frac{\partial}{\partial\theta}$term and finally by integrating it, we will get

$$\int_0^{2\pi}\left\{\frac{1}{r}\frac{\partial}{\partial r}\left[r\frac{\partial p(r,z)}{\partial r}\right] + \frac{\partial^2 p(r,z)}{\partial z^2} + \rho(z)\frac{\partial}{\partial z}\left[\frac{1}{\rho(z)}\right]\frac{\partial p(r,z)}{\partial z} + k^2(z)p(r,z)\right\} =$$
$$= \int_0^{2\pi}\left\{-4\pi\frac{\delta(r)}{r}\delta(\theta)\delta(z-z_0)\right\}$$
$$\frac{1}{r}\frac{\partial}{\partial r}\left[r\frac{\partial p(r,z)}{\partial r}\right] + \frac{\partial^2 p(r,z)}{\partial z^2} + \rho(z)\frac{\partial}{\partial z}\left[\frac{1}{\rho(z)}\right]\frac{\partial p(r,z)}{\partial z} + k^2(z)p(r,z) = -2\frac{\delta(r)}{r}\delta(z-z_0)$$

We will not try to be mysterious about the next steps...We are looking for some way to represent 2.13 in the Sturm-Liouville problem form which defined in [14] as:

$$\mathcal{L}u(x) + \lambda w(x)u(x) = 0 \tag{2.14}$$

, where $\mathcal{L}$ is a linear second order differential operator defined by $\mathcal{L}u(x) = s_0(x)u_{xx} + s_1(x)u_x + s_2(x)u$, and $s_{0/1/2}$are functions of x.

The most known way to show that the 2.13 fits the 2.14 form is by using separation of variables. The technique is well described in Arfken[14]. We are switching to a homogeneous form of the equation:

$$\frac{1}{r}\frac{\partial}{\partial r}\left[r\frac{\partial p(r,z)}{\partial r}\right] + \frac{\partial^2 p(r,z)}{\partial z^2} + \rho(z)\frac{\partial}{\partial z}\left[\frac{1}{\rho(z)}\right]\frac{\partial p(r,z)}{\partial z} + k^2(z)p(r,z) = 0 \tag{2.15}$$

The solution to the 2.15 is assumed to be of the form $p(r,z) = \Phi(r)\Psi(z)$, so if we substitute the last to the 2.15 we will get:

$$\frac{\Psi}{r}\frac{d}{dr}\left[r\frac{d\Phi}{dr}\right] + \Phi\frac{d^2\Psi}{dz^2} + \rho\Phi\frac{d}{dz}\left[\frac{1}{\rho(z)}\right]\frac{d\Psi}{dz} + k^2\Phi\Psi = 0$$

All partial derivatives became full derivatives. Dividing by $\Phi\Psi$will give us:

$$\frac{1}{\Phi r}\frac{d}{dr}\left[r\frac{d\Phi}{dr}\right] + \frac{1}{\Psi}\frac{d^2\Psi}{dz^2} + \rho\frac{1}{\Psi}\frac{d}{dz}\left[\frac{1}{\rho(z)}\right]\frac{d\Psi}{dz} + k^2 = 0$$
$$\frac{1}{\Psi}\frac{d^2\Psi}{dz^2} + \rho\frac{1}{\Psi}\frac{d}{dz}\left[\frac{1}{\rho(z)}\right]\frac{d\Psi}{dz} + k^2 = -\frac{1}{\Phi r}\frac{d}{dr}\left[r\frac{d\Phi}{dr}\right]$$

The last expression is defined by Arfken[14] as a "paradox", because we have on the LHS a $f(z)$ that equal to a $f(r)$ on the RHS. The only way that the equality can be satisfied if both sides are equal to a constant value, so we are getting a separable solution with a separation constant k_n^2.

$$\frac{1}{\Psi}\frac{d^2\Psi}{dz^2} + \rho\frac{1}{\Psi}\frac{d}{dz}\left[\frac{1}{\rho}\right]\frac{d\Psi}{dz} + k^2 = k_{rn}^2$$
$$\frac{1}{\rho}\frac{d^2\Psi}{dz^2} + \frac{d}{dz}\left[\frac{1}{\rho}\right]\frac{d\Psi}{dz} + \frac{1}{\rho}\Psi k^2 - \frac{1}{\rho}\Psi k_{rn}^2 = 0$$

Let's define a relation $k_{zn}^2 = k^2 - k_{rn}^2$ that will rearrange the solution to the Sturm-Liouville form with eigenfunction $\Psi(z)$

$$\frac{1}{\rho(z)}\frac{d^2\Psi}{dz^2} + \frac{d}{dz}\left[\frac{1}{\rho(z)}\right]\frac{d\Psi}{dz} + \frac{\omega^2}{c^2(z)\rho(z)}\Psi - \frac{k_{rn}^2}{\rho(z)}\Psi = 0 \tag{2.16}$$

where an operator $\mathcal{L}$ is

$$\mathcal{L} = \frac{1}{\rho(z)} + \frac{d}{dz}\left[\frac{1}{\rho(z)}\right] + \frac{\omega^2}{c^2(z)\rho(z)} \tag{2.17}$$

a weighting function is

$$w(z) = \frac{1}{\rho(z)} \tag{2.18}$$

and a eigenvalue

$$\lambda = k_{rn}^2 \tag{2.19}$$

We should also notice from the 2.17 expression that $s_1(z) = \frac{ds_0}{dz}$, so a condition for $\mathcal{L}$ to be a self-adjoint operator is satisfied.

Now we can use all the known properties of the Sturm-Liouville problem. Two facts to keep in mind that there is an infinite number of solutions $\Psi_n(z)$ which are described as normal modes (eigenfunctions) and eigenvalues$k_{rn}^2$are positive. For the m mode within watercolumn $0 < z < h$ will be m zero crossings of eigenfunction $\Psi_n(z)$.

The modes are orthonormal to each other:

$$\int_0^h w(z)\Psi_m(z)\Psi_n(z)dz = \int_0^h \frac{1}{\rho(z)}\Psi_m(z)\Psi_n(z)dz = \delta_{nm} = \begin{cases} 1, & m = n \\ 0, & m \neq n \end{cases} \tag{2.20}$$

Modes create complete set of solutions:

$$p(r,z) = \sum_{n=1}^{\infty} \Phi_n(r)\Psi_n(z) \tag{2.21}$$

Modes satisfy closure relationship:

$$\sum_{n=1}^{\infty} w(z_0)\Psi_n(z_0)\Psi_n(z) = \delta(z - z_0) \tag{2.22}$$

We will substitute a 2.21 relationship back into the inhomogeneous form of a 2.13 and we will use the properties of Sturm-Liouville problem as a 2.20 and a 2.22 to get

$$\frac{1}{r}\frac{d}{dr}\left[r\frac{d\Phi_n(r)}{dr}\right] + k_{rn}^2\Phi_n(r) = -2\frac{\delta(r)\Psi_n(z_0)}{r\rho(z_0)} \tag{2.23}$$

The equation 2.23 has a standard solution $\Phi_n(r) = \frac{i\pi}{2\rho(z_0)}\Psi_n(z_0)H_0^{(1)}(k_{rn}r)$, where $H_0^{(1)}(k_{rn}r)$ is the Hankel function that was already described in the previous section. The final form will be

$$p(r,z) = \frac{i\pi}{2\rho(z_0)}\sum_{n=1}^{\infty} \Psi_n(z_0)\Psi_n(z)H_0^{(1)}(k_{rn}r) \tag{2.24}$$

in which $\Psi_n(z)$ is a normal mode expression and $\Psi_n(z_0)$ is a modal exciting function. We got the same expression as it was already derived before using an integral representation of the field.

The asymptotic form of Hankel function will give us expression for a far away (by the means of the wavelength) from a source case

$$p(r,z) \sim \frac{\sqrt{2\pi}\exp\left(\frac{i\pi}{4}\right)}{\rho(z_0)}\sum_{n=1}^{\infty} \Psi_n(z_0)\Psi_n(z)\frac{\exp(ik_{rn}r)}{\sqrt{k_{rn}r}} \tag{2.25}$$

2.2.2 Boundary conditions

We will adopt now a Pekeris waveguide model into our discussion. The model includes a top pressure-release surface, a water-column and a higher velocity/density ($\rho_1 > \rho$, $c_1 > c$) half-space bottom. Top boundary conditions are the same as it was in 2.1. Bottom boundary conditions are different, therefore we can't use $R = 1$ as a reflection coefficient. R value in the current case will be a function of a wave incident angle θ. The whole angle space will be split by a value of the critical angle $\theta_c = \arcsin\left(\frac{c}{c_1}\right)$. The angle space above the critical angle (closer to a normal incident) will be defined as continuous and below the critical angle as discrete. Although the final representation of the pressure field includes contribution from each of the two subspaces, we are mainly interested in the discrete spectrum of so called trapped modes only. The reason for this is a high decaying rate of the continuum modes due high energy losses into a halfspace. Relied on the final applicability considerations we will discuss here only a trapped modes case.

For the modes with propagating grazing angles below the critical angle a reflection coefficient $|R| = 1$. A phase of an R is equal to $\varphi = -2\arctan\left[\frac{\sqrt{\sin^2\theta - \frac{c^2}{c_1}}}{\frac{\rho_1}{\rho}}\right]$. These modes are trapped inside a water-column as in a waveguide. With each interaction of a trapped wave with a bottom the phase will be changed by the φ. We can recall that for n modes in the hard bottom case a phase term gave us equality of

$$k_{zn}h - \frac{\pi}{2} = (n-1)\pi,\ n = 1, 2, 3...$$

A phase change due interaction with a higher velocity bottom requires modification in a phase part of the expression, so for the trapped modes of a Pekeris model the expression will be

$$k_{zn}h - \frac{\pi}{2} + \frac{\varphi}{2} = (n-1)\pi,\ n = 1, 2, 3...$$

and the vertical wavenumber component will be

$$k_{zn} = \frac{1}{h}(n - \frac{1}{2})\pi - \frac{\varphi}{2},\ n = 1, 2, 3... \tag{2.26}$$

As a next step we are looking for a pressure expression contributed by the trapped modes that will satisfy the wave equation. We are defining eigenfunctions in a water-column and into a bottom half-space as

$$\Psi_n(z) = \begin{cases} A_n \sin(k_{zn}z), & 0 \le z \le h \\ B_n \exp(-k_{1zn}z), & z \ge h \end{cases} \tag{2.27}$$

where $k_{1zn} = \sqrt{k_{rn}^2 - k_1^2}$and $k_{rn} = \sqrt{k^2 - k_{zn}^2}$, so $k_{1zn}$is the vertical wavenumber in the bottom halfspace. A pressure continuity at the boundaries is required, therefore for a bottom boundary

$$\begin{aligned} A_n \sin(k_{zn}h) &= B_n \exp(-k_{1zn}z) \\ B_n &= A_n \sin(k_{zn}h)\exp(-k_{1zn}h) \end{aligned} \tag{2.28}$$

We will find the orthonormal property very useful for eigenfunctions of a Sturm-Liouville problem for a next step. Let's recall an expression 2.20:

$$\int_0^h \frac{1}{\rho(z)}\Psi_m(z)\Psi_n(z)dz = \delta_{nm} = \begin{cases} 1, & m = n \\ 0, & m \ne n \end{cases}$$

In the current case will be two regions of integration, the first through a water-column and the second into a bottom halfspace. By using an orthonormality and a pressure continuity as a boundary condition expressed by 2.28 we can find an amplitudeA_n

$$\int_0^h \frac{1}{\rho} A_n^2 \sin^2(k_{zn} z)\, dz + \int_h^\infty \frac{1}{\rho} B_n^2 \exp(-2k_{1zn} z)\, dz = 1$$

$$\frac{A_n^2}{\rho} \int_0^h \sin^2(k_{zn} z)\, dz + \frac{A_n^2 \sin^2(k_{zn} h)}{\rho \exp(2k_{1zn} h)} \int_h^\infty \exp(-2k_{1zn} z)\, dz = 1$$

$$A_n = \sqrt{2\left[\frac{1}{\rho}\left(h - \frac{\sin 2k_{zn} h}{2k_{zn}}\right) + \frac{1}{\rho_1}\frac{sin^2 k_{zn} h}{k_{1zn}}\right]}$$

Now we can define a pressure field p_t contributed by modes trapped into the water-column. Using already developed expression for a Sturm-Liouville problem we can write:

$$p_t(r,z) = \begin{cases} \frac{i\pi}{\rho} \sum_{n=1}^{n_{max}} A_n^2 \sin(k_{zn} z_0) \sin(k_{zn} z)\, H_0^{(1)}(k_{nr} r), & 0 \le z \le h \\ \frac{i\pi}{\rho} \sum_{n=1}^{n_{max}} A_n^2 \sin(k_{zn} z_0) \sin(k_{zn} h) \exp(k_{1zn} h - k_{1zn} z)\, H_0^{(1)}(k_{nr} r), & z \ge h \end{cases} \tag{2.29}$$

The n_{max}term in upper limit of a summation is equal to a highest mode number that will propagate with a grazing angle less than the critical (modes with a steeper angle than the critical are defined as "leaking" modes and they are out of our scope of interest in the current discussion).

Pressure field contributed by the trapped modes 2.29 gives us a relatively good approximation for the pressure value in different ranges, though it was already mentioned before that we are interested in cases where $k_{rn} r \gg 1$. Therefore an asymptotic form of the 2.29 will be more useful:

$$p(r,z) \sim \begin{cases} \frac{\sqrt{2\pi}\exp\left(\frac{i\pi}{4}\right)}{\rho} \sum_{n=1}^{n_{max}} A_n^2 \sin(k_{zn} z_0) \sin(k_{zn} z) \frac{\exp(ik_{rn} r)}{\sqrt{k_{rn} r}}, & 0 \le z \le h \\ \frac{\sqrt{2\pi}\exp\left(\frac{i\pi}{4}\right)}{\rho} \sum_{n=1}^{n_{max}} A_n^2 \sin(k_{zn} z_0) \sin(k_{zn} h) \exp(k_{1zn} h - k_{1zn} z) \frac{\exp(ik_{rn} r)}{\sqrt{k_{rn} r}}, & z \ge h \end{cases} \tag{2.30}$$

Before we will continue our discussion about main properties of the pressure field it could noticed that the field has an exponentially decaying behavior into the bottom half-space.

Let's go through some of the main properties of the Pekeris waveguide briefly by analyzing recently derived equations.

- Zero crossing locations of the eigenfunctions (nodes) will be more dense in the top boundary area comparing to the hard bottom case and will be defined as

$$z_{zero-cross} = \frac{m\pi h}{\left[\left(n - \frac{1}{2}\right)\pi - \frac{\varphi}{2}\right]},\ m = 0, 1, 2..,\ z_{zero-cross} < h \tag{2.31}$$

  A nodes location is quite important for our future discussion. A source location in the node area will produce highly attenuated pressure field. It is also immediately seen from the 2.31 that as a propagating angle is approaching to the $0^0$the nodes location is getting closer to the hard bottom case.

- The number of the propagating modes will be a function of the critical angle and it can be derived using an eigenvalue equation 2.26:

$$n_{max} = \frac{2h}{\lambda}\sqrt{1 - \frac{c^2}{c_1^2}} + \frac{1}{2} \tag{2.32}$$

- The cut-off frequency for mode propagation can be derived easily from the 2.32 using known relationships $\lambda = \frac{2\pi}{k}$ and $f = \frac{ck}{2\pi}$:

$$f_{n_{cut-off}} = \frac{c}{2h} \frac{\left(n - \frac{1}{2}\right)}{\sqrt{1 - \frac{c^2}{c_1^2}}} \tag{2.33}$$

  Below the frequency defined by a 2.33 a mode will not propagate and it's value is higher than for the hard bottom case.

2.3 Near-Surface Sources

Our next discussion will deal with a special case of an acoustic source location. It will be very useful for our future surface/submerged distinction criteria development to study pressure field properties for a source location near the surface.

We will start with a more intuitive way to explain phenomena described in the literature [13, 10] as a Lloyd Mirror Effect. Lets assume that our source is very close to the surface $z_0 \ll r$. In this case a wave that has been reflected by an air-water boundary could arrive to the receiver approximately at the same time as a direct wave. A reflected wave phase as was already discussed before will be shifted by π, so the destructive interference should be expected at the receiver. The pressure field that will be measured at the receiver for this case will have a different range dependence (non $\sim \frac{1}{r}$) from a free space propagation case.

Now we will redefine our assumption in mathematical form. The subject is well explained in both Frisk and Officer, the last one is using a velocity potential expression for a subject of the discussion . We will use a pressure notation as in Frisk's book in order to keep previous conventions.

We are starting with a old trick which is called a method of images. Let's put an image source above a water-air interface (into the air) at $(0, -z_0)$. In the case of a point source a total field will be a superposition of the source and the image, and we can define it as:

$$p(r,z) = \frac{1}{R_0}\exp(ikR_0) + \frac{1}{R_1}\exp(ikR_1) \tag{2.34}$$

where $R_0, R_1$are distances between a receiver and the source / the image respectively. If we adopt cylindrical coordinates for our case we can define these distances as:

$$R_{0,1} = \sqrt{r^2 + (z^2 \mp z_0^2)} = r\sqrt{1 + \frac{z^2 \mp z_0^2}{r^2}} \tag{2.35}$$

where is a minus sign states for the source case (a shorter distance). By using our initial assumption $z_0 \ll r$ we will simplify the 2.35 by bringing it to a form of $\frac{r}{z}$ expansion. Let's use a binomial expansion for this purpose (also known as a application of Taylor and Maclaurin expansion[14]):

$$(1+x)^m = 1 + mx + \frac{m(m-1)}{2!}x^2 + ... + remainder$$

for m non integer or/and negative. By using the first two terms of the expansion we will get approximation for the ranges as follows:

$$R_{0,1} \approx r\left[1 + \frac{1}{2}\left(\frac{z^2 \mp z_0^2}{r^2}\right)\right] \approx r + \frac{z^2}{2r}$$

Let's rewrite the 2.34 using derived from above relations $\frac{1}{R_1} \approx \frac{1}{R_2} \approx \frac{1}{r}$, $R_1 - R_0 \approx \frac{2zz_0}{r}$, $R_1 + R_0 \approx 2r$

$$p(r,z) \approx \frac{\exp\left(ik\frac{R_0+R_1}{2}\right)}{r}\left[\exp\left(-ik\frac{R_1+R_0}{2}\right) - \exp\left(ik\frac{R_1-R_0}{2}\right)\right] \approx -2i\sin\left(\frac{kzz_0}{r}\frac{\exp(ikr)}{r}\right)$$

By using a linear approximation of a sinus function for small angles we are getting a $\frac{1}{r^2}$ dependence of the pressure field:

$$p(r,z) \approx -2i\frac{kzz_0\exp(ikr)}{r^2} \tag{2.36}$$

As was expected intuitively, the pressure field for a source located very close to a surface (it is important to add at this point that we are assuming a plane interface with no roughness at all, otherwise we should discuss other mechanisms that stayed out of our current discussion) will decay with a much higher rate than $\sim \frac{1}{r}$. The decay rate will be $\sim \frac{1}{r^2}$ as we can see it from the 2.36.

Our discussion will not be complete without a definition of a Lloyd mirror effect area by means of a wavelength. It can be derived by comparing a power radiated by a source located in the Lloyd mirror effect area and in free space. We will show here the final expression from the [13]:

$$\frac{P}{P_0} = 1 - \frac{\sin 2kz_0}{2kz_0} \tag{2.37}$$

We are interested in finding a source depth below which the Lloyd mirror effect could be neglected. To accomplish this goal we need to look for a case of $\frac{P}{P_0} = 1$. The power value for two cases will be the same as long as $\frac{\sin 2kz_0}{2kz_0} = 0$, so $2kz_0 = \pi$ or $z_0 = \frac{\lambda}{4}$. Therefore as long as we are staying below the depth of a quarter wavelength the Lloyd mirror effect can be neglected. We found this criteria very useful for a surface target definition.

Chapter 3

SI for Range-Independent Environments

In the current chapter we will discuss simulation results of a range-independent waveguide. We will show through the numerical results a connection between a source depth and SI (Submergence index) values. An SI algorithm will be presented and an extensive discussion on it's stabilization will be provided.

3.1 Normal modes dependence on the source location

Although we already mentioned in Section 1.1 a connection between surface/submerged location and a high/low modes relation, it has to be shown by numerical results.

To show existence of the connection we investigated some scenarios of different source frequencies. We used 'Kraken'[5] for pressure field calculations. A contribution of each of the normal modes to a total field has been extracted using an orthogonality property. The low and higher modes has been split by a factor of $\frac{1}{3}$ and rounded up to a nearest integer value. For the case of total 10 modes for example, modes $1 \div 4$ will be defined as low modes and modes $5 \div 10$ as high modes. By averaging the amplitude values in each of two modal groups and comparing them we can get a indication on an energy distribution between low and high modes.

For the simulation we used an approximate Monterrey Bay summer sound-speed profile for a 100m depth water-channel. The sound-speed profile was defined by stratifying a channel in 8 levels (see Table 3.1) . A water density was $\rho_w = 1020\frac{kg}{m^3}$. The bottom modeling was based on a fast sediment with a density of $\rho_b = 1800\frac{kg}{m^3}$ and a sound-speed of $c_b = 1612\frac{m}{s}$, the bottom assumed to be a loss media with an attenuation of $\alpha_b = 0.4\frac{dB}{\lambda}$

A graphical description of the environmental model and the applied model are shown on the Fig. 3.1 and the 3.2 respectively.

A receiver array was simulated by 128 vertical equally spaced hydrophones with separation distance of $d = 0.75m$ from each other to satisfy $d \leq \frac{\lambda}{2}$, i.e. $f < 1kHz$. Therefore the chosen spacial sampling rate will be good enough up to a source frequency of $f_0 \approx 1kHz$. The total array length of $L = 127 \times 0.75 = 95.25m$

z[m]	c[m/s]
0	1497
10	1495
15	1492
30	1491
35	1489
45	1488
55	1487
100	1486

Table 3.1: Sound-speed stratification fro simulation

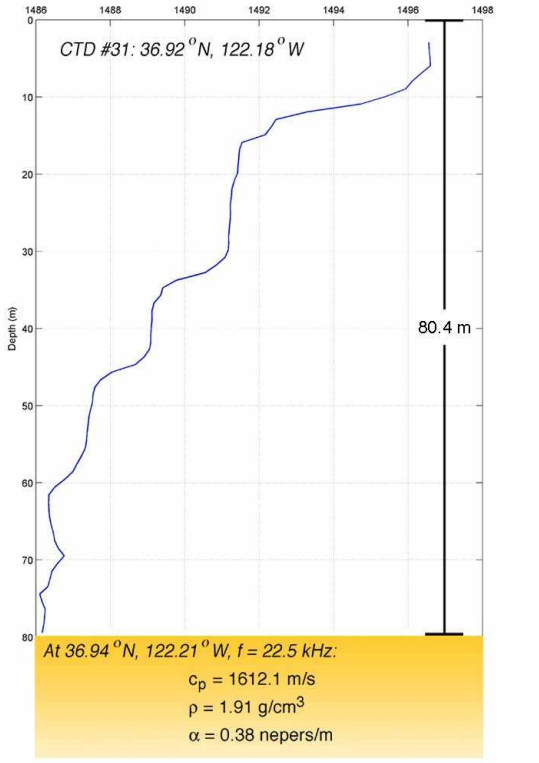

Figure 3.1: Environmental model graph, MB summer

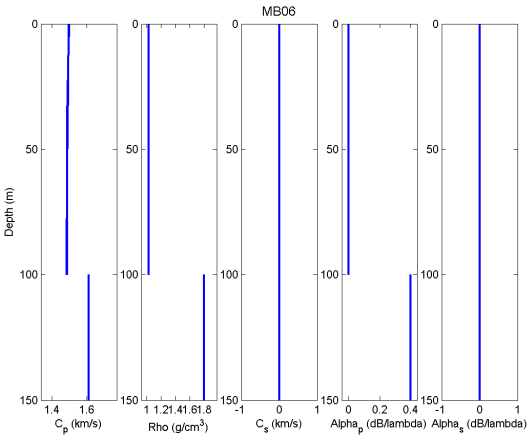

Figure 3.2: Environmental data used for simulation

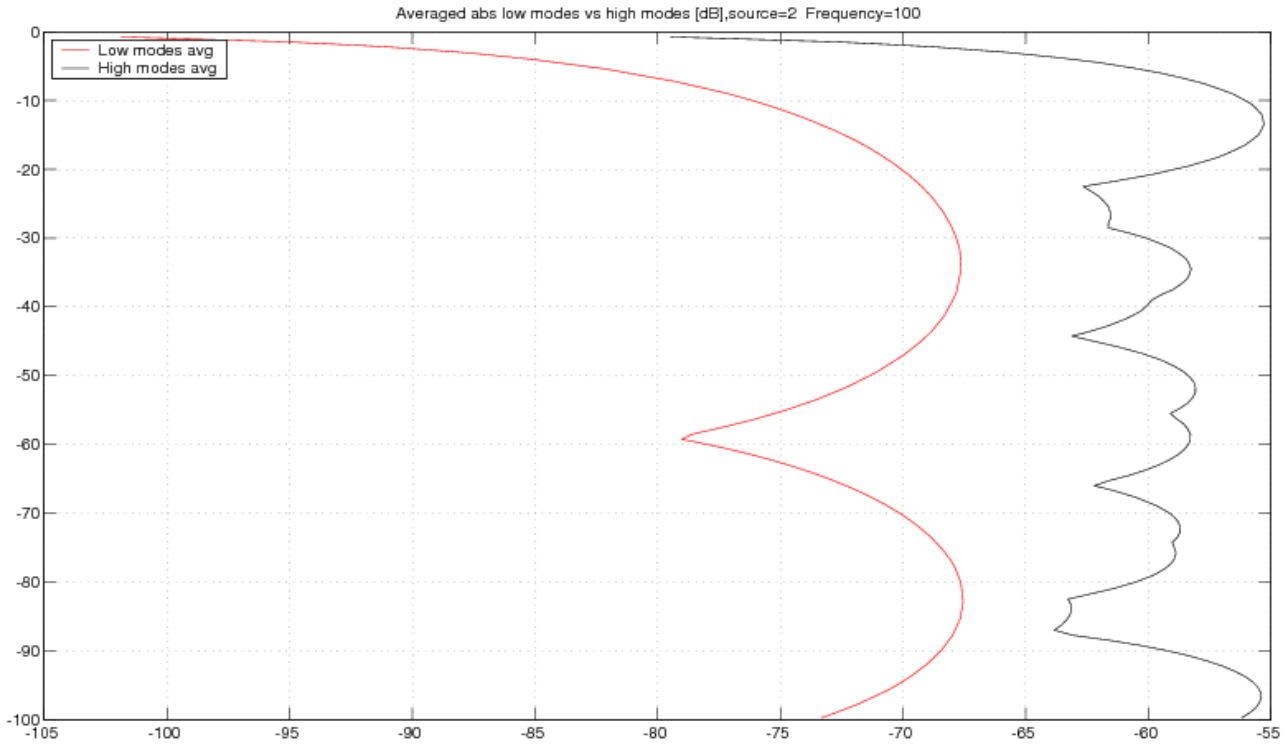

Figure 3.3: Low modes vs high modes power contribution [dB] for surface target of 100Hz

assures an angular resolution of

$$\theta = \arcsin\left(\frac{\lambda}{L}\right) \tag{3.1}$$

for a plane-wave [21]. Therefore for 100Hz source the angular resolution will be $\sim 9^0$and it will be improved up to$\sim 0.9^0$ value for 1kHz source. The source location was chosen to satisfy criteria of a depth just below $\frac{\lambda}{4}$ (Lloyd Mirror criteria, see 2.37) for a surface target simulation case and at least 10m deeper for a submerged case. Because there is a frequency dependence in a surface target criteria expression, we defined two regimes for a surface depth location, the first is $z_0 = 2m$ depth and it will satisfy targets with a frequency up to $f_0 = 500Hz$ and the second is $z_0 = 1m$ for $500Hz < f_0 \leq 1kHz$.

Our goal at this point to analyze a pressure field as close as possible to a source location so it will allow us to exclude propagation effects from our analysis. A range to the receiver for all cases was constant and equal to $r = 10m$. Geometry has been assumed to be completely plane with no roughness for top and bottom interfaces.

We started simulation for a source with a frequency $f_0 = 100Hz$ located at $z_0 = 2m$ depth. It is clearly a surface target case and low modes contribution to a total field is relatively small or in the other words the low modes are less excited. In the current case 5 modes were excited. The results of the simulation are shown in Fig. 3.3.

The separation between an averaged value of the first two modes (low modes-red line) and the three higher modes (high modes-black line) can be noticed through the water-column. Although the results are

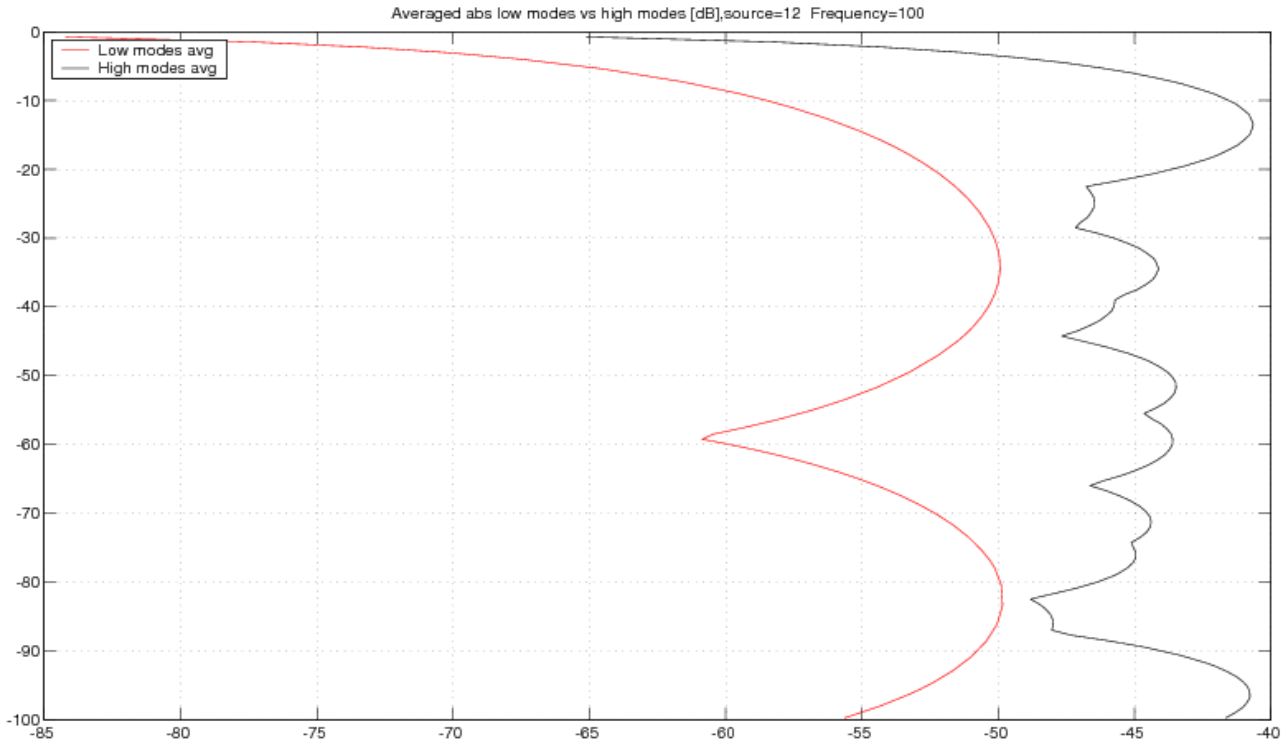

Figure 3.4: Low modes vs high modes power contribution [dB] for submerged at 12m target at f=100Hz

supporting our assumption that for a surface target low modes will be less excited, the results will not be complete without comparing it to a submerged target scenario. So this time we are using a submerged target at depth $z_0 = 12m$ with the same simulation parameters as before. This specific depth was chosen based on the minimum $10m$ separation step between surface and submerged sources. The simulation results shown in Fig.3.4.

By comparing the results shown in Fig.3.3 and Fig.3.4, we can see that the separation between high and low modes is decreasing as a target depth is increasing. To show the tendency we proceed with the simulation and increased the source depth by $10m$ for each next simulation running (see Fig.3.5).

The results show clearly a dependence of low modes excitement on a source depth for 100Hz source. We will proceed with the simulation for source frequencies at 200Hz, 500Hz and 1kHz. From the results in Fig. 3.63.73.8 we can conclude that the relation between a source location (surface/submerged) and a low modes excitement as was found for 100Hz source exists for source frequencies of 200Hz, 500Hz and 1KHz.

It will be reasonable to assume that we will find the same dependence for other source frequencies in the band of 100Hz and 1kHz , so the results of the simulation are not occasional. The assumption based on the numerical results for a 1kHz frequency case with total number of 51 modes which can be very difficult to analyze with pure analytic tools.

After we checked the correctness of our theory on some numerical examples we can proceed to a stage of SI calculations.

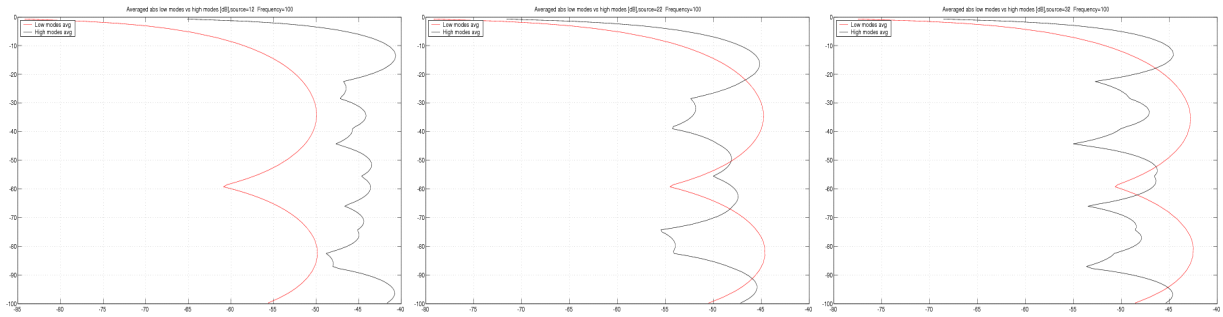

(a) source depth 12m (b) source depth 22m (c) source depth 32m

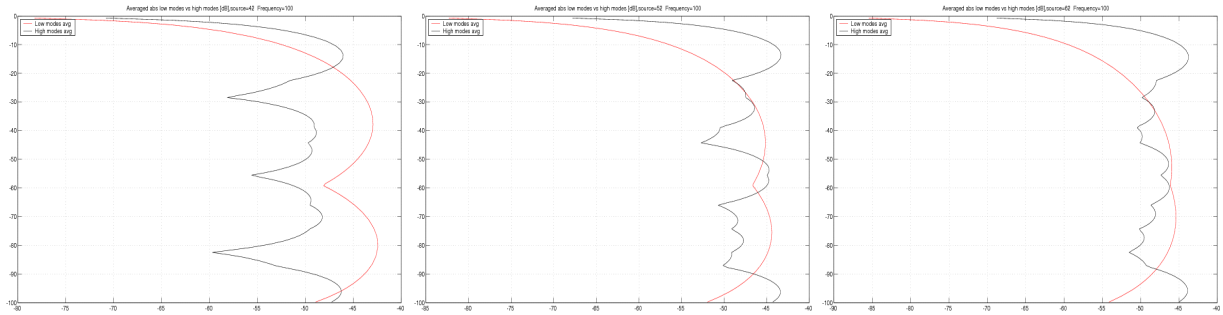

(d) source depth 42m (e) source depth 52 (f) source depth 62m

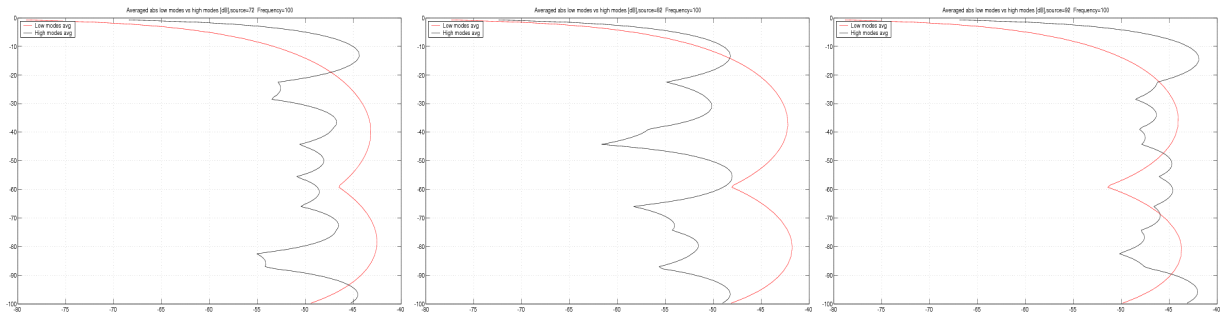

(g) source depth 72m (h) source depth 82m (i) source depth 92m

Figure 3.5: Low modes vs high modes [dB] for submerged targets between 12m and 92m at f=100Hz

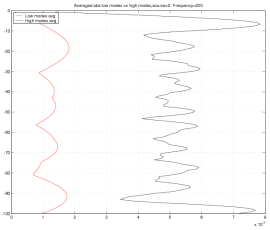

(a) source depth 2m

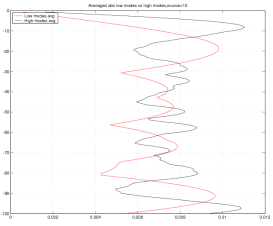

(b) source depth 12 m

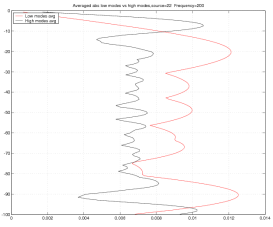

(c) source depth 22m

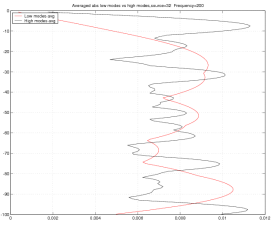

(d) source depth 32m

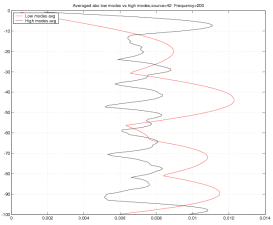

(e) source depth 42m

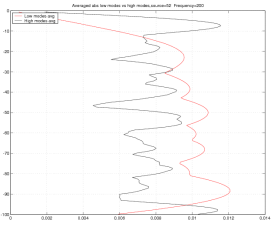

(f) source depth 52m

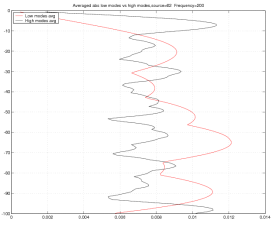

(g) source depth 62m

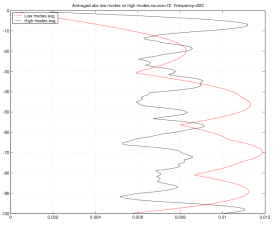

(h) source depth 72m

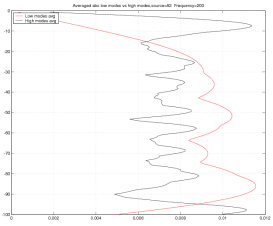

(i) source depth 82m

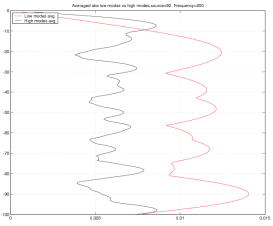

(j) source depth 92m

Figure 3.6: Low modes vs high modes for submerged targets between 2m and 92m at f=200Hz

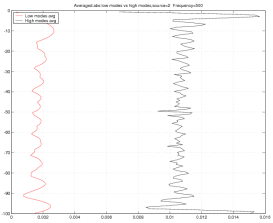

(a) source depth 2m

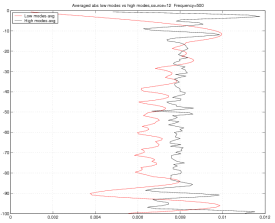

(b) source depth 12m

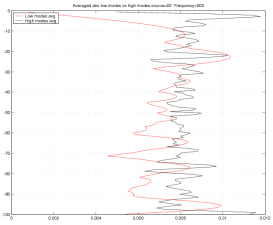

(c) source depth 22m

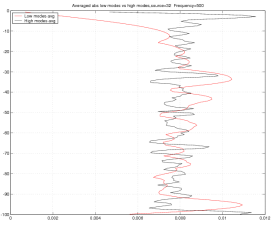

(d) source depth 32m

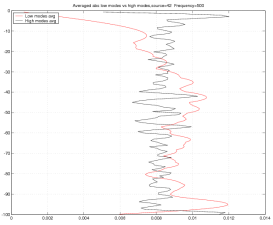

(e) source depth 42m

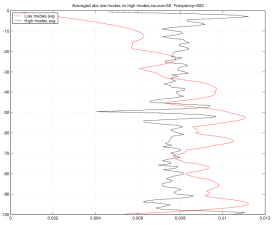

(f) source depth 52

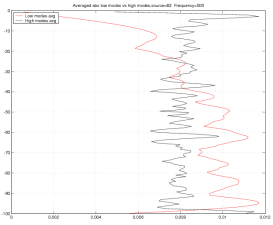

(g) source depth 62m

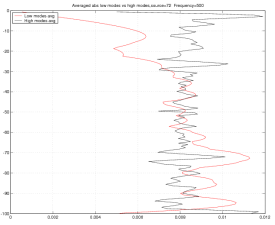

(h) source depth 72m

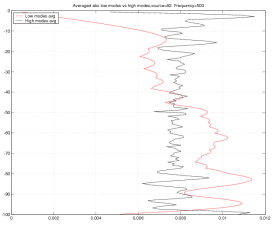

(i) source depth 82m

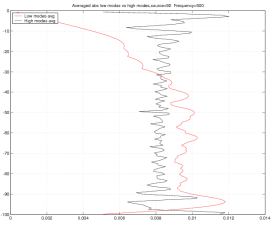

(j) source depth 92m

Figure 3.7: Low modes vs high modes for submerged targets between 12m and 92m at f=500Hz

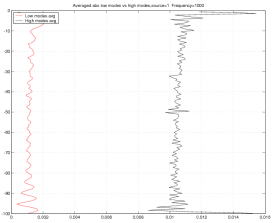

(a) source depth 1m

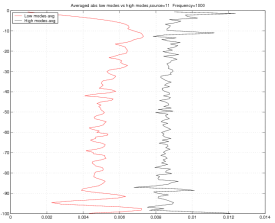

(b) source depth 11m

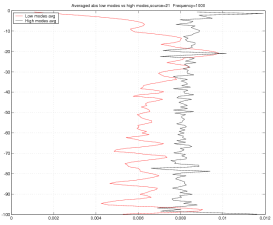

(c) source depth 21m

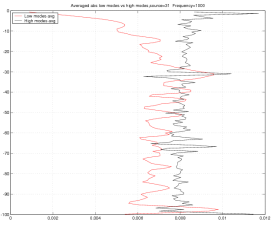

(d) source depth 31m

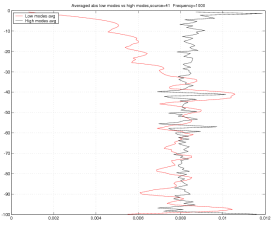

(e) source depth 41m

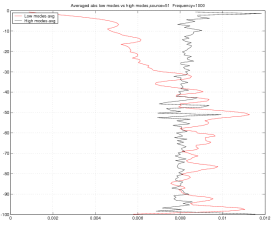

(f) source depth 51m

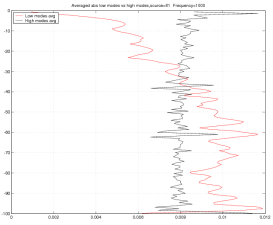

(g) source depth 61m

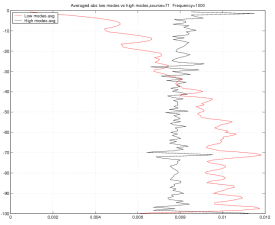

(h) source depth 71m

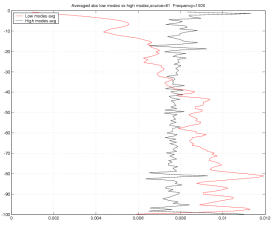

(i) source depth 81m

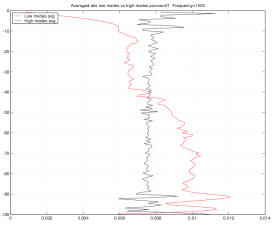

(j) source depth 91m

Figure 3.8: Low modes vs high modes for submerged targets between 12m and 92m at f=1kHz

$z_0[m]$	$c[\frac{m}{s}]$
0	1500
20	1498
30	1485
100	1480

Table 3.2: Water-column sound-speed profile

3.2 SI calculation for range independent environment

At the current section we will describe shortly an algorithm for a Submergence Index (SI) calculation. Examples of SI calculations will be presented and discussed.

3.2.1 SI algorithm description.

For SI properties and it's robustness study we initially used an algorithm that was developed by Prof. Henrik Schmidt. The algorithm is using an OASES[15] simulation package as a propagation model. The main idea behind the algorithm is to run an OASES simulation for specific source-receiver depth values. OASES is producing plane wave replicas in the MCM (Multiple-Constraints beamforming)[16] mode. For each source-receiver position an SI can be calculated by an appropriate shallow-steep angles separation of the received pressure field (calculated by the OASES). For a fixed source position the final averaged SI value is calculated by taking an average of SI's for different receiver depth values. A balance between a calculation time and accurate final SI results should be established as a output of the current study. The algorithm is repeating for incremental values of the source depth, so an SI dependence on the source location can be studied and SI's for surface or submerged targets can be compared. An algorithm flowchart description can be found in Fig. 3.9.

3.2.2 Simulation parameters description and analysis of the simulation results

Although the algorithm is quite straightforward, it can be useful to describe shortly some of main setting parameters. One of the first parameters that has direct impact on the calculation time will be a number of discrete depth levels. As was already mentioned before, by increasing a number of stratifying levels we can improve a calculation's resolution and make an averaging process through receiver depth levels more robust but a trade-off will be a non-linear increase in calculation time. For example, in the case of 5 levels we will need to calculate the pressure field for a total of $5^2 = 25$ source-receiver locations, meaning 25 iterations of OASES calculations. But even by increasing stratification level's number by 1 we have to add to the calculation period a duration of 11 iterations ($6^2 = 36$). As an initial value we chose 10 as a number of discrete depth levels. The environmental parameters were defined as described in Table 3.2.

A frequency of $f = 300Hz$ has been studied at first. For this purpose a horizontal 32 hydrophones array with a spacing of 2.5m was chosen to satisfy the space sampling criteria ($\frac{\lambda}{2} \approx 2.5m$). The Hanning window function[18, 17] was chosen for an angle space splitting with a ratio of $\frac{1}{4}$, meaning that a ratio of the energy located in the first 25% of a total angles space below a critical angle θ_c to the energy concentrated in a remaining part of the angle space will be defined as Submergence Index. The source is located in an array's end-fire direction. For example, if a critical angle is 24^0 the first quarter of the an angle space will include subspace between $0^0$and 6^0. There is no special reason for choosing a Hanning window function and some other window functions were studied also. The splitting ratio (or window width) was chosen based on the results of modal excitation study (see 3.1) , yet the ratio is, in some sense, a random value, so it should be also studied as a one of the parameters for SI algorithm improvement.

Other simulation parameters were set to:

- source-receiver separation - 10km,
- bearing - 0^0(end-fire direction),
- source level -120dB,

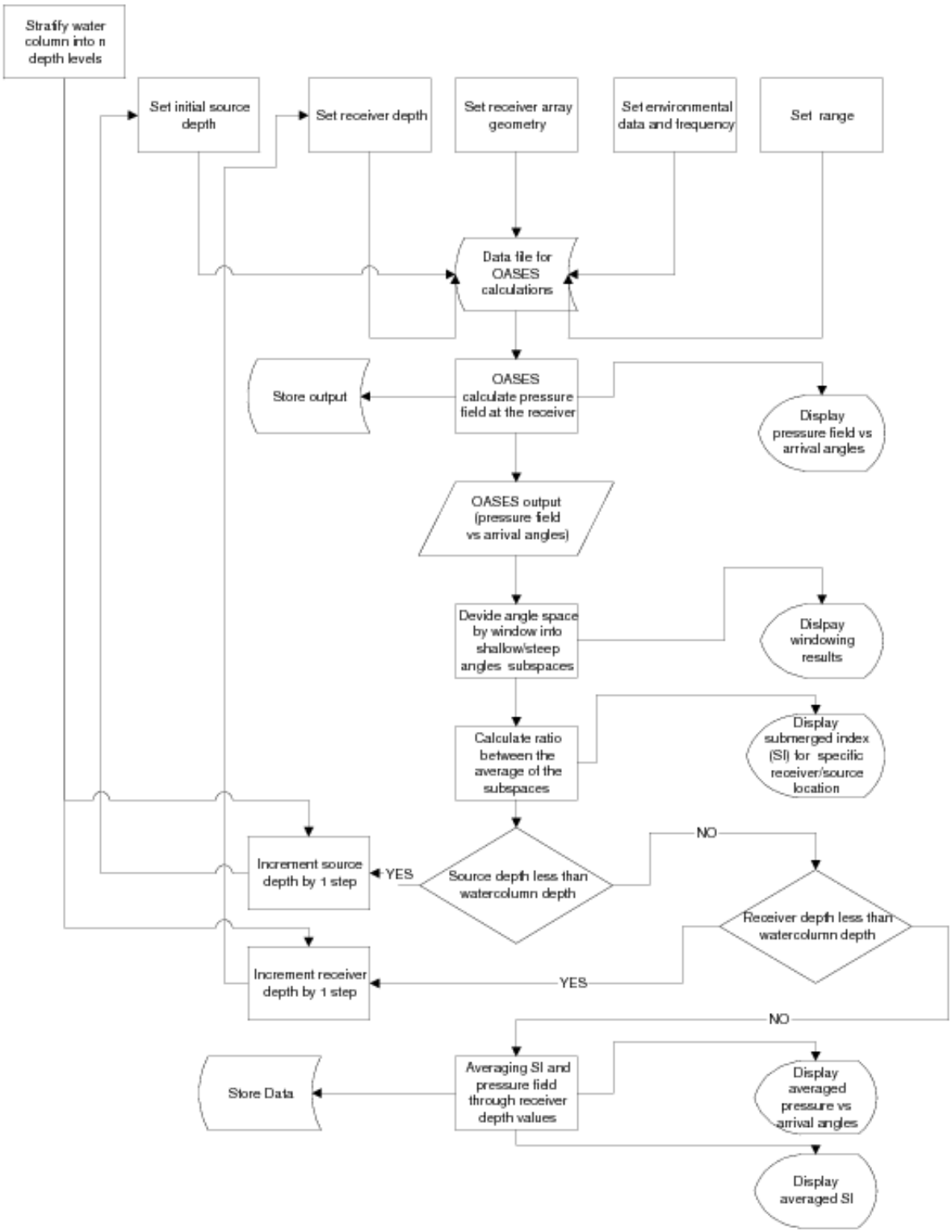

Figure 3.9: SI algorithm flowchart diagram

$z_0[m]$	2	12	22	32	42	52	62	72	82
$c_b = 1575\frac{m}{s}$	-0.3542	1.4423	1.3245	2.1421	2.2227	2.1672	2.2050	2.4699	2.5602
$c_b = 1600\frac{m}{s}$	-0.9550	0.7386	1.1374	2.3634	2.1564	2.0889	2.0575	2.2207	2.5909
$c_b = 1625\frac{m}{s}$	-1.2335	0.7991	1.0315	2.0279	1.8101	2.2316	1.9148	2.0809	2.4645

Table 3.3: Averaged receiver depth SI values in dB

- bottom sound-speed - $c_b = 1575\frac{m}{s}$,
- noise level - 50dB.

The results of a simulation are shown in Fig. 3.10. Fig. 3.10(c) describes graphically an SI calculation output. We can notice a separation of ∼1.75dB in an SI value between the surface ($z_0 = 2m$) and the submerged ($z_0 = 12m$) targets, therefore in the current case SI will be a good indicator to categorize the target. The Fig. 3.10(a) upper part shows a beamformer output for one of simulation transient states for which the source and the receiver are both located at 82m depth, a critical angle is $\sim 18^0$(vertical line). The down part of the figure shows results of Hanning windowing. An averaged ratio of shallow to steep angles (red and green colors respectively in Fig. 3.10(a)) for the particular geometry case shown in Fig. 3.10(b) and it is actually pre-averaged description of SI. Fig. 3.10(d) shows a receiver depth averaged beamformer output and can be a very good indicator of the energy distribution between shallow and steep angles. We can see visually the differences between a surface and a submerged target in the current case, therefore the SI final results shouldn't surprise us.

Although our first study case fitted very well to the theoretical assumptions about SI, it will be not satisfying to make final conclusions at this point, the results could be very random and we should definitely to look at some different cases.

3.2.3 Bottom sound-speed vs SI results.

We will next investigate, the influence of small bottom sound-speed changes on the SI value. From a modal theory point of view we can recall that for a Pekeris waveguide a faster bottom means more trapped modes are expected. Therefore we can expect that a shallow angles relative part will increase, meaning in a modal domain that more modes will be defined as low modes, but steep angles relative part should also increase so it is hard to conclude that a separation between a surface and a submerged target in an SI value will increase. We have to use a numerical solution to make conclusions concerning connection between bottom velocity deviations and an SI value.

We ran the simulation for two different values of bottom sound-speed: $c_b = 1600/1625\frac{m}{s}$,leaving other parameters without changes. The results are shown in Fig. 3.11 and Fig. 3.12 respectively.

From the graphical representation of SI values unclear if there is any separation improvement between surface and submerged sources, especially among $c_b = 1575\frac{m}{s}$ and $c_b = 1600\frac{m}{s}$ cases. So we have to compare the averaged numerical SI results, shown in Table 3.3. Based on the numerical results, the only dependence that immediately can be noticed is that SI for a surface target is getting smaller as a bottom speed value is growing. Other SI values are fluctuating and there is no obvious dependence can be pointed on. Although there is no surface/submerged separation improvement between $c_b = 1575\frac{m}{s}$ and $c_b = 1600\frac{m}{s}$, we are assuming that the tendency of slow SI decreasing will continue and a separation improvement will continue as a gradient between velocity at the bottom of a water-column and a sound-speed velocity into the bottom layer will grow. A more general conclusion arises from the presented results - small oscillations in the bottom velocity will degrade separation capability of SI.

3.2.4 Changes in bearing vs SI results

We have been interested as a part of our study to learn a bearing angle influence on SI capabilities to distinguish between targets. We used the SI algorithm for different bearing angles between $5^0 - 55^0$, a bottom sound-speed was set to $c_b = 1612\frac{m}{s}$ to create more realistic profile. We didn't make any changes

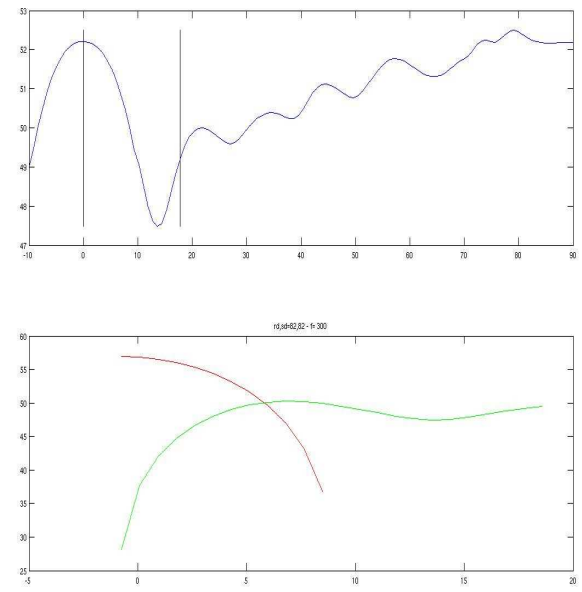

(a) Beamformer output for source/receiver at 82m depth

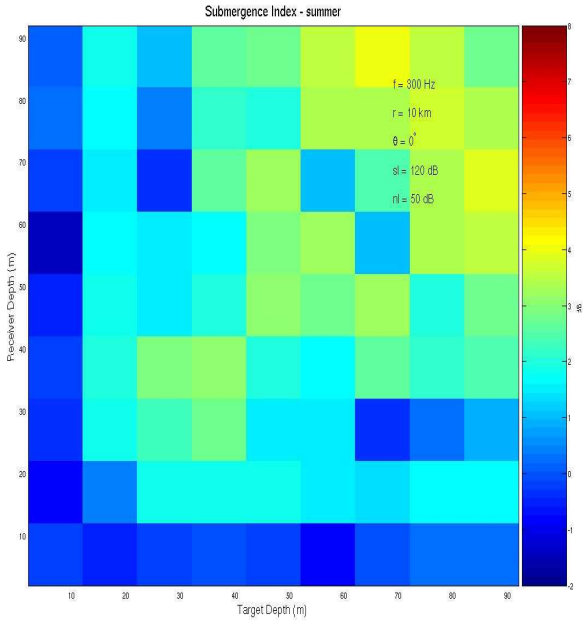

(b) SI for all depth/ receiver depth combinations

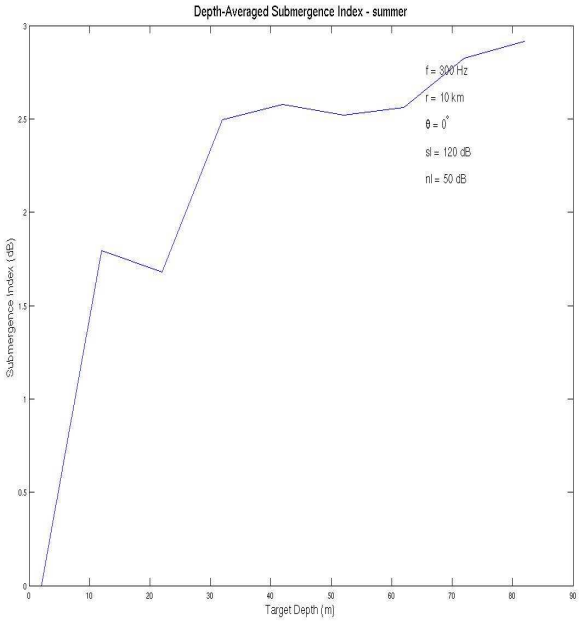

(c) Averaged receiver depth SI

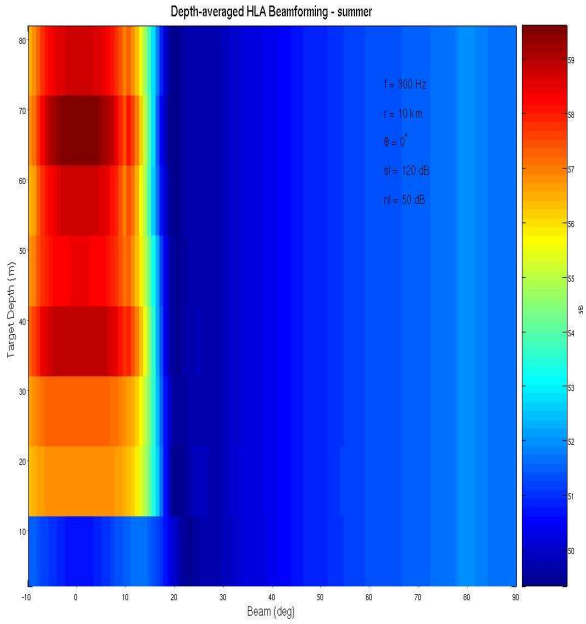

(d) Averaged receiver depth beamformer output

Figure 3.10: SI algorithm output for 300Hz source,$c_b = 1575\frac{m}{s}$, bearing 0^0.

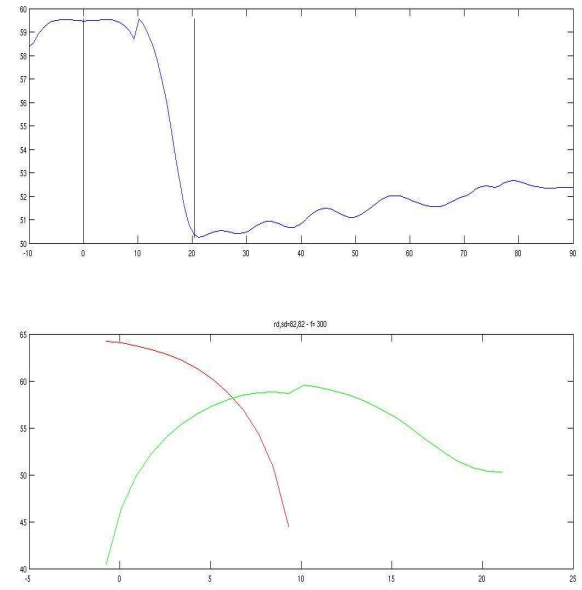

(a) Beamformer output for source/receiver at 82m depth

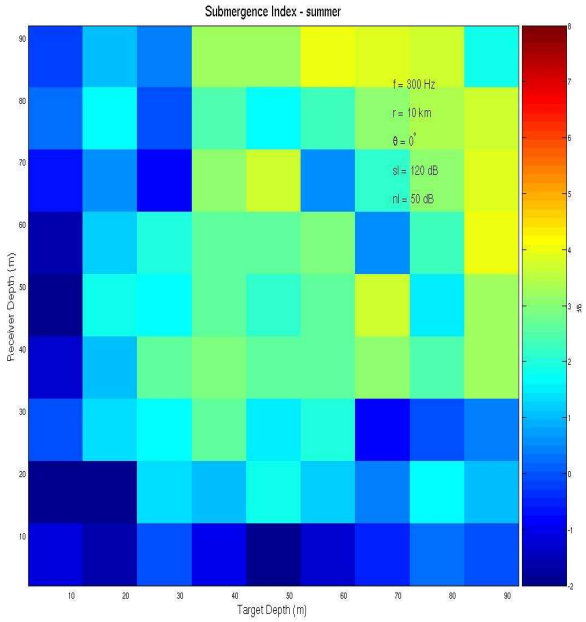

(b) SI for all depth/ receiver depth combinations

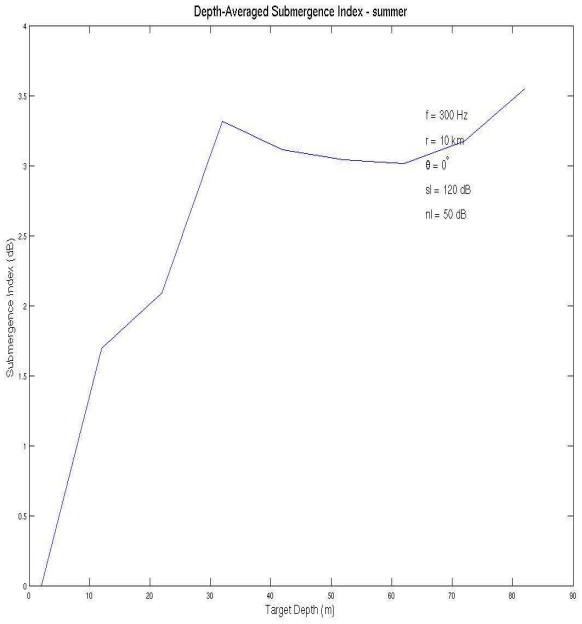

(c) Averaged receiver depth SI

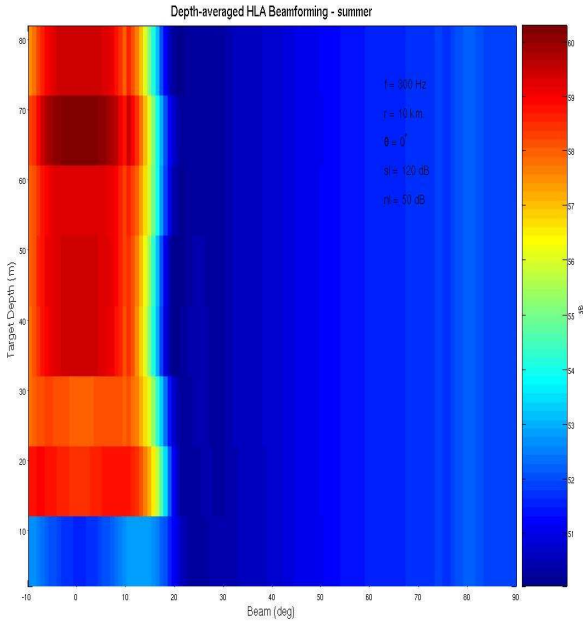

(d) Averaged receiver depth beamformer output

Figure 3.11: SI algorithm output for 300Hz source,$c_b = 1600\frac{m}{s}$, bearing 0^0

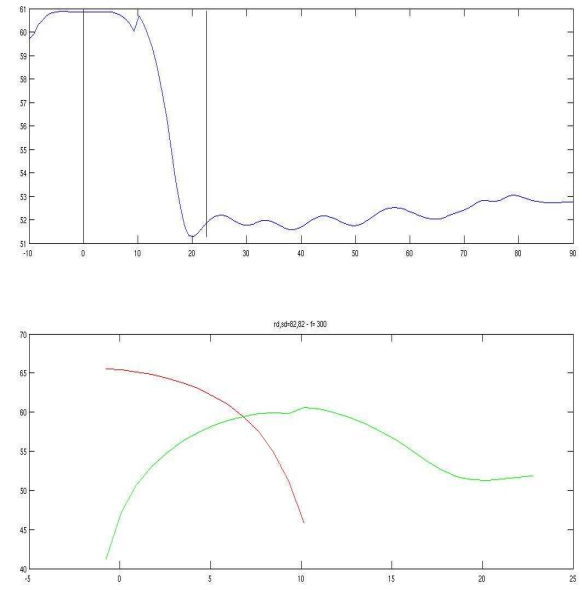

(a) Beamformer output for source/receiver at 82m depth

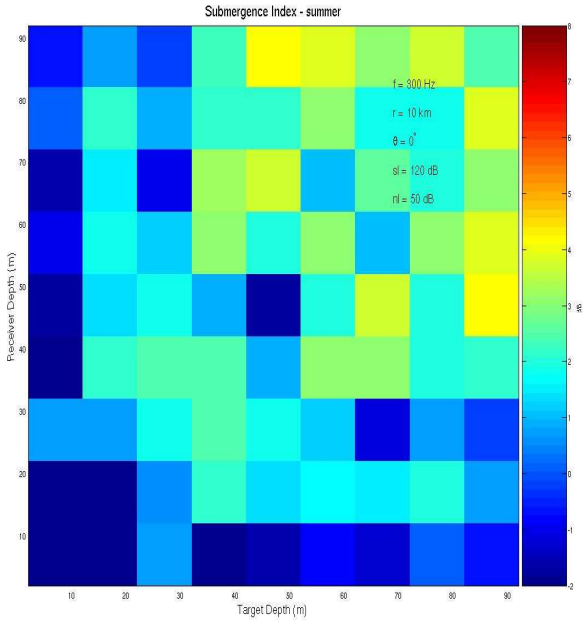

(b) SI for all depth/ receiver depth combinations

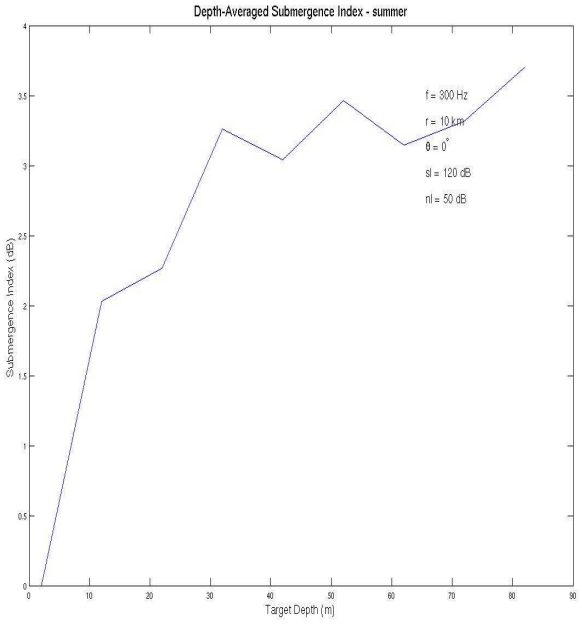

(c) Averaged receiver depth SI

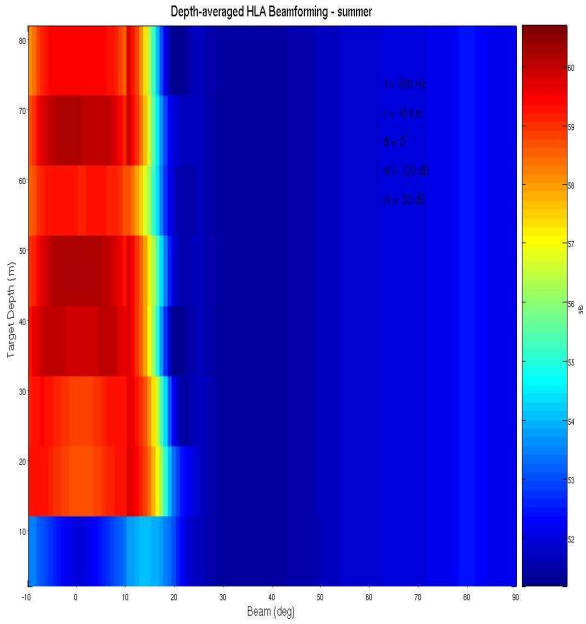

(d) Averaged receiver depth beamformer output

Figure 3.12: SI algorithm output for 300Hz source,$c_b = 1625\frac{m}{s}$, bearing 0^0

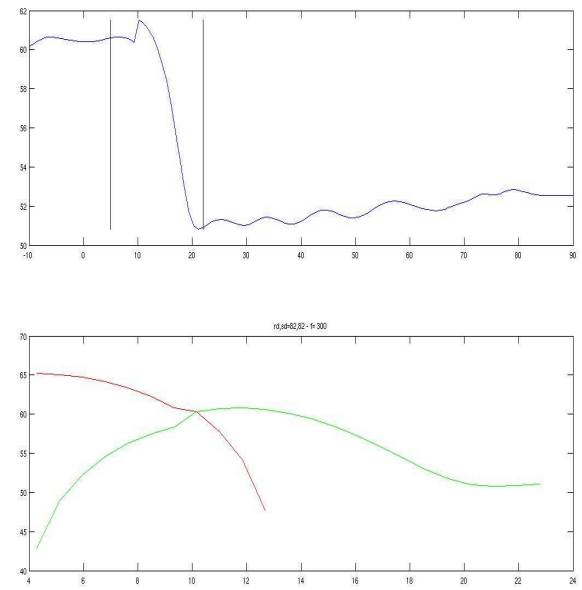

(a) Beamformer output for source/receiver at 82m depth

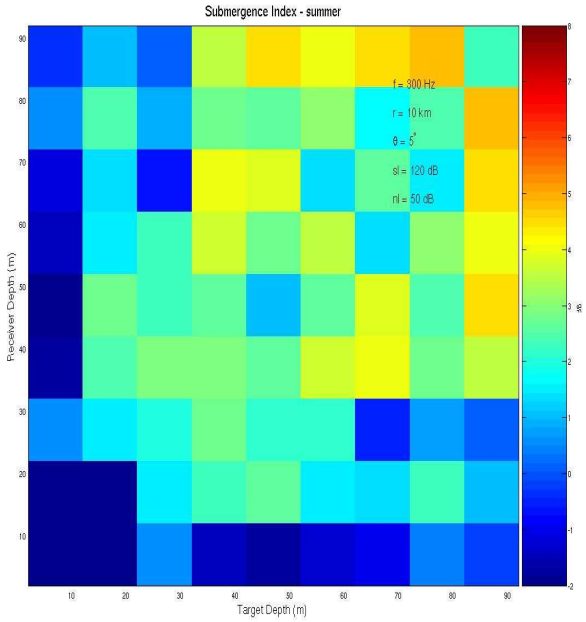

(b) SI for all depth/ receiver depth combinations

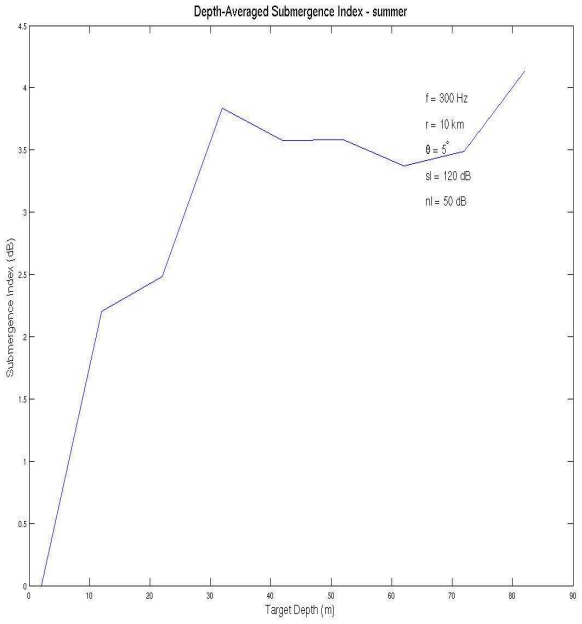

(c) Averaged receiver depth SI

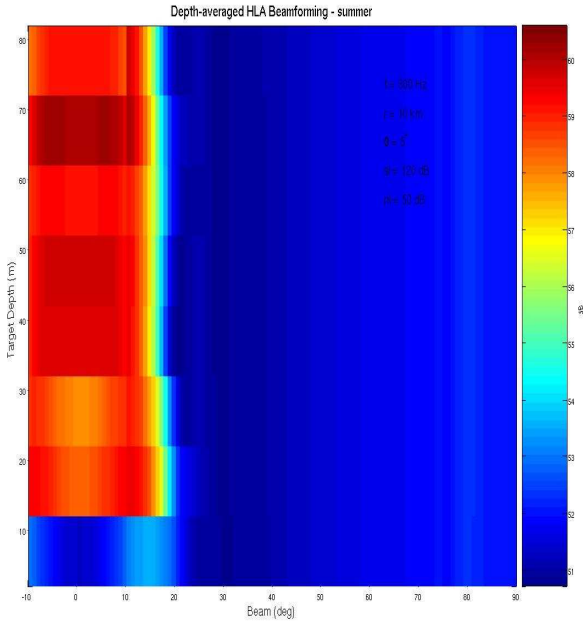

(d) Averaged receiver depth beamformer output

Figure 3.13: SI algorithm output for 300Hz source,$c_b = 1612\frac{m}{s}$, bearing 5^0

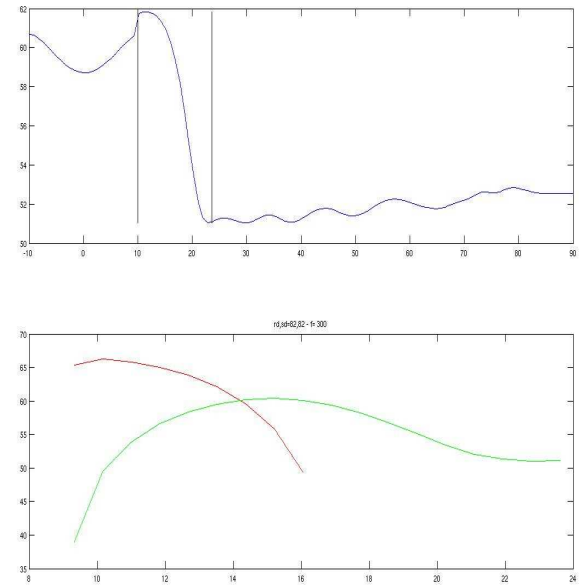

(a) Beamformer output for source/receiver at 82m depth

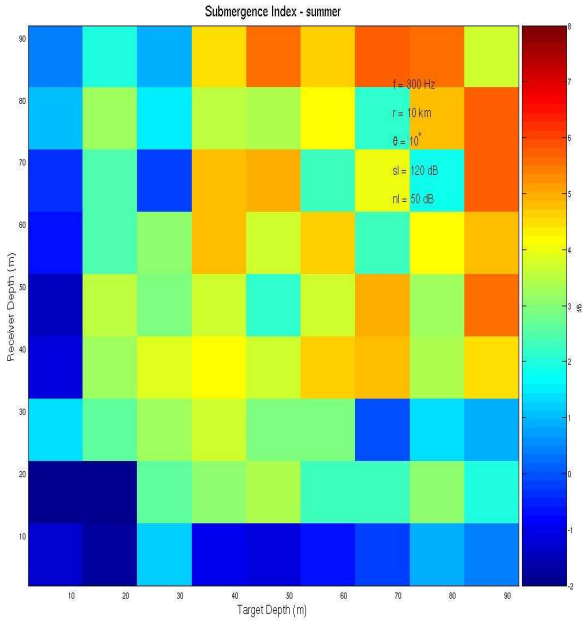

(b) SI for all depth/ receiver depth combinations

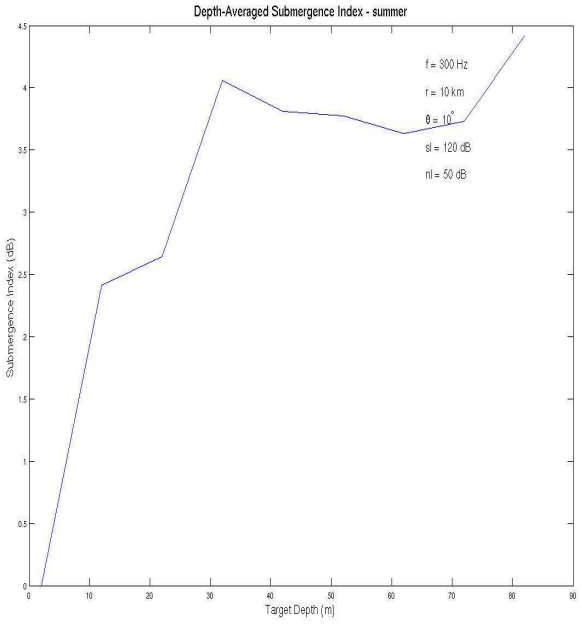

(c) Averaged receiver depth SI

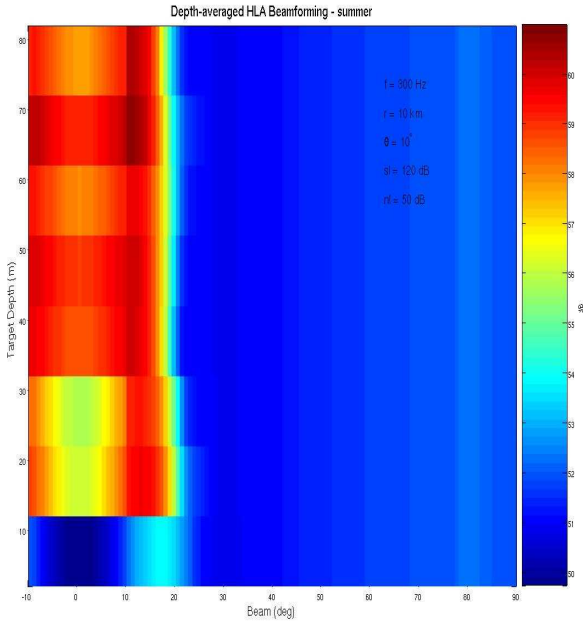

(d) Averaged receiver depth beamformer output

Figure 3.14: SI algorithm output for 300Hz source,$c_b = 1612\frac{m}{s}$, bearing 10^0

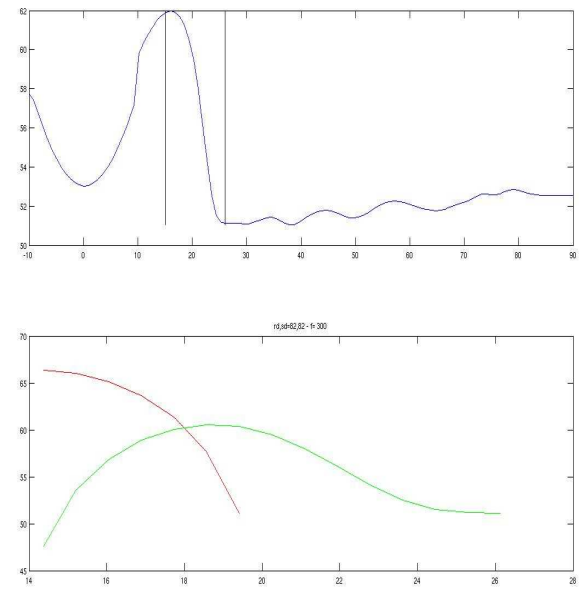

(a) Beamformer output for source/receiver at 82m depth

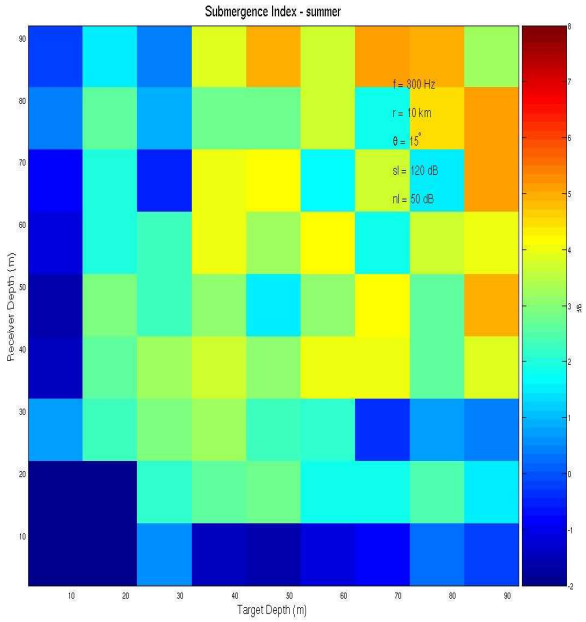

(b) SI for all depth/ receiver depth combinations

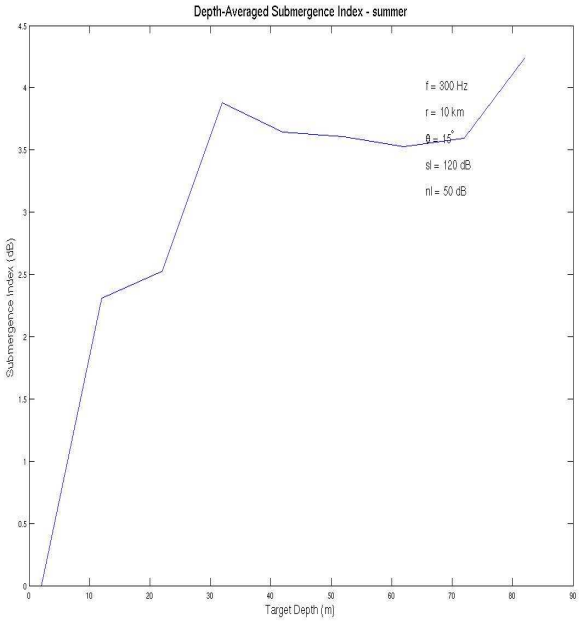

(c) Averaged receiver depth SI

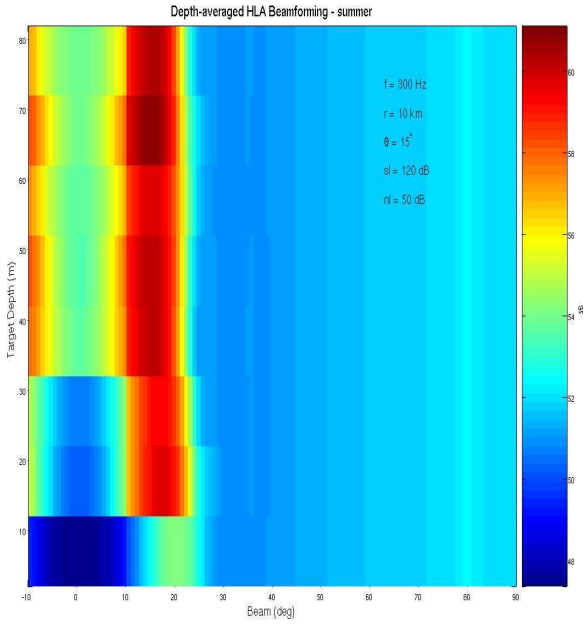

(d) Averaged receiver depth beamformer output

Figure 3.15: SI algorithm output for 300Hz source,$c_b = 1612\frac{m}{s}$, bearing 15^0

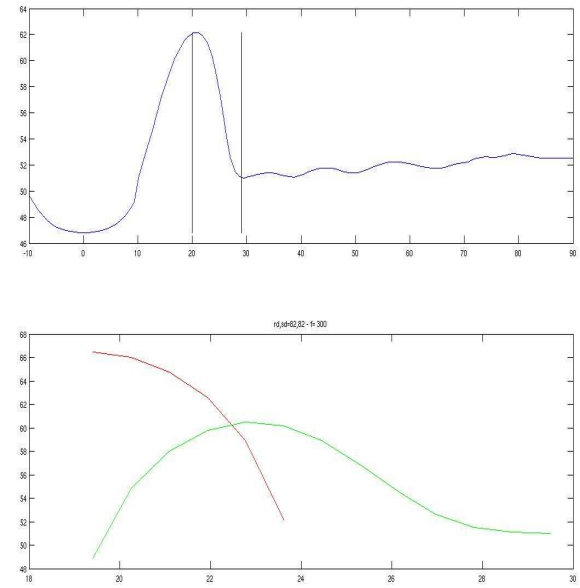

(a) Beamformer output for source/receiver at 82m depth

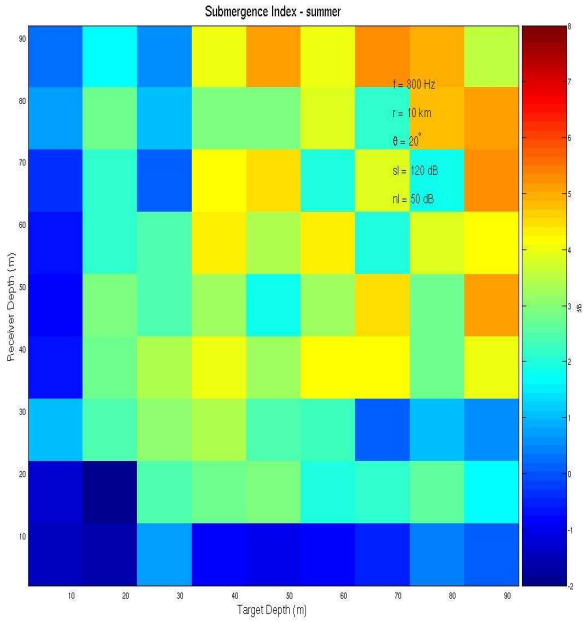

(b) SI for all depth/ receiver depth combinations

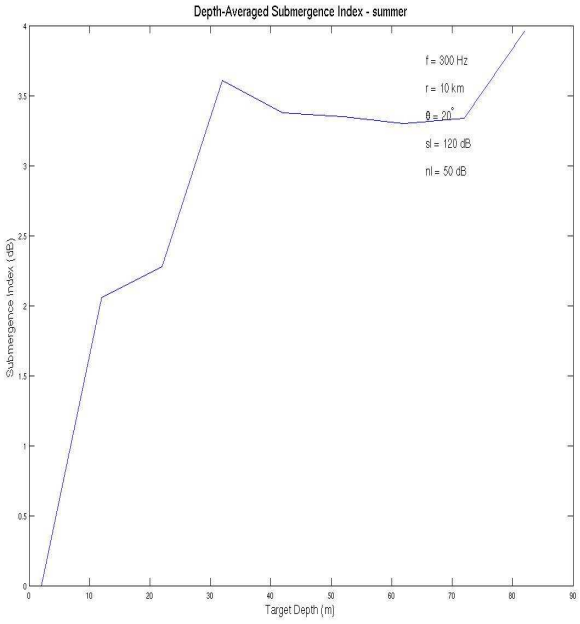

(c) Averaged receiver depth SI

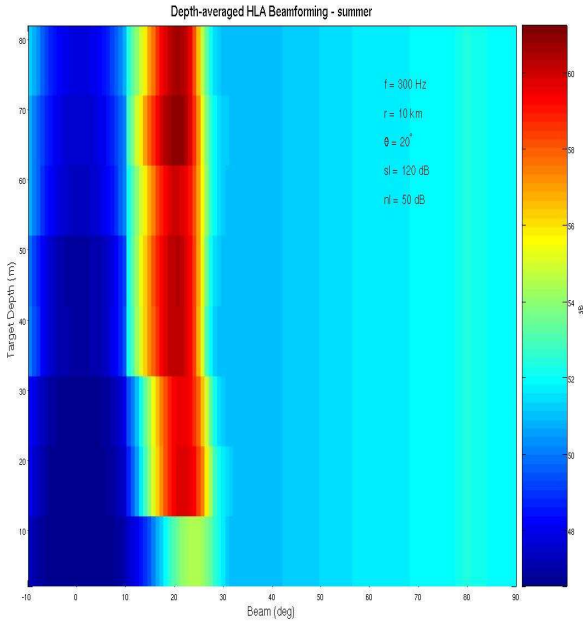

(d) Averaged receiver depth beamformer output

Figure 3.16: SI algorithm output for 300Hz source,$c_b = 1612\frac{m}{s}$, bearing 20^0

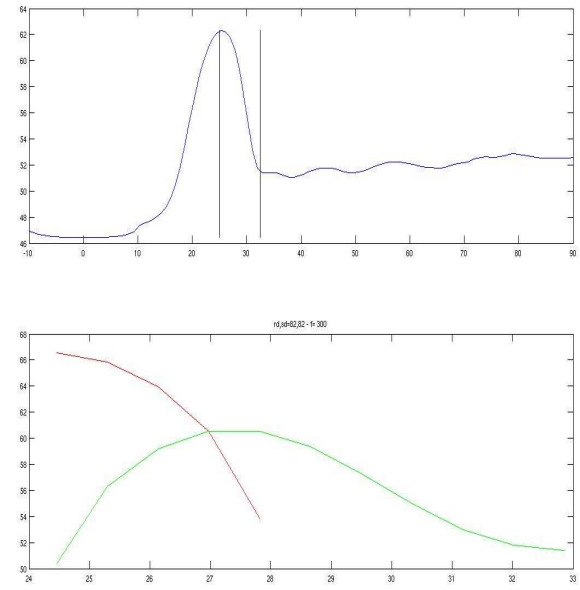

(a) Beamformer output for source/receiver at 82m depth

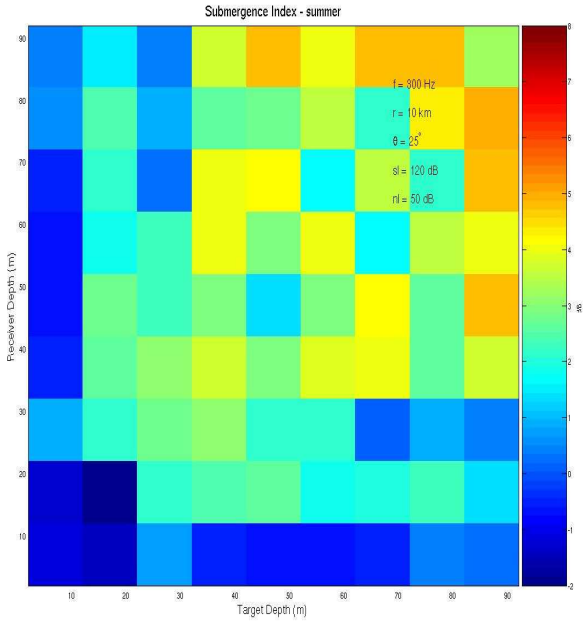

(b) SI for all depth/ receiver depth combinations

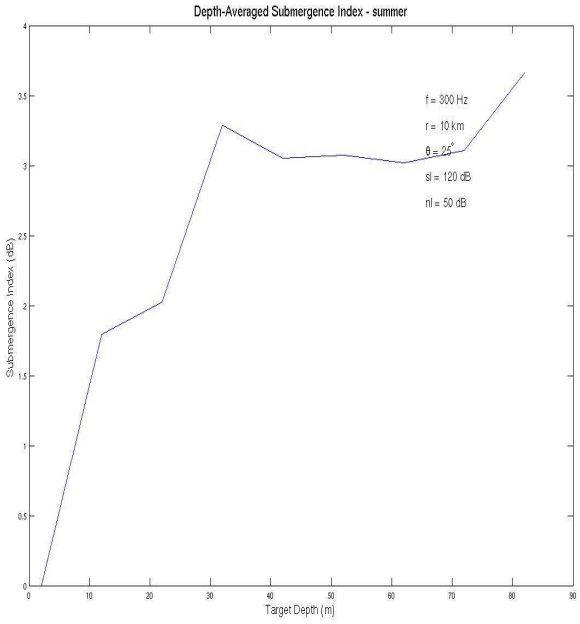

(c) Averaged receiver depth SI

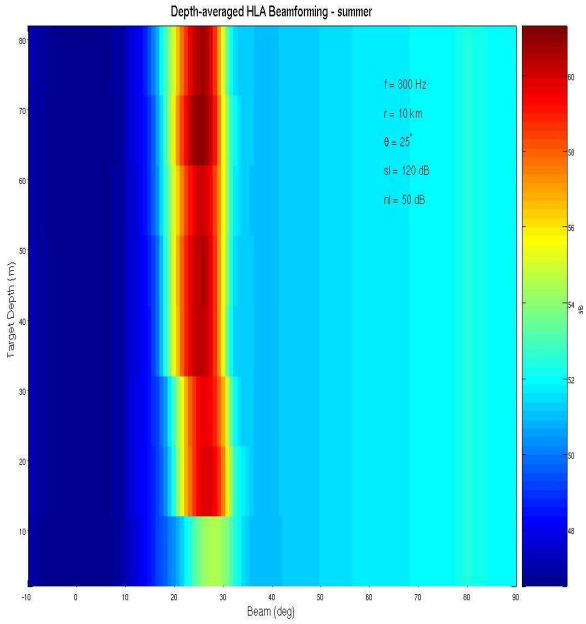

(d) Averaged receiver depth beamformer output

Figure 3.17: SI algorithm output for 300Hz source,$c_b = 1612\frac{m}{s}$, bearing 25^0

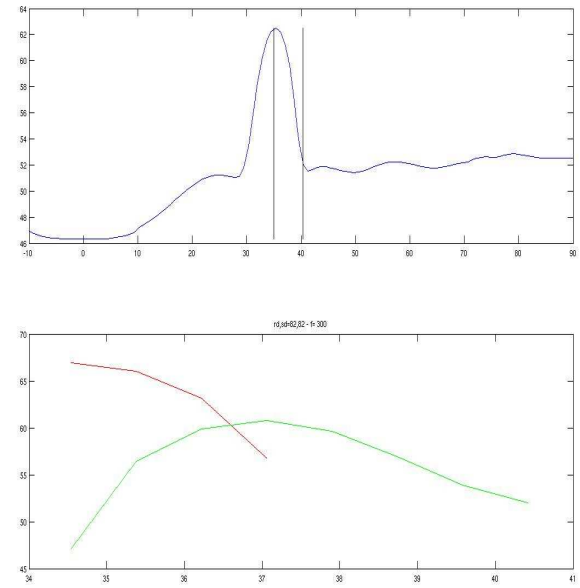

(a) Beamformer output for source/receiver at 82m depth

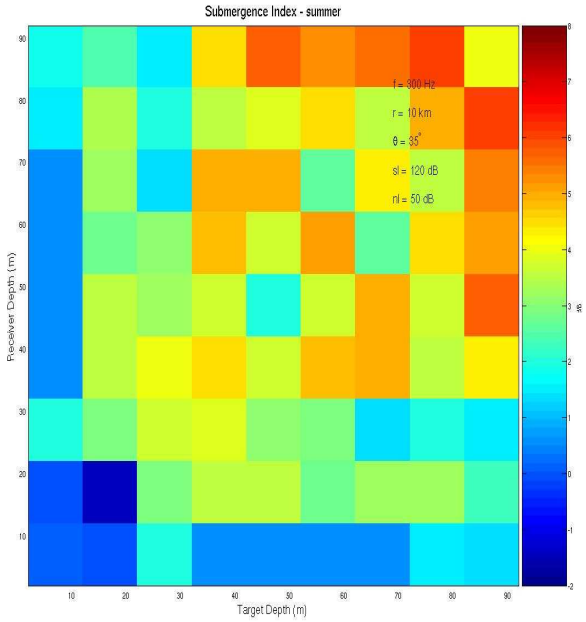

(b) SI for all depth/ receiver depth combinations

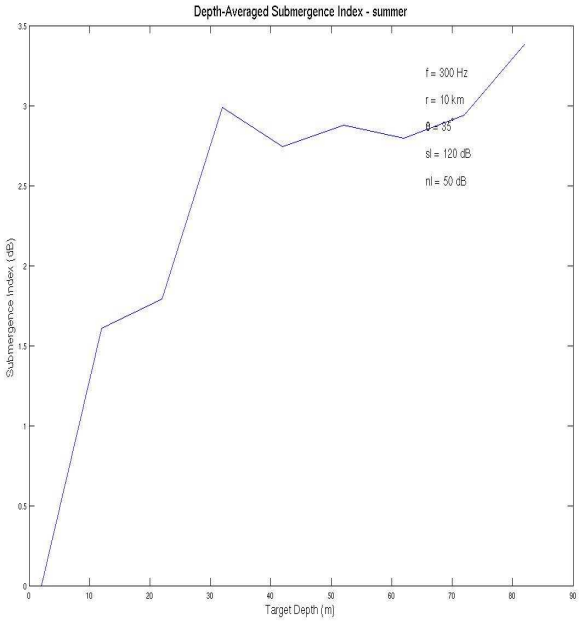

(c) Averaged receiver depth SI

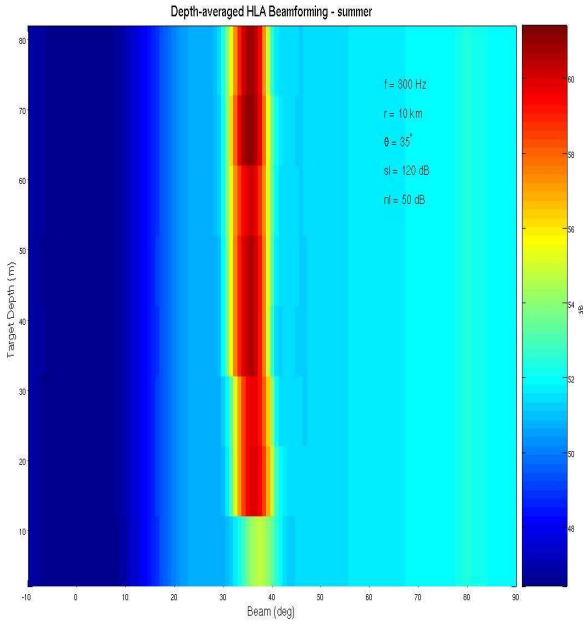

(d) Averaged receiver depth beamformer output

Figure 3.18: SI algorithm output for 300Hz source,$c_b = 1612\frac{m}{s}$, bearing 35^0

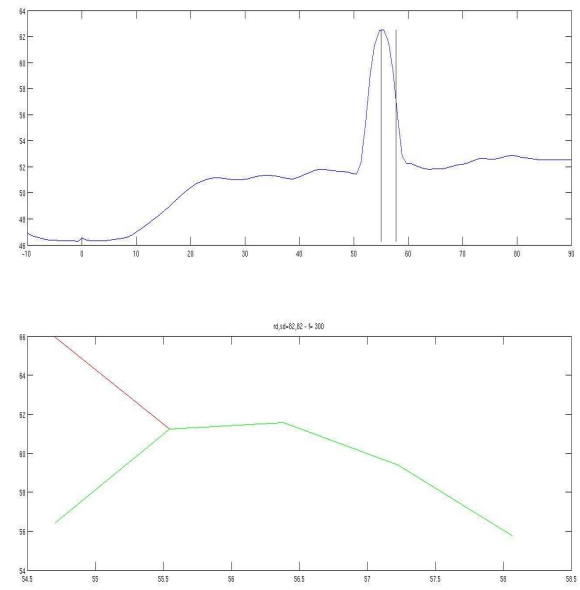

(a) Beamformer output for source/receiver at 82m depth

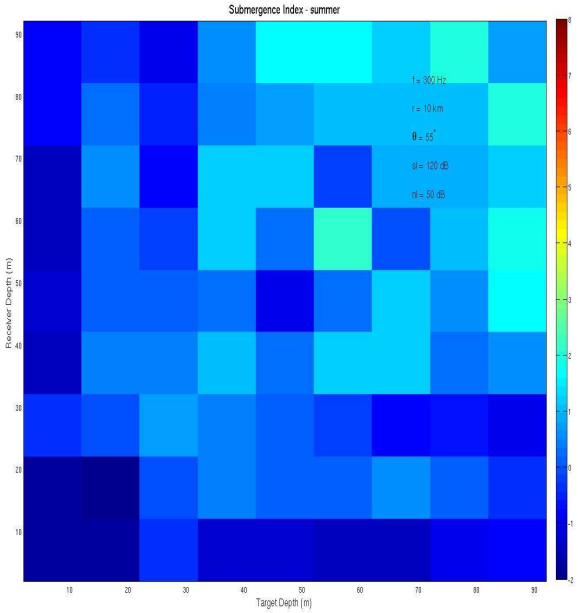

(b) SI for all depth/ receiver depth combinations

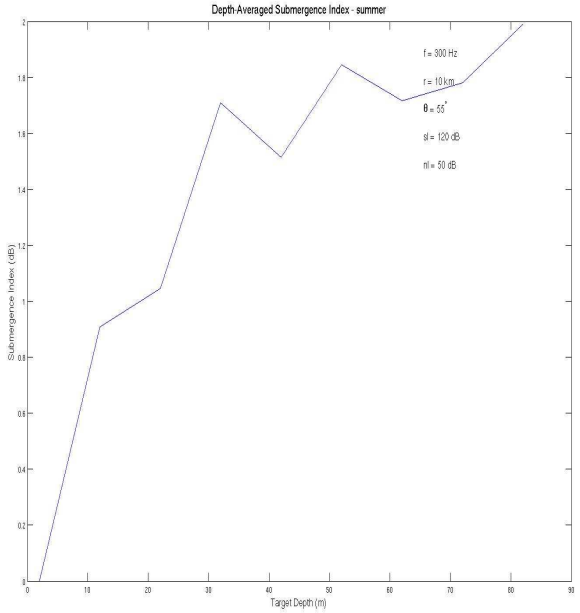

(c) Averaged receiver depth SI

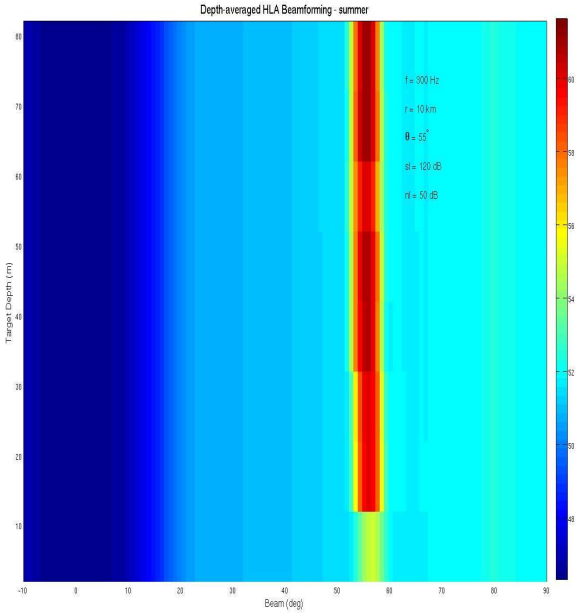

(d) Averaged receiver depth beamformer output

Figure 3.19: SI algorithm output for 300Hz source,$c_b = 1612\frac{m}{s}$, bearing 55^0

Depth[m]	2	12	22	32	42	52	62	72	82
5 degrees	0	2.206535	2.480343	3.837674	3.575308	3.579411	3.370111	3.489219	4.133561
10 degrees	0	2.414774	2.641773	4.060378	3.810047	3.773722	3.630781	3.730757	4.41962
15 degrees	0	2.307565	2.523109	3.877021	3.644636	3.605533	3.525793	3.594004	4.238014
20 degrees	0	2.059453	2.277098	3.604964	3.378639	3.349663	3.301152	3.340176	3.956847
25 degrees	0	1.79283	2.023966	3.286769	3.054922	3.075611	3.020373	3.109049	3.661791
35 degrees	0	1.607837	1.789684	2.987098	2.744084	2.879322	2.796697	2.938716	3.384298
45 degrees	0	1.456295	1.595701	2.574233	2.342001	2.570682	2.445064	2.563295	2.900078

Table 3.4: SI values [dB] for bearing angles $5^0 - 55^0$

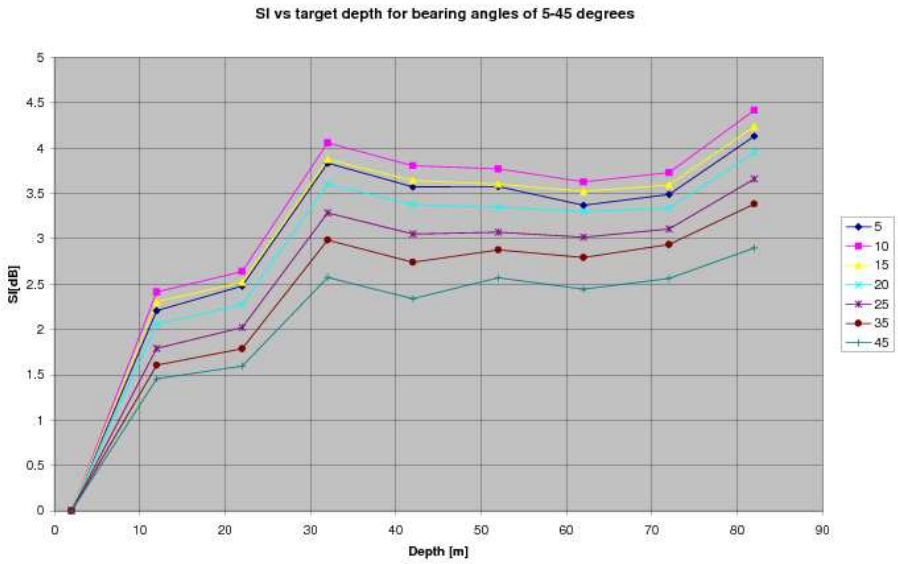

Figure 3.20: Averaged SI values for bearing angles $5^0 - 55^0$

in other parameters at this stage under an assumption that for a current study it will be unnecessary. The results are shown in Fig. 3.13-3.19 corresponding to bearing angles of $5^0 - 55^0$respectively.

We can conclude from the simulation results that as a bearing angle is growing above $\sim 22^0$ the SI capabilities to distinguish between 2m and 12m targets are degrading. But for a relatively small bearing angles the SI dependence can't be seen immediately. We need to make additional analysis beside the graphical results as it was done in 3.2.3. The SI values for the current case can be found in Table 3.4.

We chose to display the values graphically at the same configuration as the simulation output where SI for 2 m target defined as a reference zero value.The results are given in Fig. 3.20using a same axis system for all the cases. From the shown results we can't conclude that there is any dependence between the SI and bearing angles of $5^0 - 20^0$, yet we can state that for relatively small bearing angles the separation value is stable and it is around 2dB. Therefore SI can be useful for surface and submerged targets classification not only in zero bearing (end-fire) case but also for small bearing angles values (less than critical angle value).

3.2.5 SI dependence on a source-receiver range separation

Despite the fact that we are dealing with a range independent waveguide case, SI is expected to change through the range. The most obvious reason for this is decaying of the pressure field with a range increasing and for a long distance case a source level will be eventually same or even below a noise level, and for these ranges SI will not be useful anymore. Beside a range-decaying process regions of constructive and destructive inter-modal interference can be found at different ranges from the source. Therefore we should expect fluctuations in SI values for different ranges. We used the same parameters for the simulation as before for ranges of 1,5,10 and 15km. The results are shown in Fig. 3.21-3.24.

Although SI values are changing with a range, we got satisfying results for ranges of 5 and 10 km. For the two cases a Δ of $\sim$1.5-2 dB in SI values helps to distinguish between targets. For 1 km range the separation is relatively small and ΔSI between 2 m and 12m targets is less than 1dB. We can study from the current results that areas of 'shadow' by means of an SI capability to distinguish between the targets should be expected. We will get back to the SI range dependence issue and study it more carefully with realistic sound-speed profile. Not less important to study 15km results. Generally it can be noticed from Fig.3.24(d) that for a 'far away' from a source case a signal level will be below a noise level. In addition to the range decaying effect we can see that the SI separation capabilities had been degraded. It can be explained by a more significant attenuation in higher modes up to the point in the range where is only one dominant mode (first mode) exists.

Our conclusions concerning a range influence on SI are preliminary at this stage and will be explored extensively in Section 3.2.7

3.2.6 Windowing functions for SI calculations, numerical results.

We already mentioned before (3.2.2) that we chose to use a Hanning window function to split an angle space (or a modal space). Now we will describe and compare results of SI calculations to other standard window functions. We used for this purpose three additional window functions: Blackman-Harris[19], Nutall's Blackman-Harris[20], and triangular[17, 18] function. We are interested to know if there is any improvement in SI ability to separate lower from higher modes in case of using a slightly different window function. The final performances of SI are most interesting in the current case, therefore averaged SI values only will be presented and compared.

By comparing the shown in Fig. 3.25,3.26,3.27 for ranges of 1, 5 and 10km it is hard to make a definite conclusion concerning advantages of a specific windowing technique. We can see a high correlation between all the techniques in ranges of 1 and 5 km, especially in a separation between 2m and 12m targets which is our main concern. At the range of 10km more differences can be noticed, yet the differences are not significant enough to make conclusions and to prefer specific window function among the others. We will continue to use a Hanning window from communality reasons only.

3.2.7 SI and source-receiver range. Extensive view.

At this part we will investigate the reasons for the early discovered (Fig. 3.21) SI mismatch for a 1km range case. We found that at some ranges SI results can mislead us about a target location. We will use a pressure field modal analysis to investigate the reasons for this. Finally, a solution which will improve SI algorithm robustness will be suggested and tested.

To make our study more realistic we changed a water-column sound-speed profile according to Table 3.1. Our intentions were to study 500Hz and 1kHz frequency cases, so we defined an array of 133 horizontal equally spaced hydrophones separated by a $d = 0.75m$. For 1kHz frequency case a surface target was defined as a source at 1m depth based on a Llyod-Mirror effect (see 2.37). Random range values for a simulation were chosen to fulfill requirement for SI algorithm stability and to find if there is some areas of 'shadow' where SI results will bring us to a wrong conclusion concerning a target category. We will present firstly results for 1kHz frequency source.

From the results presented in Fig. 3.28,3.29,3.30,3.31,3.32,3.33,3.34 it can be immediately noticed that an SI supplies robust indication of the source category for a relatively wide spectrum of range values. As promising the results may be looks there is still an unsolved issue of a 'shadow' area that must be studied.

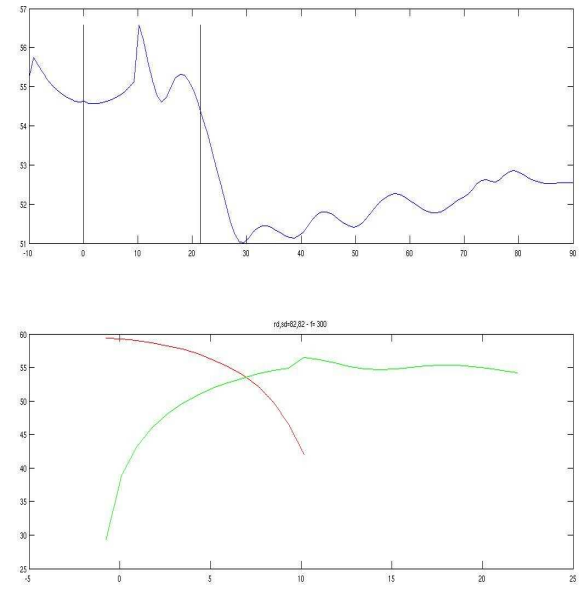

(a) Beamformer output for source/receiver at 82m depth

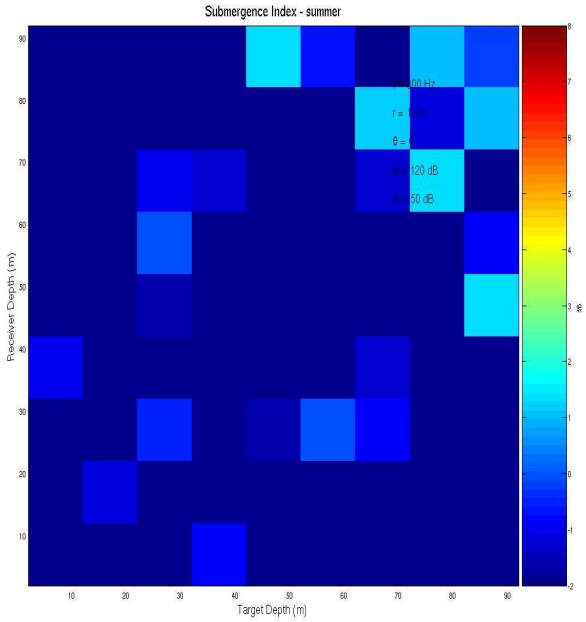

(b) SI for all depth/ receiver depth combinations

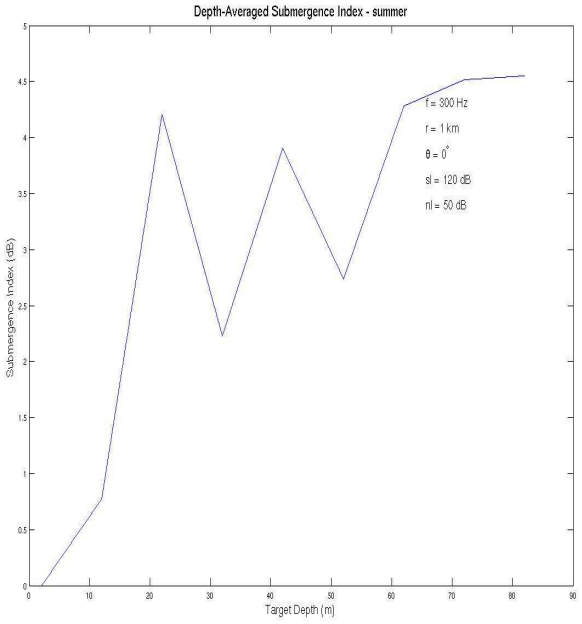

(c) Averaged receiver depth SI

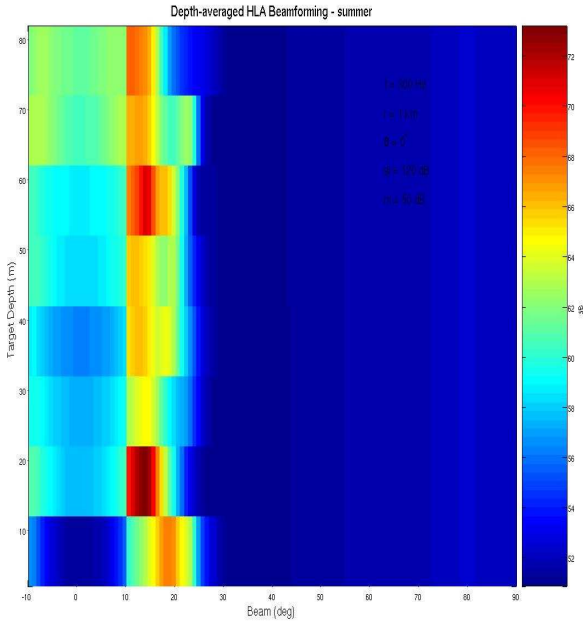

(d) Averaged receiver depth beamformer output

Figure 3.21: SI algorithm output for 300Hz source,$c_b = 1612\frac{m}{s}$, bearing 0^0, range $1km$

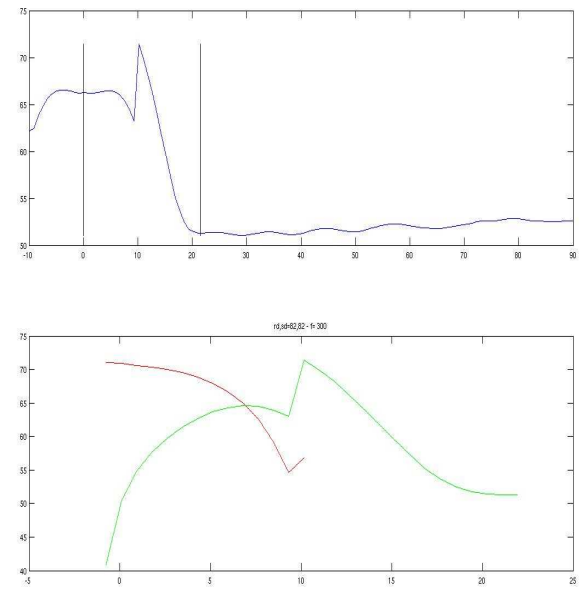

(a) Beamformer output for source/receiver at 82m depth

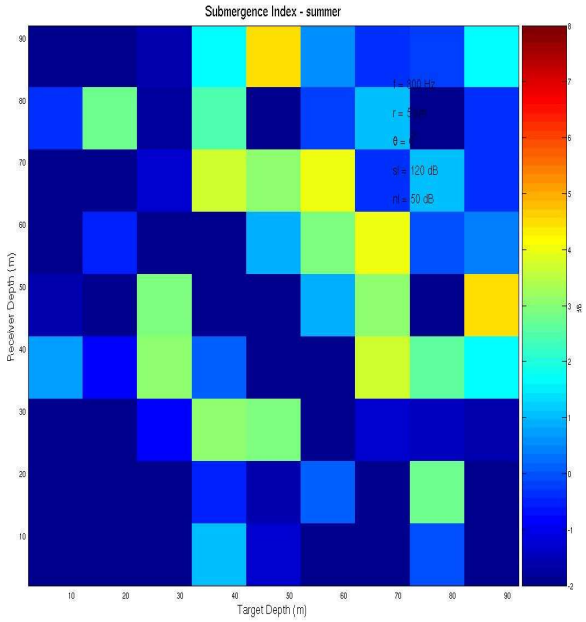

(b) SI for all depth/ receiver depth combinations

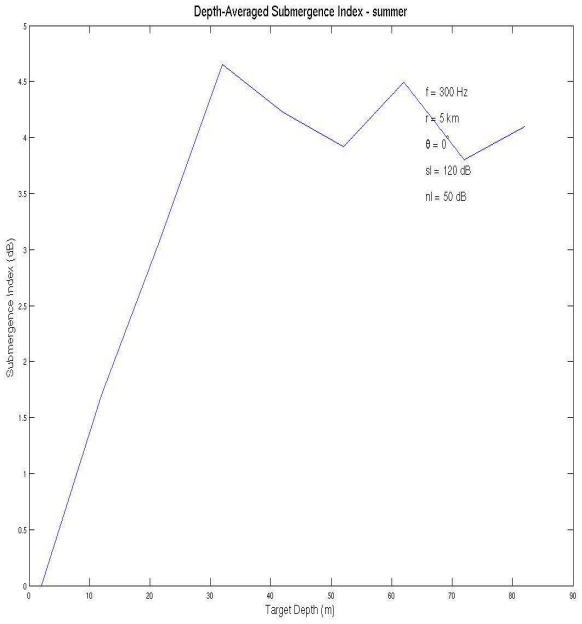

(c) Averaged receiver depth SI

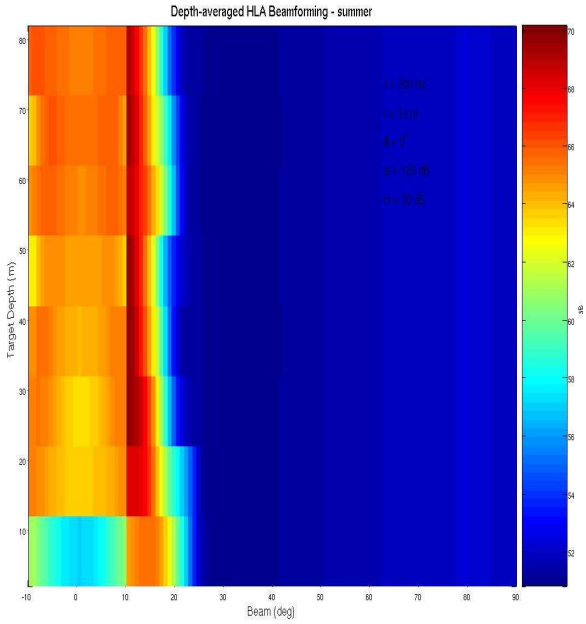

(d) Averaged receiver depth beamformer output

Figure 3.22: SI algorithm output for 300Hz source,$c_b = 1612\frac{m}{s}$, bearing 0^0, range $5km$

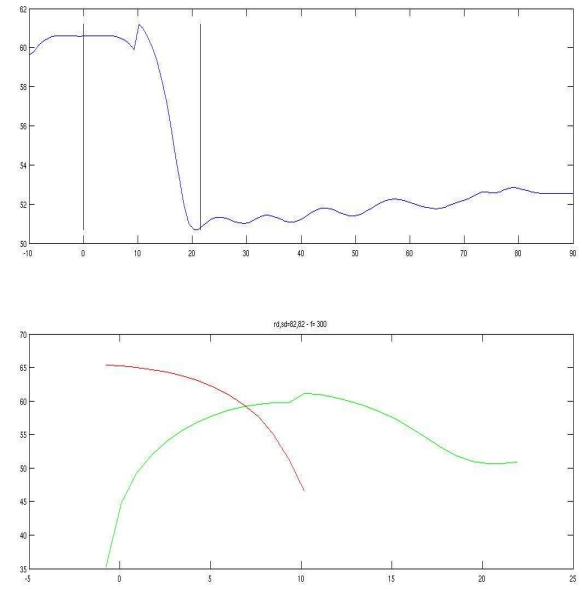

(a) Beamformer output for source/receiver at 82m depth

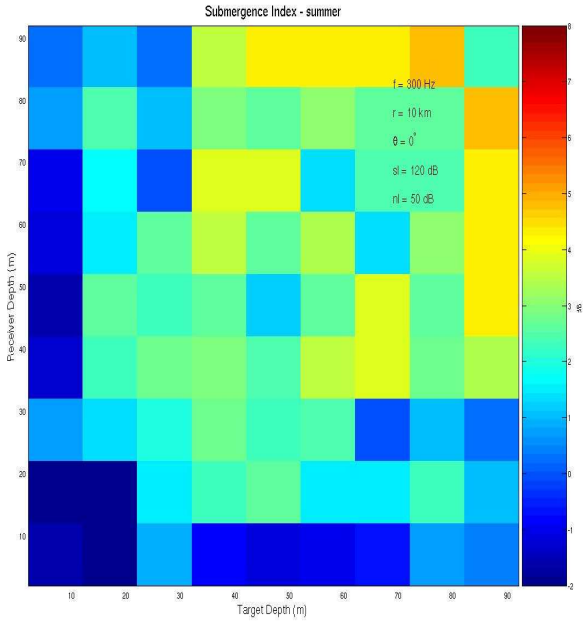

(b) SI for all depth/ receiver depth combinations

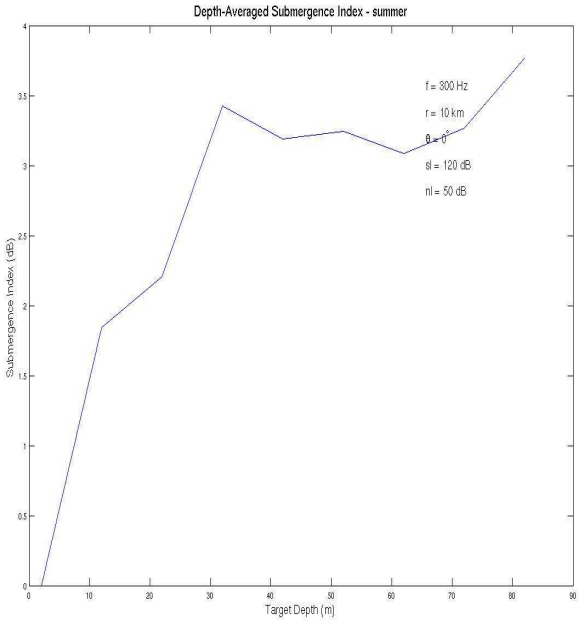

(c) Averaged receiver depth SI

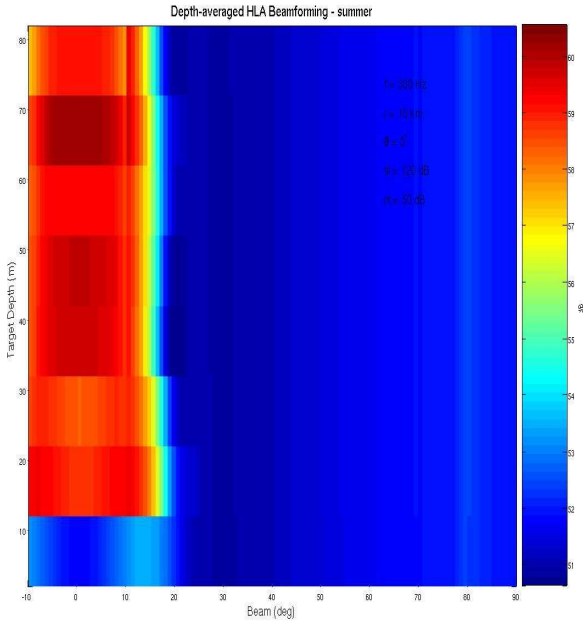

(d) Averaged receiver depth beamformer output

Figure 3.23: SI algorithm output for 300Hz source,$c_b = 1612\frac{m}{s}$, bearing 0^0, range $10km$

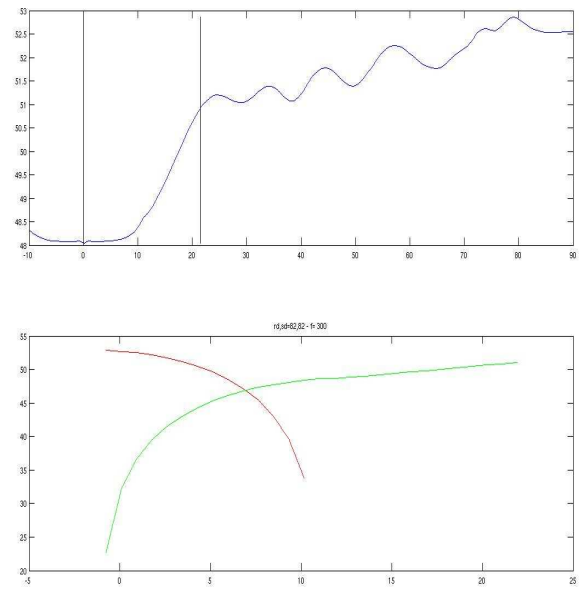

(a) Beamformer output for source/receiver at 82m depth

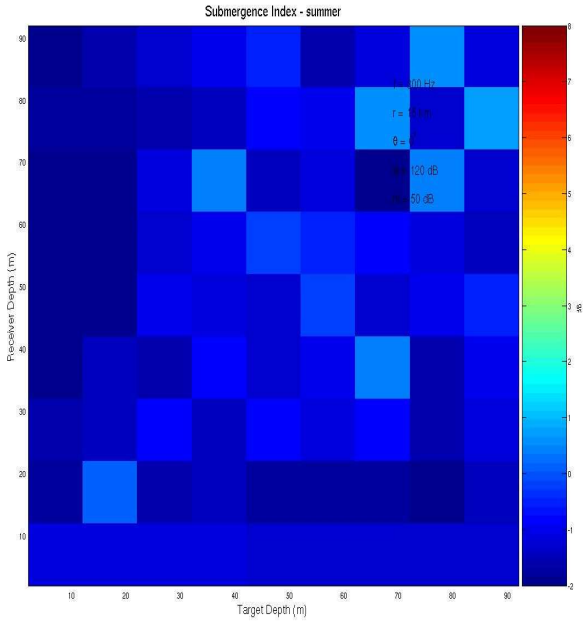

(b) SI for all depth/ receiver depth combinations

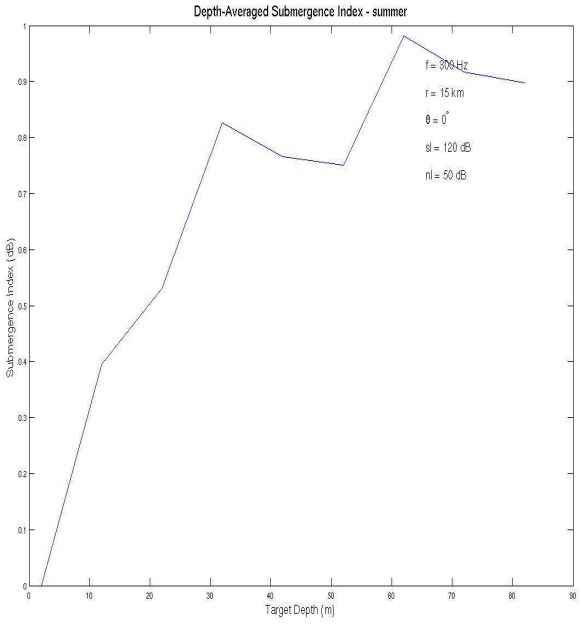

(c) Averaged receiver depth SI

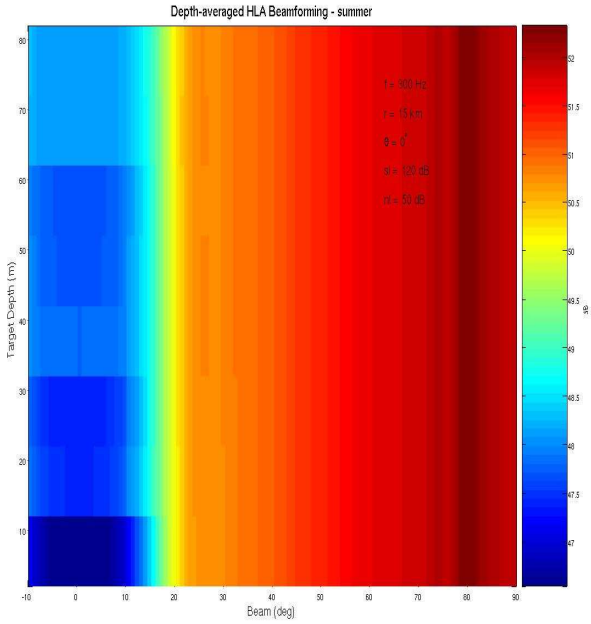

(d) Averaged receiver depth beamformer output

Figure 3.24: SI algorithm output for 300Hz source,$c_b = 1612\frac{m}{s}$, bearing 0^0, range $15km$

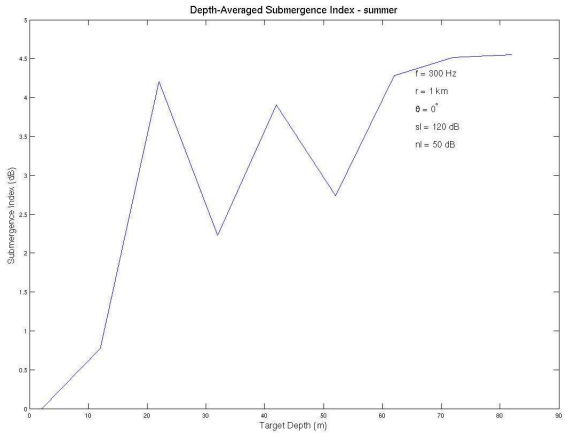

(a) Hanning window results

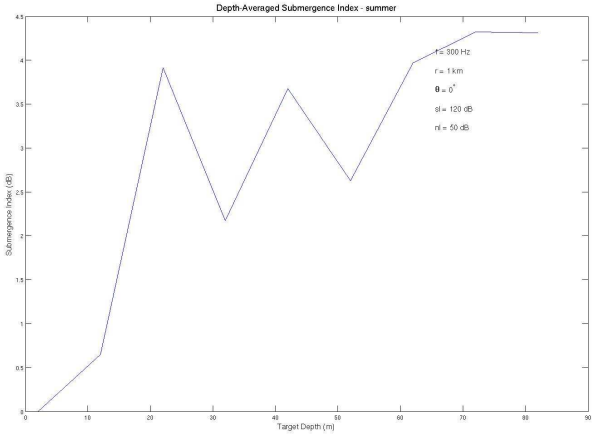

(b) Blackman-Harris window results

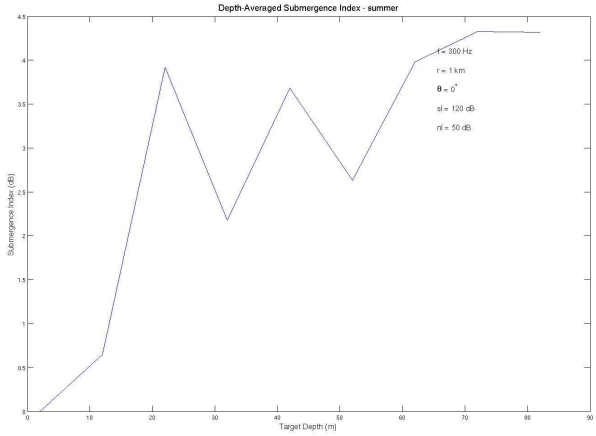

(c) Nutall's window results

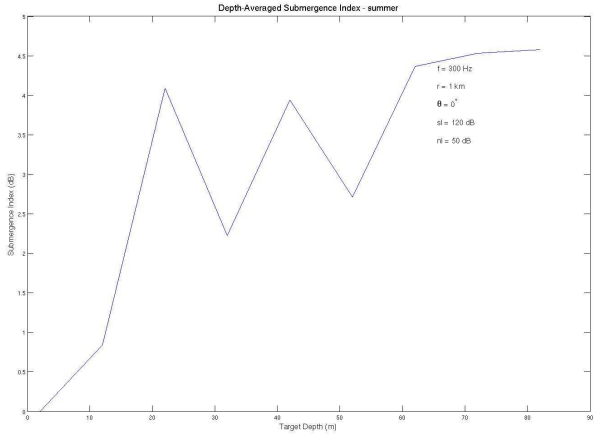

(d) Tringle window results

Figure 3.25: Averaged SI using different windows techniques for 300Hz source,$c_b = 1612\frac{m}{s}$, bearing 0^0, range $1km$

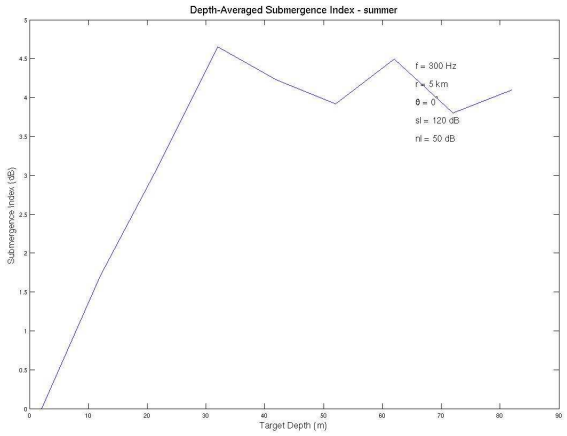

(a) Hanning window results

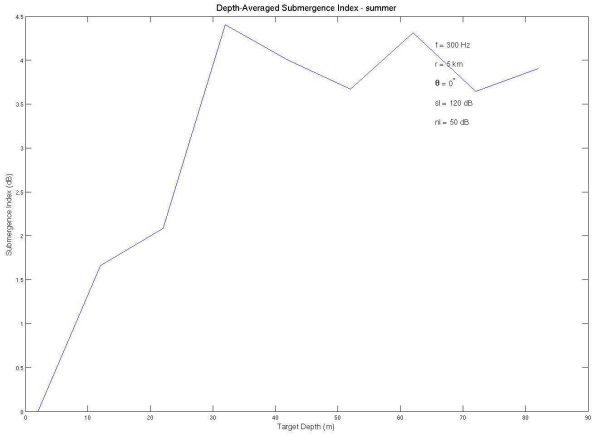

(b) Blackman-Harris window results

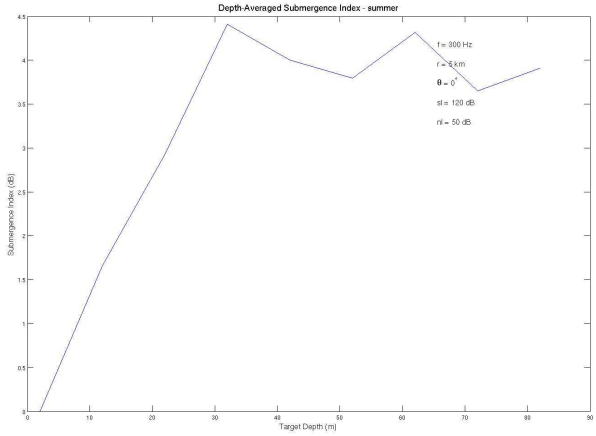

(c) Nutall's window results

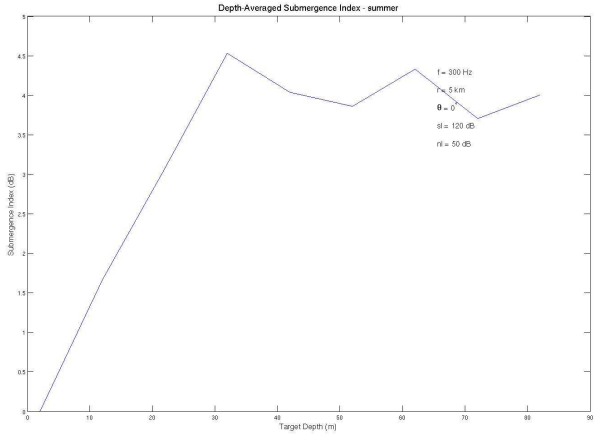

(d) Triangle window results

Figure 3.26: Averaged SI using different windows techniques for 300Hz source,$c_b = 1612\frac{m}{s}$, bearing 0^0, range $5km$

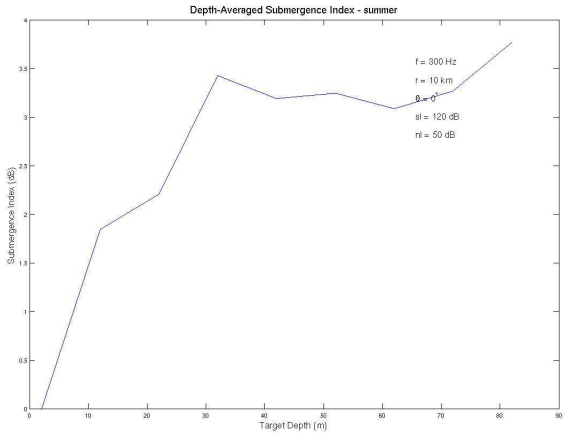

(a) Hanning window results

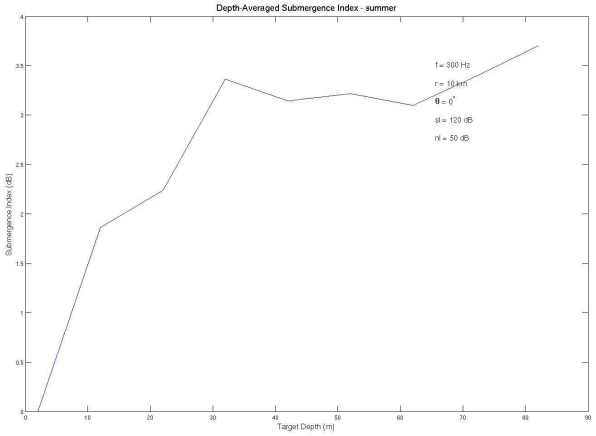

(b) Blackman-Harris window results

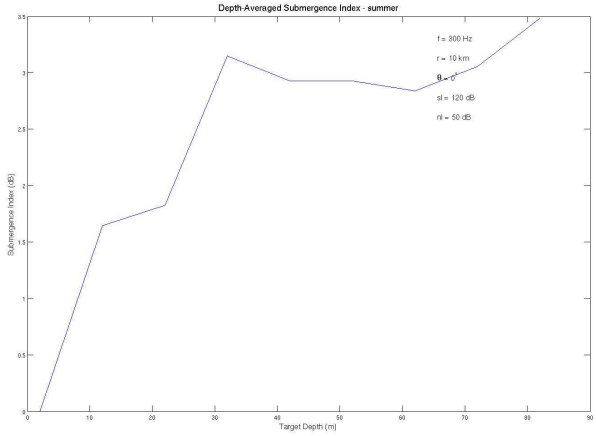

(c) Nutall's window results

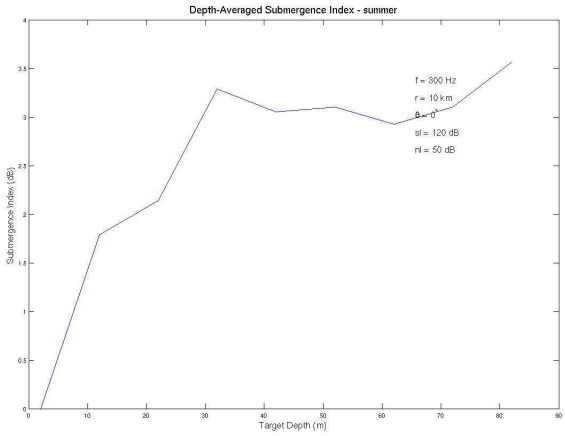

(d) Triangle window results

Figure 3.27: Averaged SI using different windows techniques for 300Hz source,$c_b = 1612\frac{m}{s}$, bearing 0^0, range $10km$

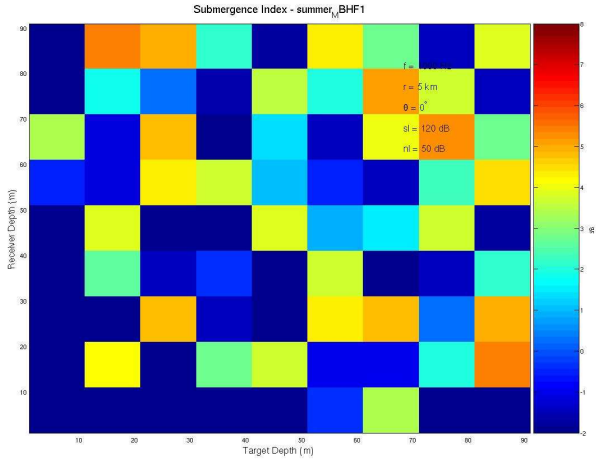

(a) SI for all depth/ receiver depth combinations

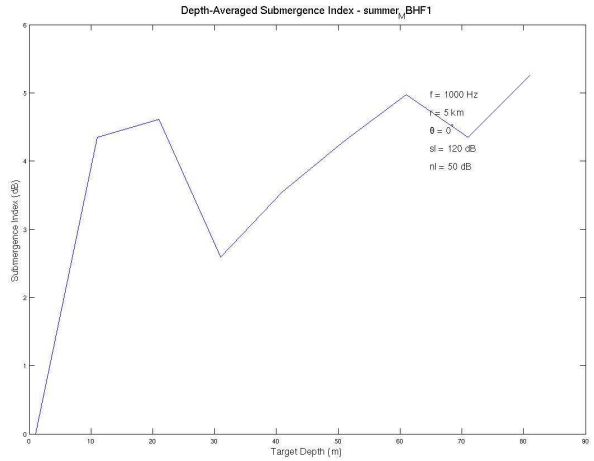

(b) Averaged receiver depth SI

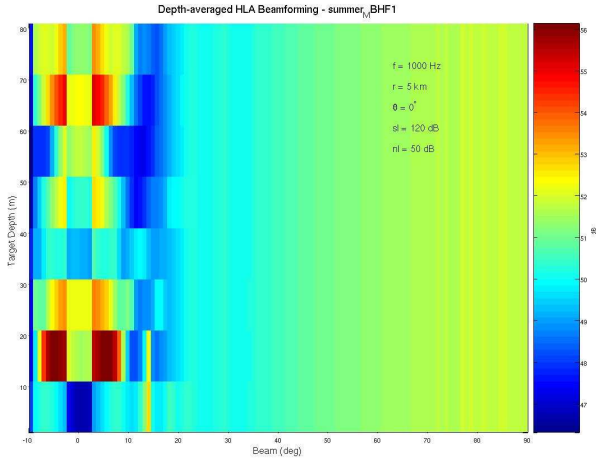

(c) Averaged receiver depth beamformer output

Figure 3.28: SI algorithm output for 1kHz source,$c_b = 1612\frac{m}{s}$, bearing 0^0, range $5km$

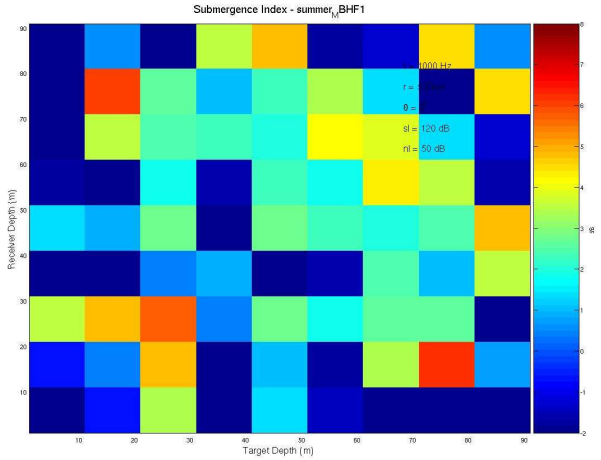

(a) SI for all depth/ receiver depth combinations

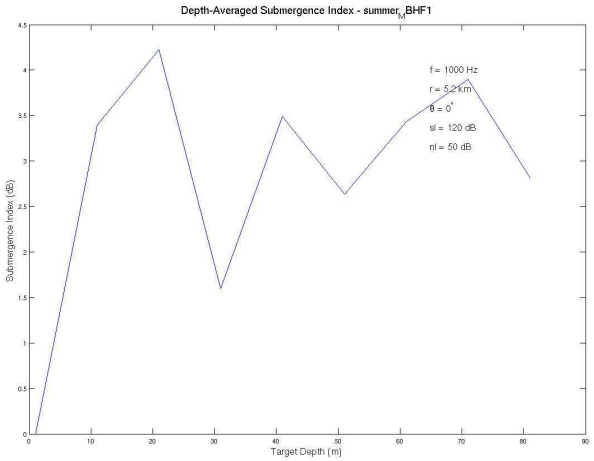

(b) Averaged receiver depth SI

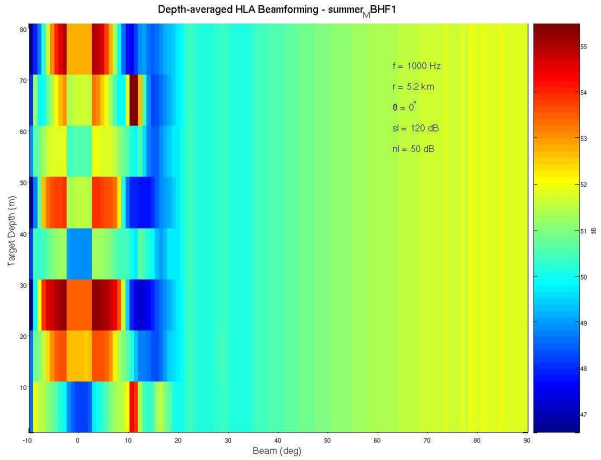

(c) Averaged receiver depth beamformer output

Figure 3.29: SI algorithm output for 1kHz source,$c_b = 1612\frac{m}{s}$, bearing 0^0, range $5.2km$

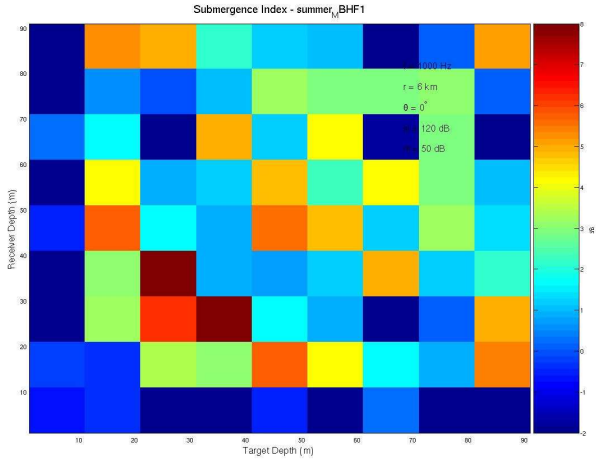

(a) SI for all depth/ receiver depth combinations

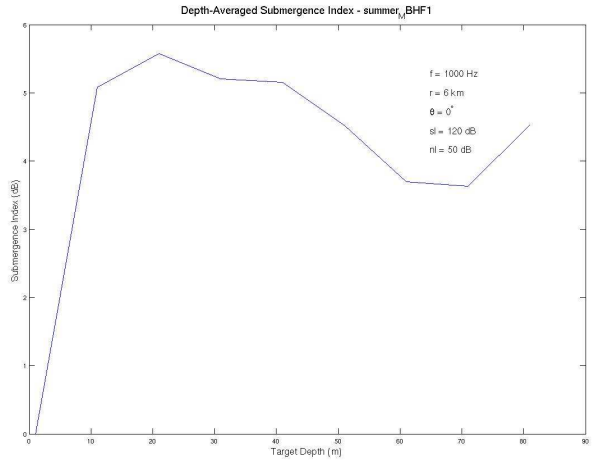

(b) Averaged receiver depth SI

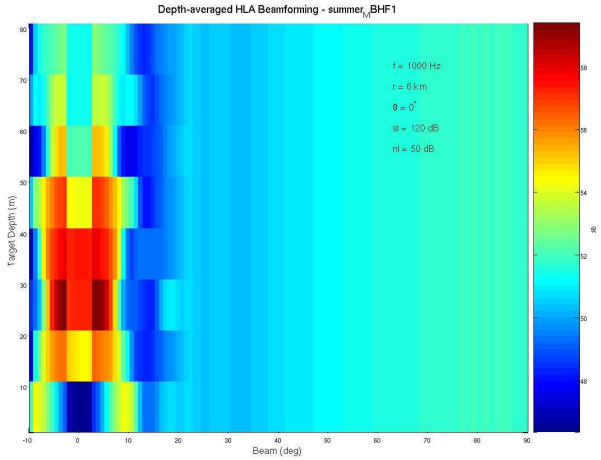

(c) Averaged receiver depth beamformer output

Figure 3.30: SI algorithm output for 1kHz source,$c_b = 1612\frac{m}{s}$, bearing 0^0, range $6km$

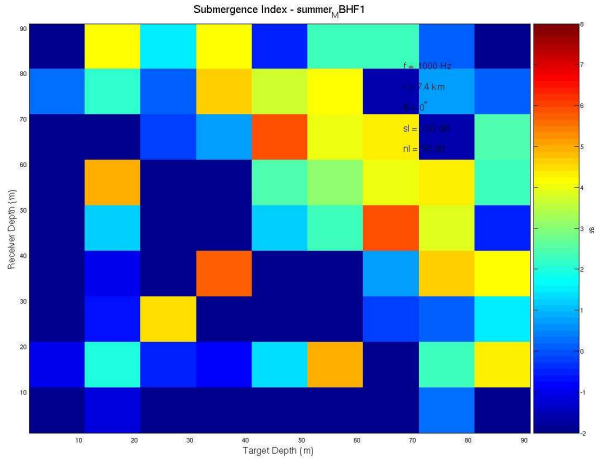

(a) SI for all depth/ receiver depth combinations

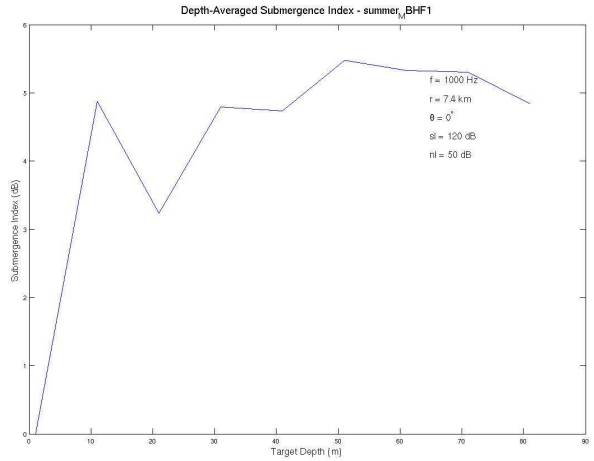

(b) Averaged receiver depth SI

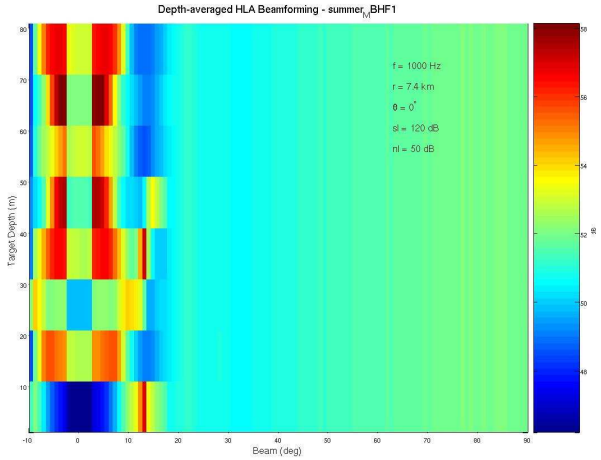

(c) Averaged receiver depth beamformer output

Figure 3.31: SI algorithm output for 1kHz source,$c_b = 1612\frac{m}{s}$, bearing 0^0, range $7.4km$

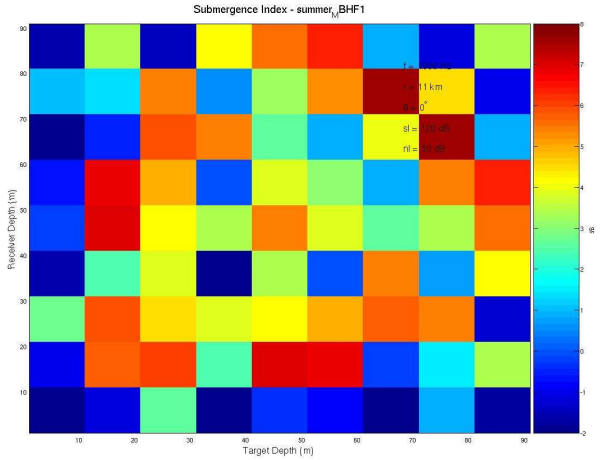

(a) SI for all depth/ receiver depth combinations

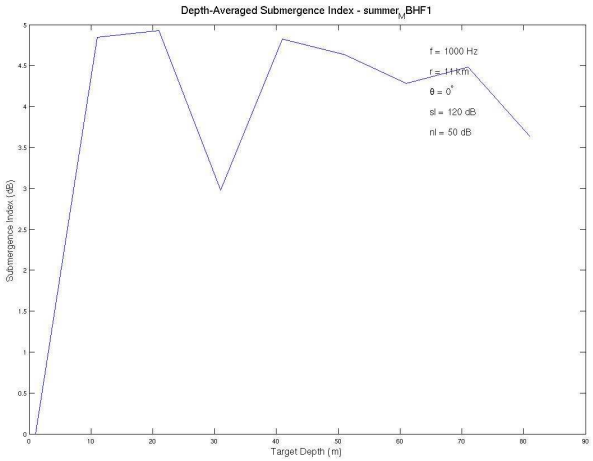

(b) Averaged receiver depth SI

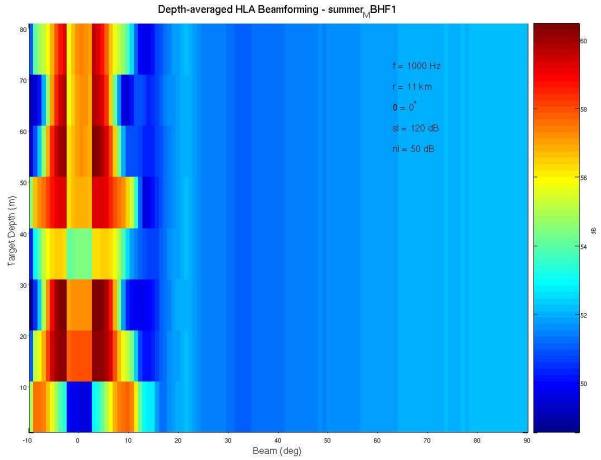

(c) Averaged receiver depth beamformer output

Figure 3.32: SI algorithm output for 1kHz source,$c_b = 1612\frac{m}{s}$, bearing 0^0, range $11km$

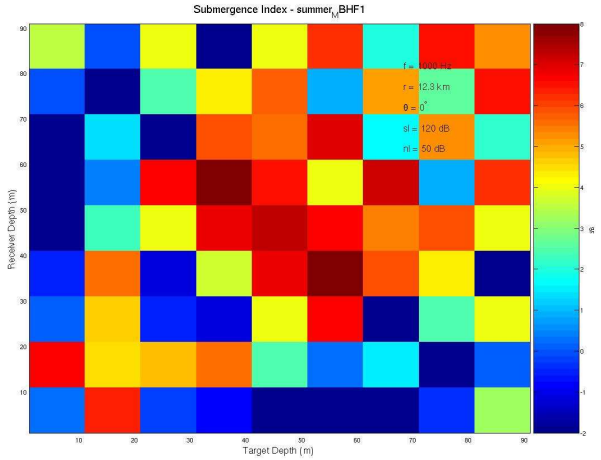

(a) SI for all depth/ receiver depth combinations

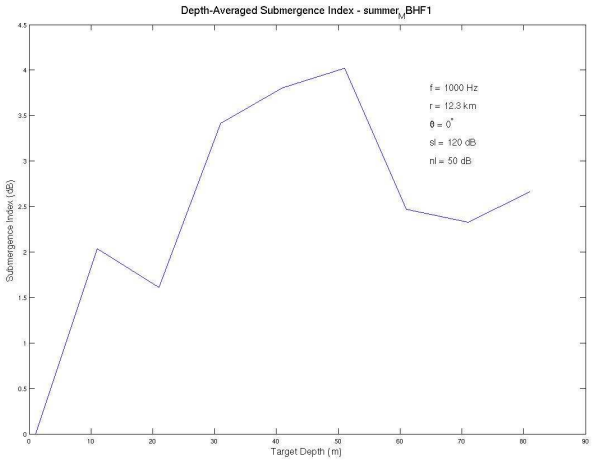

(b) Averaged receiver depth SI

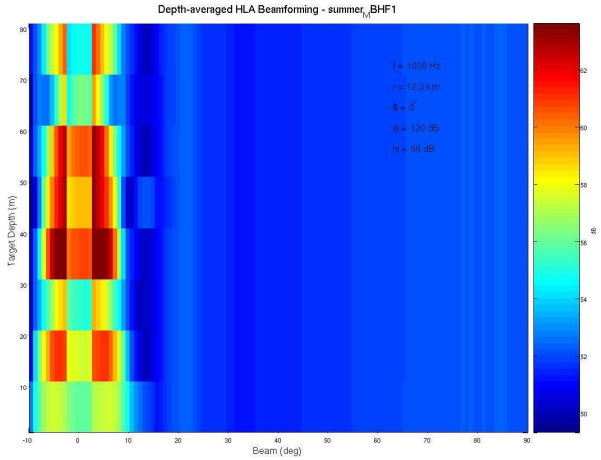

(c) Averaged receiver depth beamformer output

Figure 3.33: SI algorithm output for 1kHz source,$c_b = 1612\frac{m}{s}$, bearing 0^0, range $12.3km$

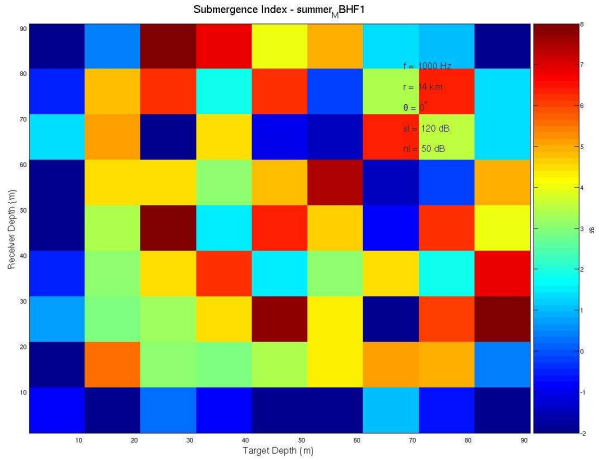

(a) SI for all depth/ receiver depth combinations

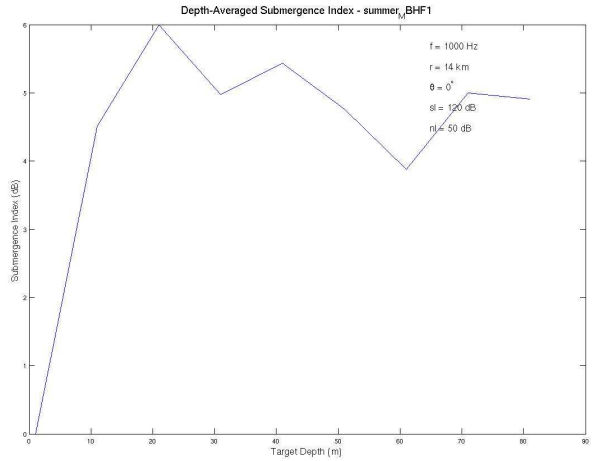

(b) Averaged receiver depth SI

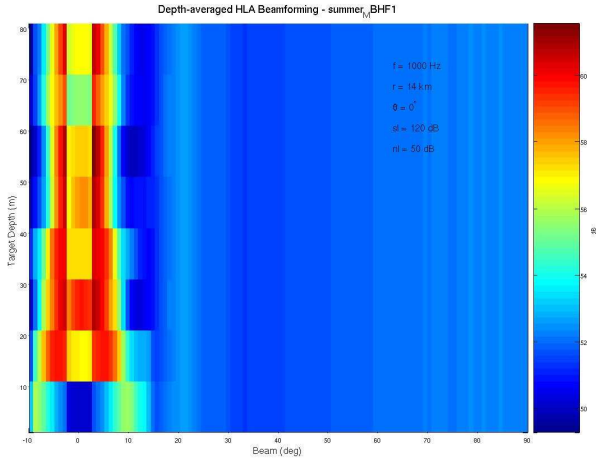

(c) Averaged receiver depth beamformer output

Figure 3.34: SI algorithm output for 1kHz source,$c_b = 1612\frac{m}{s}$, bearing 0^0, range $14km$

We tried to run a simulation for more range values but for all cases results were satisfying from an SI stability and a correct indication point of view.

Our next goal was to repeat the same procedure for 500Hz source. Simulation parameters were set as before, beside that a surface target was defined at 2m depth. Simulation results can be found in Fig. 3.35, 3.36, 3.37, 3.38, 3.39, 3.40, 3.41, 3.42.

The most interesting result is the one in Fig. 3.36. It is easy to notice that for a receiver which is separated from a target at 6km range it will be impossible to distinguish between a target at 2m depth and at 72m depth based on the averaged SI results. Both targets will look same if we will rely on SI analysis tools. This is an extreme version of the previously observed effect for a 300Hz target (Fig. 3.21). It can be seen also that the 'shadow' area is relatively short, the problem completely disappears for ranges of 5.9km and 6.1km, therefore we can assume existence of other 'shadow' areas that just hadn't been discovered yet. Our next step was to determine the extend of this area. From simulation results shown in Fig. 3.43, 3.44, 3.45 we found that boundaries of the area are 5.96km and 6.01km. So the total 'shadow' area is less than 50m long, therefore it can't be easily located.

Now we have to find what was a cause for misleading SI results almost exclusively in range of 6km and to suggest a robust solution. To understand the physics of the process we have to get back to a pressure field modal analysis. Total pressure field for 2m depth omnidirectional source and the same environmental parameters was derived using a KRAKEN simulation[5] and presented in Fig.3.46. Some pressure field value drops can be noticed around 6km range. To look at more detailed view of this area we are using close-up results displayed in Fig. 3.47 and Fig. 3.48. Now it seems even more definite that at the range of 6km the pressure field is non-consistent with other ranges. Some destructive inter-modal interference pattern could be assumed for the specific range or by using a ray terminology we can assume that a defocusing effect is observed.

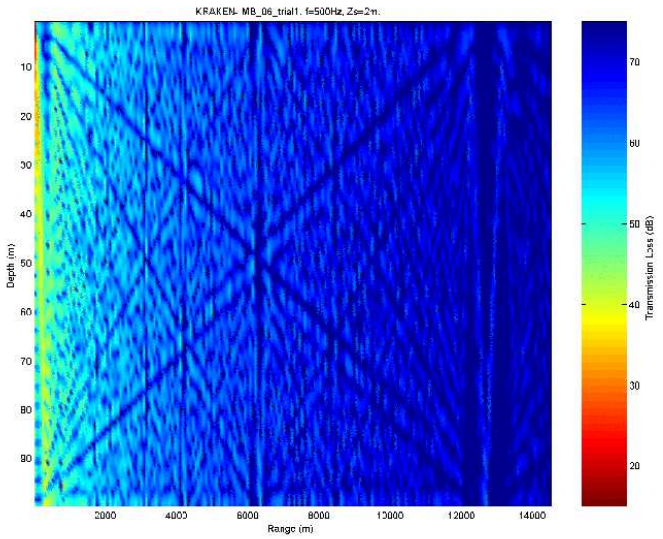

Figure 3.46: Total pressure field, 2m depth target, 500Hz

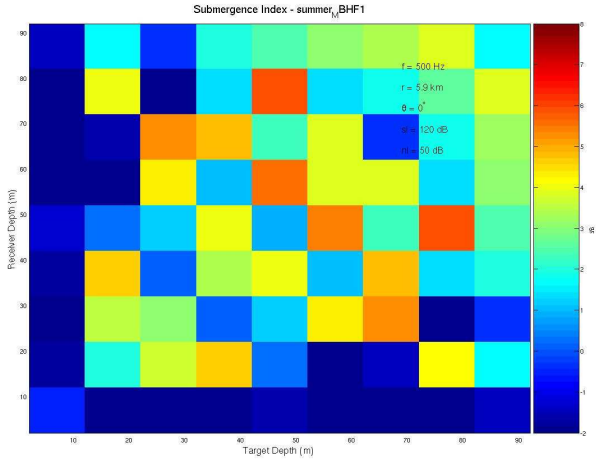

(a) SI for all depth/ receiver depth combinations

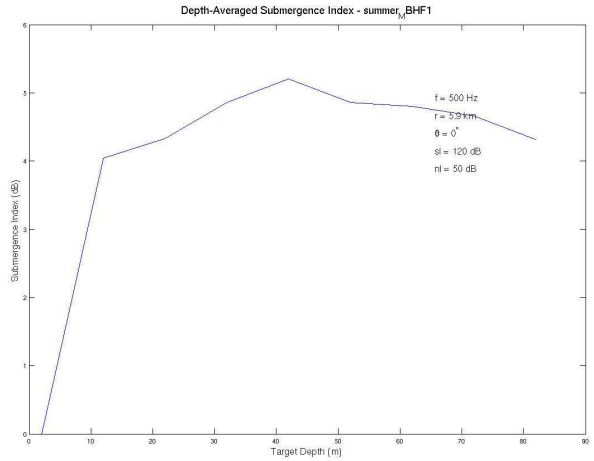

(b) Averaged receiver depth SI

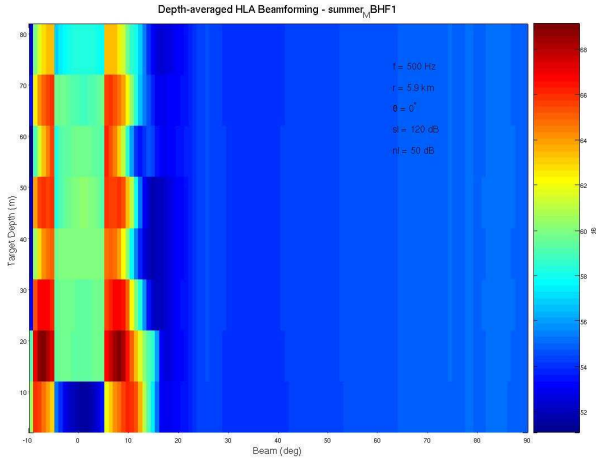

(c) Averaged receiver depth beamformer output

Figure 3.35: SI algorithm output for 500Hz source,$c_b = 1612\frac{m}{s}$, bearing 0^0, range $5.9km$

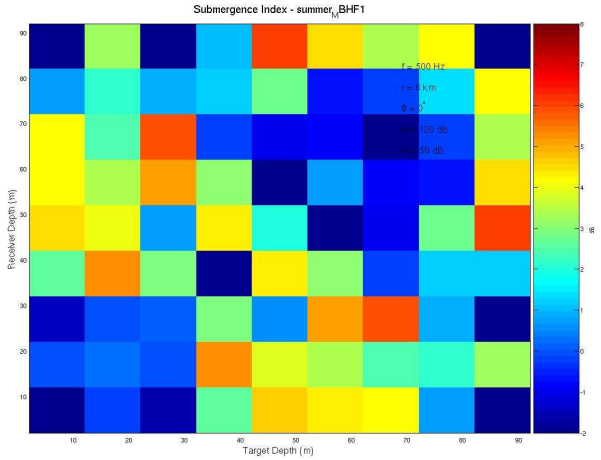

(a) SI for all depth/ receiver depth combinations

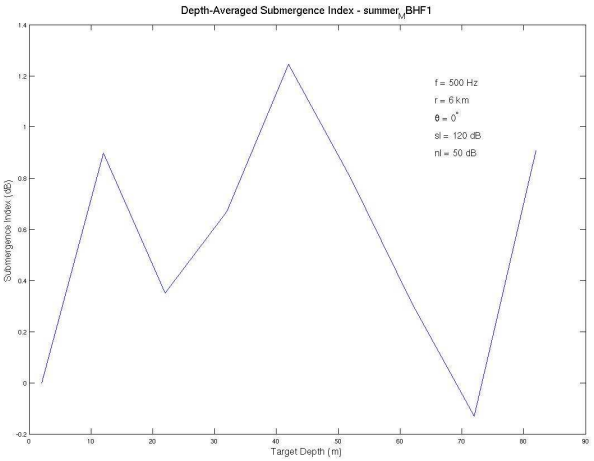

(b) Averaged receiver depth SI

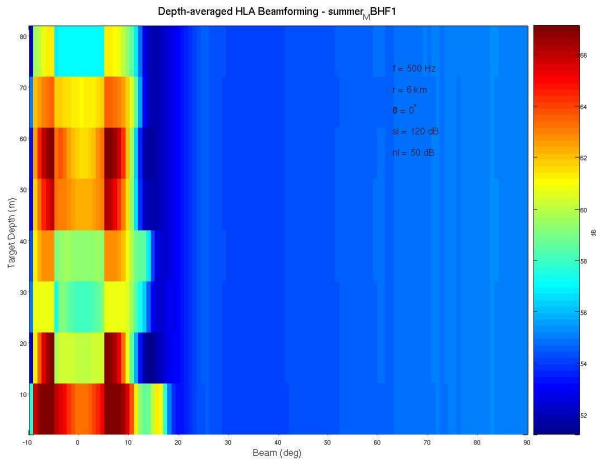

(c) Averaged receiver depth beamformer output

Figure 3.36: SI algorithm output for 500Hz source,$c_b = 1612\frac{m}{s}$, bearing 0^0, range $6km$

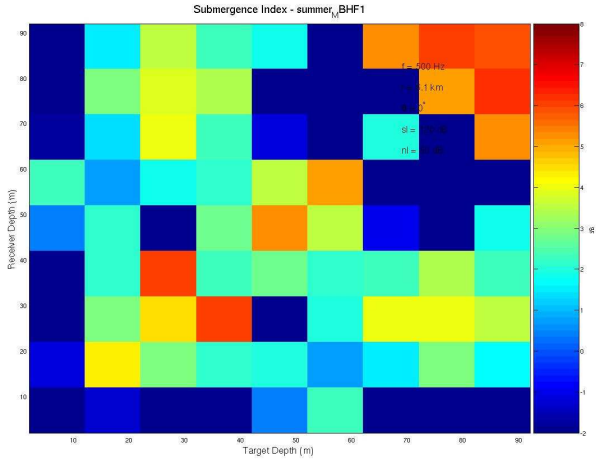

(a) SI for all depth/ receiver depth combinations

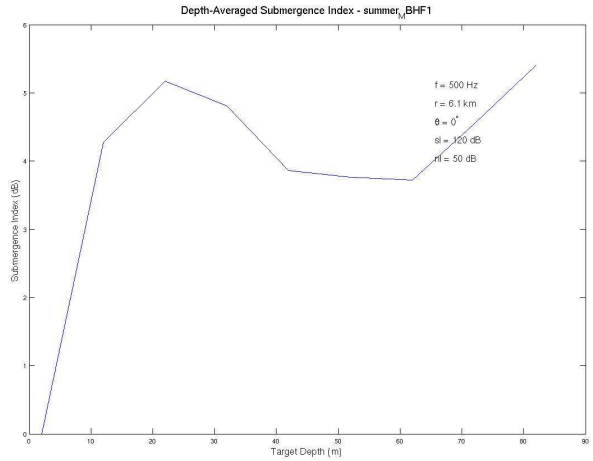

(b) Averaged receiver depth SI

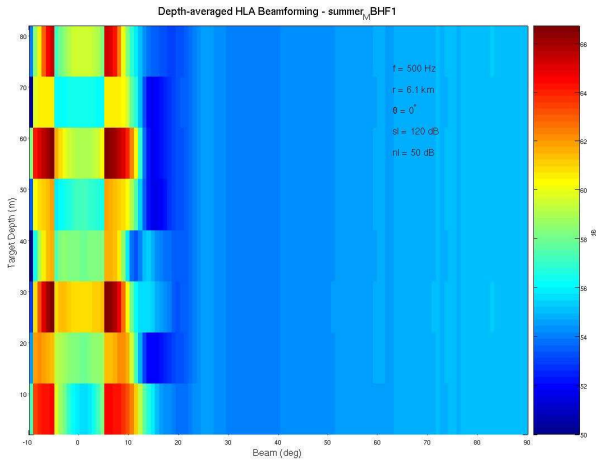

(c) Averaged receiver depth beamformer output

Figure 3.37: SI algorithm output for 500Hz source,$c_b = 1612\frac{m}{s}$, bearing 0^0, range $6.1km$

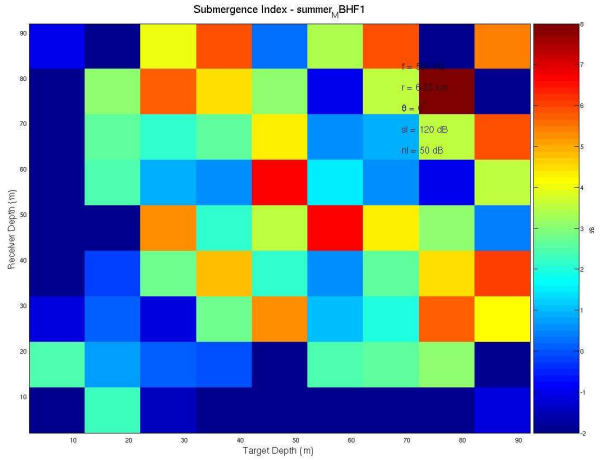

(a) SI for all depth/ receiver depth combinations

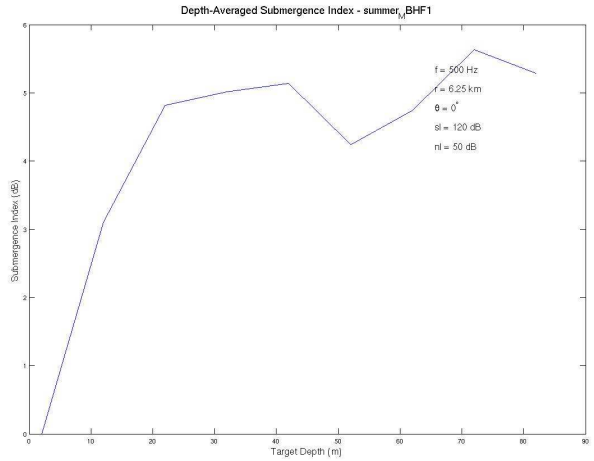

(b) Averaged receiver depth SI

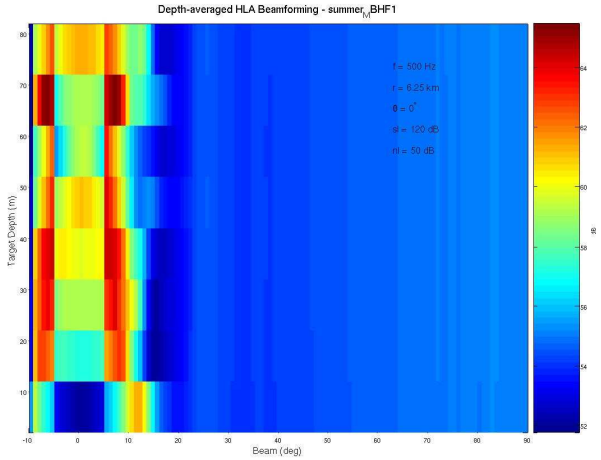

(c) Averaged receiver depth beamformer output

Figure 3.38: SI algorithm output for 500Hz source,$c_b = 1612\frac{m}{s}$, bearing 0^0, range $6.25km$

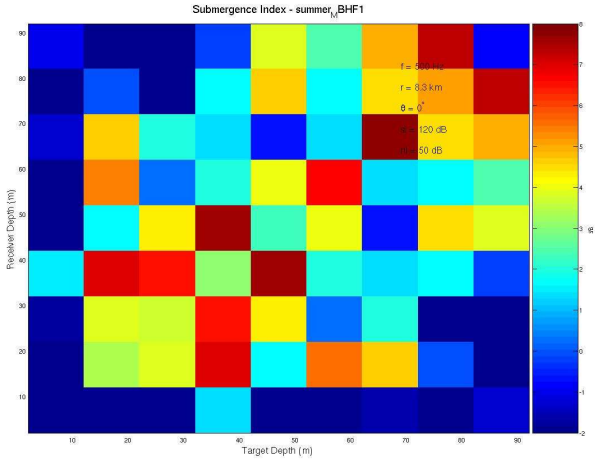

(a) SI for all depth/ receiver depth combinations

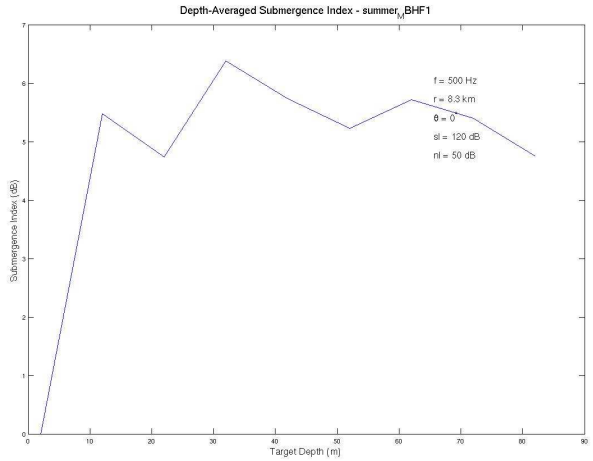

(b) Averaged receiver depth SI

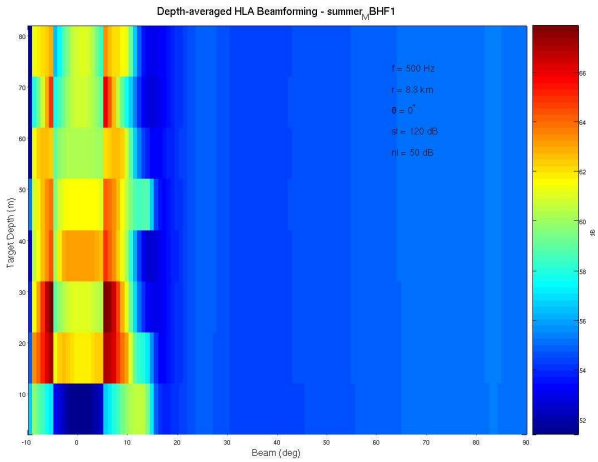

(c) Averaged receiver depth beamformer output

Figure 3.39: SI algorithm output for 500Hz source,$c_b = 1612\frac{m}{s}$, bearing 0^0, range $8.3km$

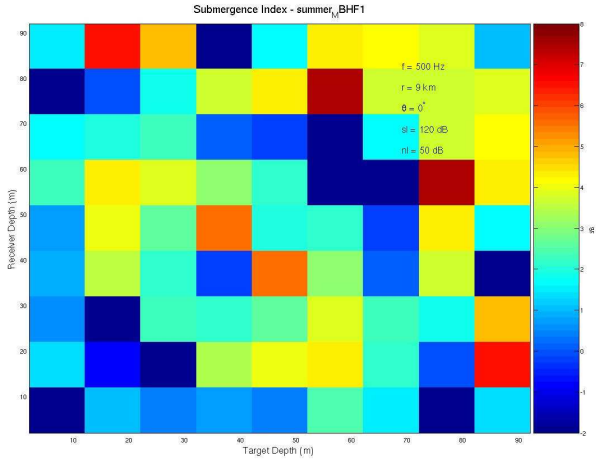

(a) SI for all depth/ receiver depth combinations

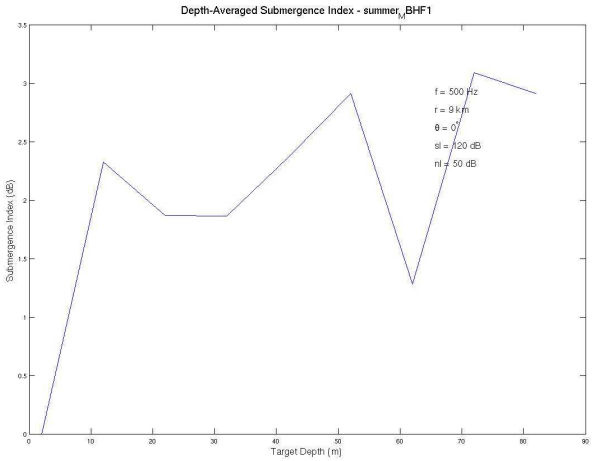

(b) Averaged receiver depth SI

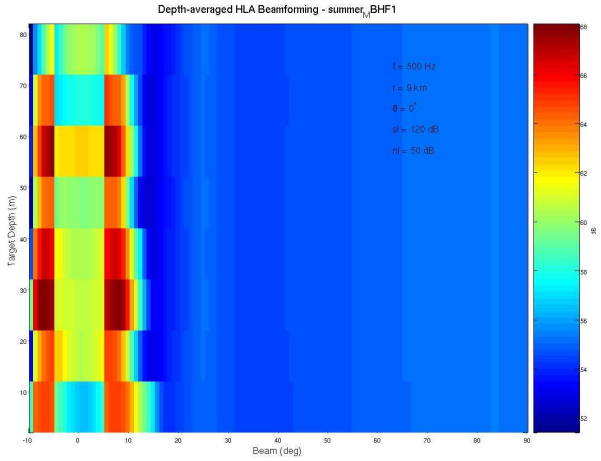

(c) Averaged receiver depth beamformer output

Figure 3.40: SI algorithm output for 500Hz source,$c_b = 1612\frac{m}{s}$, bearing 0^0, range $9km$

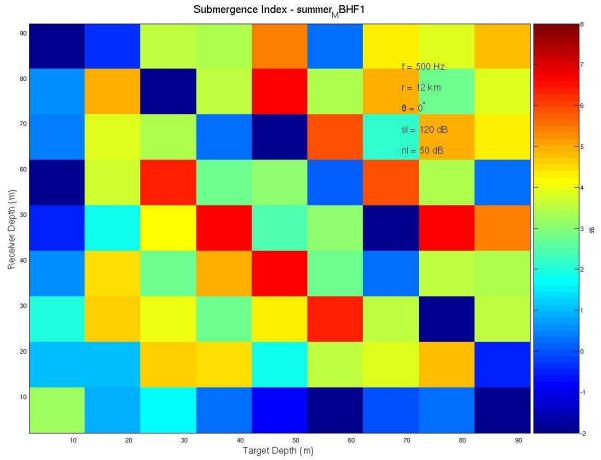

(a) SI for all depth/ receiver depth combinations

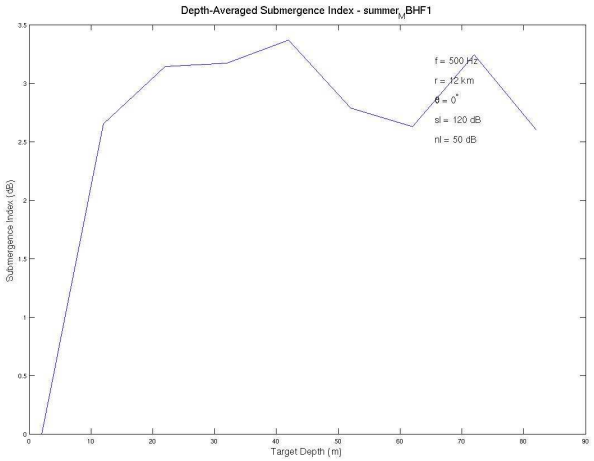

(b) Averaged receiver depth SI

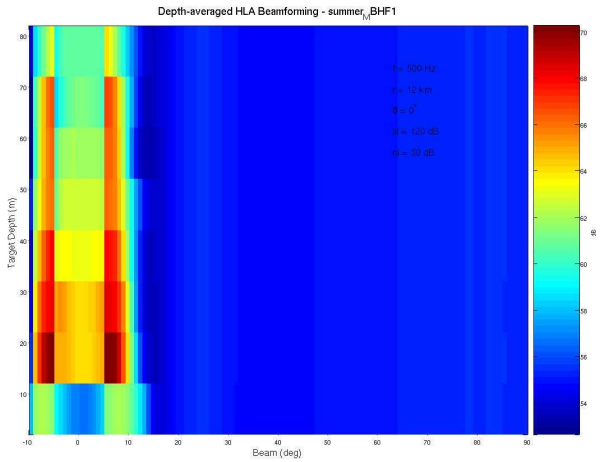

(c) Averaged receiver depth beamformer output

Figure 3.41: SI algorithm output for 500Hz source,$c_b = 1612\frac{m}{s}$, bearing 0^0, range $12km$

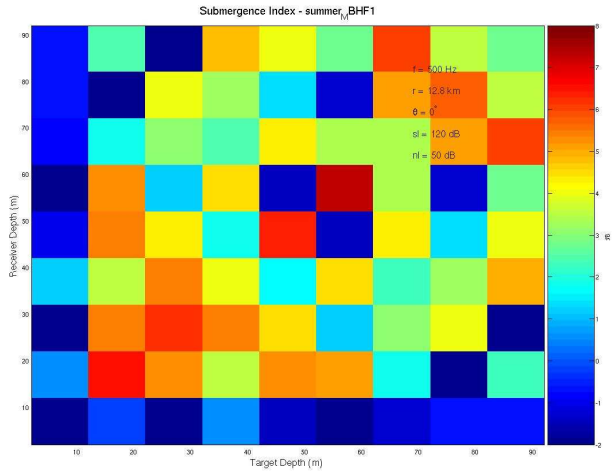

(a) SI for all depth/ receiver depth combinations

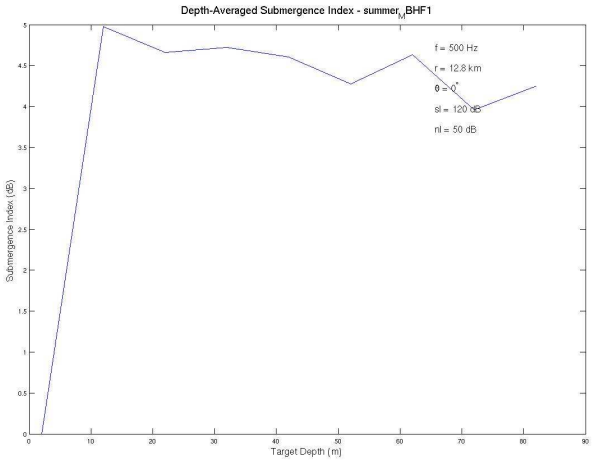

(b) Averaged receiver depth SI

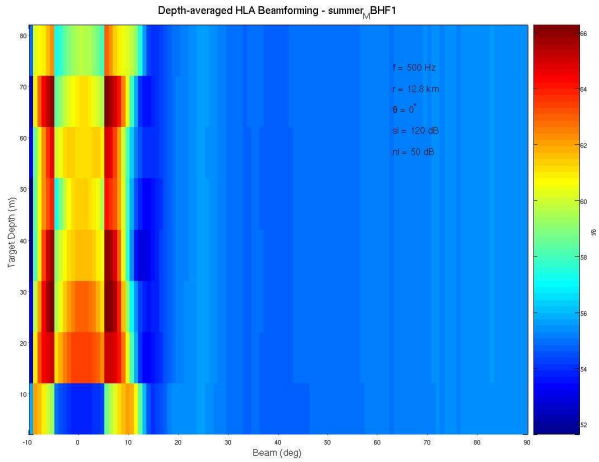

(c) Averaged receiver depth beamformer output

Figure 3.42: SI algorithm output for 500Hz source,$c_b = 1612\frac{m}{s}$, bearing 0^0, range $12.8km$

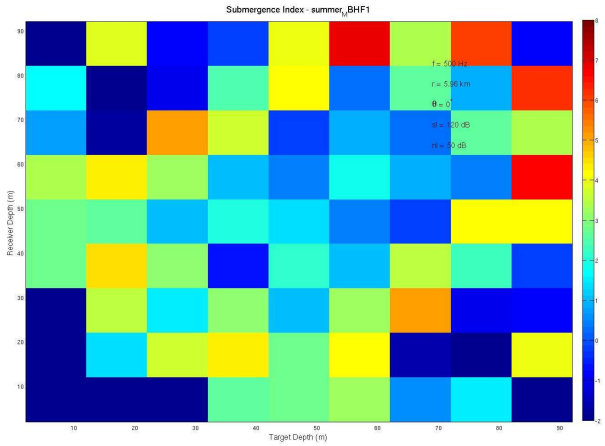

(a) SI for all depth/ receiver depth combinations

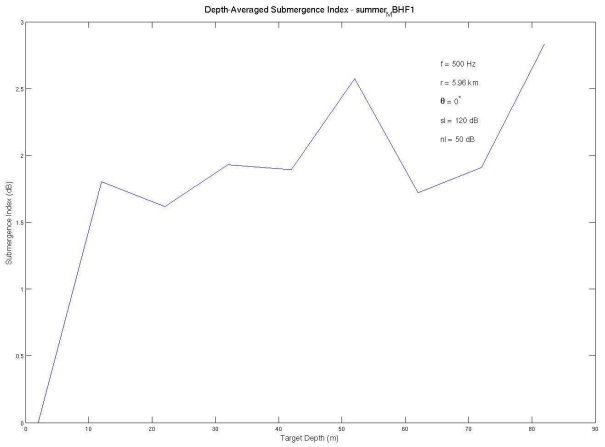

(b) Averaged receiver depth SI

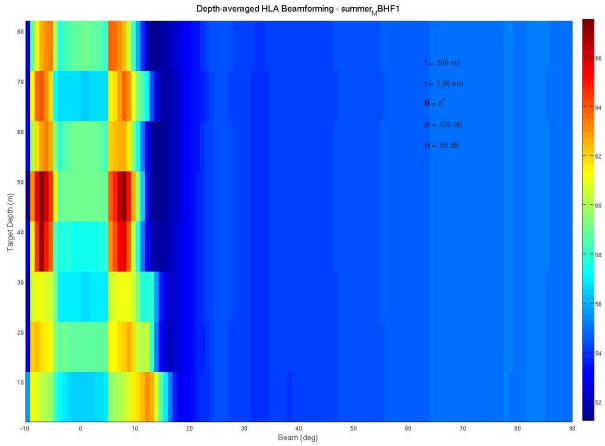

(c) Averaged receiver depth beamformer output

Figure 3.43: SI algorithm output for 500Hz source,$c_b = 1612\frac{m}{s}$, bearing 0^0, range $5.96km$

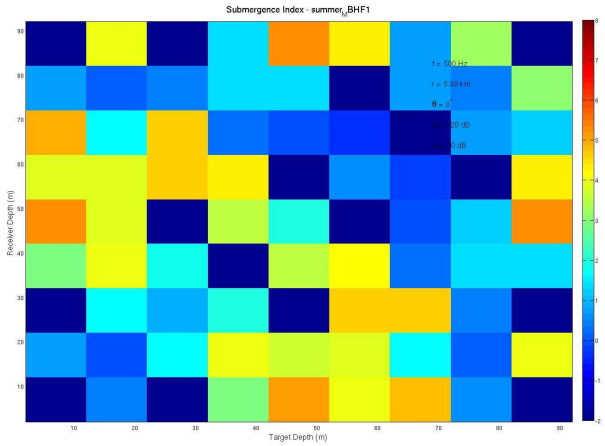

(a) SI for all depth/ receiver depth combinations

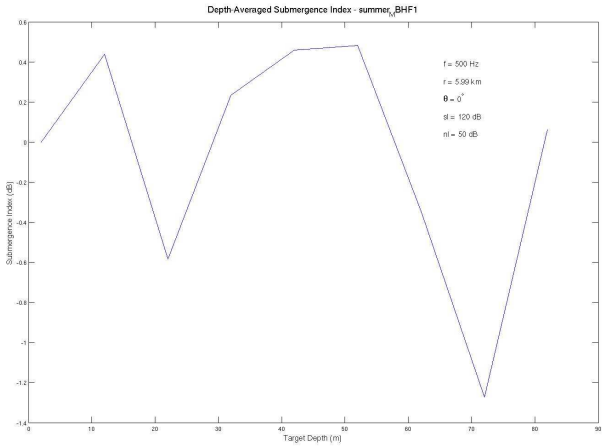

(b) Averaged receiver depth SI

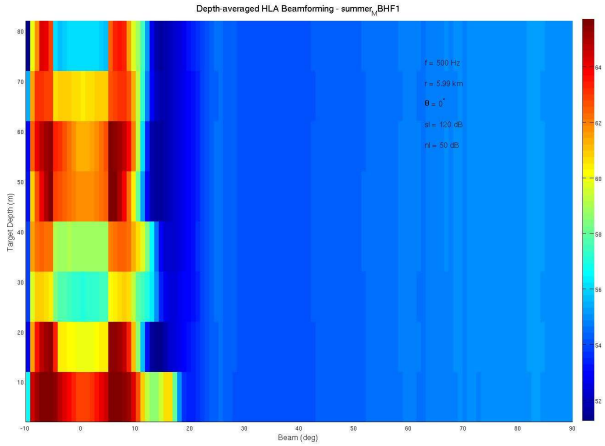

(c) Averaged receiver depth beamformer output

Figure 3.44: SI algorithm output for 500Hz source,$c_b = 1612\frac{m}{s}$, bearing 0^0, range $5.99km$

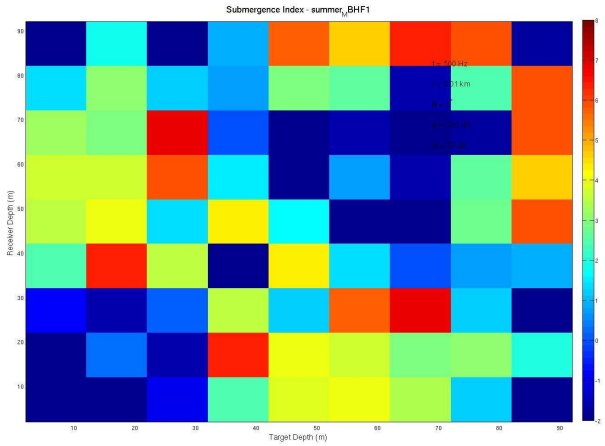

(a) SI for all depth/ receiver depth combinations

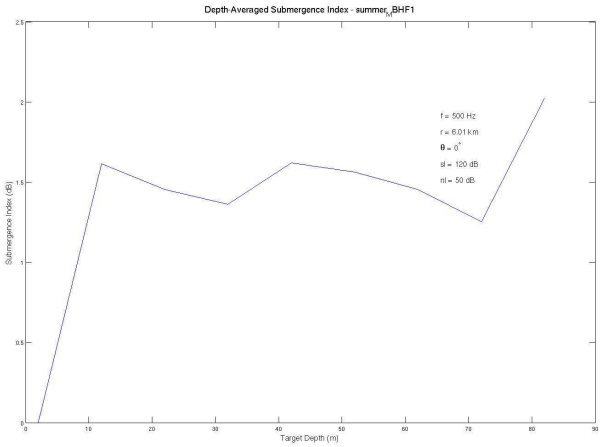

(b) Averaged receiver depth SI

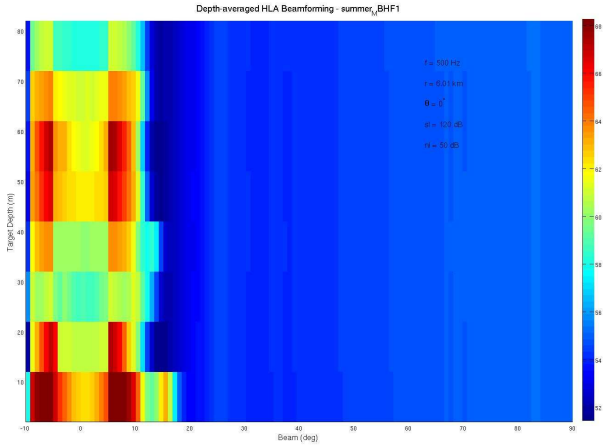

(c) Averaged receiver depth beamformer output

Figure 3.45: SI algorithm output for 500Hz source,$c_b = 1612\frac{m}{s}$, bearing 0^0, range $6.01km$

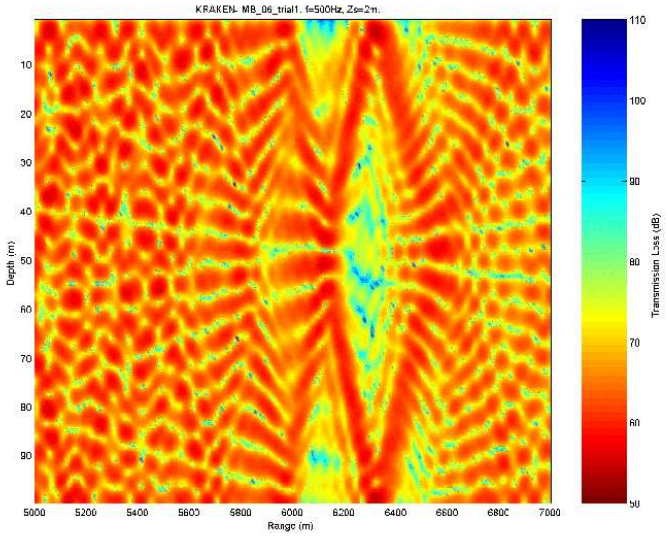

Figure 3.47: Pressure field,range 5-7km, 2m depth target, 500Hz

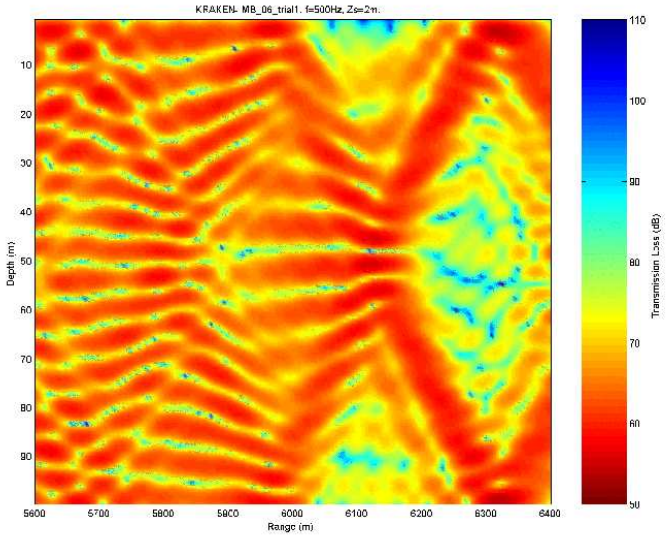

Figure 3.48: Pressure field,range 5.6-6.4km, 2m depth target, 500Hz

More accurate analysis is still required before further conclusions can be made regarding the robustness of SI. We need to look into the relative contribution to the total field of the low and high order modes. A Matlab code was written for this purpose. The total pressure field was decomposed to modes contribution functions using the orthogonality property. An absolute value of the averaged low to high modes ratio was calculated and displayed in Fig. 3.49. The same definition for high and low modes as in Sec. 3.1 was used. The results are very interesting. At range of 5.9-6.0 km a peak value of the ratio can be immediately examined, meaning strong attenuation of the high modes at the range of 5.9-6.0 km. Peak duration is relatively short at range,

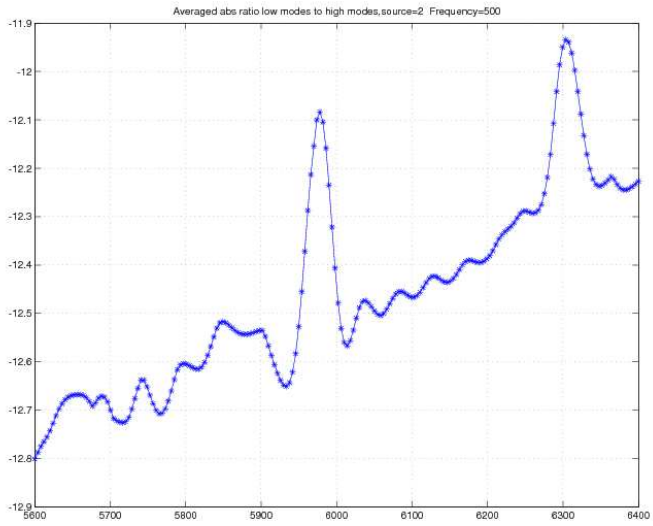

Figure 3.49: Averaged ratio $\frac{low}{high}$ modes [dB] ,range 5.6-6.4km, 2m depth target, 500Hz

$\sim 40m$, and it explains the reason for very short area of misleading SI results in the current case. A strong suppression of higher modes at this range explains also a pressure field value drop mentioned earlier.

To support our conclusions we can look at numerical results of an averaged beamformer output calculated by OASES for ranges surrounding 6km that are displayed in Table 3.5.

For every range case displayed values represent averaged beamformer output for each of target depth from 2m depth to 82m as a function of a steering angle between $-10^0 \div +10^0$. By looking at the values in an area of 0^0steering angle significant differences of $\sim 10dB$ can be noticed for surface (2m depth) target located in 5900m and 5980-6100m. The results are leading to the same conclusion. Non-consistent increasing of energy is concentrated in the lower modes relatively to the higher modes in range of 6km.

It is necessary to find a solution that will help to overcome the problem. As was already mentioned above (Fig. 3.9) the target evaluation relies on an SI averaging process of discrete receiver locations. We can try to improve our evaluation results in 'shadow' areas by increasing number of depth samplings in a water-column. We will divide a water-column into 20 stratified layers instead of 10 as it was until now. The trade-off will be obviously expressed by a calculation time growing.

The results of averaging through 20 layers for ranges 5.98/ 5.99/ 6.00 km are shown in Fig. 3.50, 3.51, 3.52.

The results show a separation of at least 1dB in SI values between a surface and a submerged target (a submerged target in this case will be defined as 7m source, following a decreasing of a depth sampling step value). Therefore a stratification to 20 layers will satisfy our requirements for SI separation capabilities even in the 'shadow' areas.

3.2.8 Receiver Depth-Range Averaging Process.

Until now we assumed that a submerging process is a vertical submerging with no changes in a range separation between an array and a source. In this section we will show results obtained by a more realistic scenario, in which AUV or any other submerged vehicle arrives to a pre-defined depth by a diving with some angle. This diving process will change not only a depth of the array but a range to the target as well. By taking into account changes in a range to the target we can estimate SI values based on depth-range averaging.

We already mentioned that the algorithm could be sensitive to a range changes. An increasing of the

	-10	-9.1597	-8.3193	-7.479	-6.6387	-5.7983	-4.958	-4.1176	-3.2773	-2.437	-1.5966	-0.7563	0.084034	0.92437	1.7647	2.605	3.4454	4.2857	5.1261	5.9664	6.8067	7.6471	8.4874	9.3277	10.168
5980m case																									
	60.595	66.007	65.464	64.736	63.854	62.96	55.256	53.887	52.985	52.343	51.909	51.648	51.443	51.564	51.765	52.103	52.619	53.349	61.996	63.117	64.081	64.916	65.593	66.069	66.021
	59.195	66.837	68.59	69.304	68.325	67.284	62.518	59.54	59.606	59.588	59.527	59.468	59.453	59.448	59.487	59.562	59.603	59.598	66.693	67.581	68.447	68.925	68.25	66.608	65.18
	53.295	66.388	66.665	66.506	66.506	65.988	61.029	59.587	59.633	59.6	59.537	59.481	59.454	59.455	59.49	59.545	59.591	59.587	65.622	66.392	66.815	66.9	66.578	64.944	62.179
	52.069	60.633	62.806	64.33	64.992	65.007	61.029	59.963	60.037	60.001	59.941	59.889	59.904	59.844	59.88	59.939	59.984	59.961	64.829	64.99	64.78	63.923	62.225	60.073	57.631
	52.138	63.849	65.614	66.781	66.737	66.796	64.481	59.067	59.327	59.646	60.079	60.163	60.143	60.04	59.834	59.539	59.231	59.587	66.969	65.668	65.625	65.818	65.189	63.298	61.008
	53.433	62.596	64.048	64.891	65.405	65.784	62.502	59.703	59.588	59.343	59.477	59.683	59.672	59.617	59.525	59.386	59.372	59.663	66.396	66.687	66.439	64.793	63.902	62.244	60.265
	52.485	59.934	61.536	62.968	64.356	64.664	62.905	59.417	59.776	59.302	59.477	59.305	58.305	58.332	58.284	58.162	57.962	57.665	63.309	63.373	63.518	62.76	61.219	59.636	58.602
	52.196	63.748	63.77	63.324	63.043	63.136	56.252	55.798	56.027	56.211	56.346	56.424	56.423	56.442	56.388	56.28	56.12	55.911	63.323	63.469	63.196	63.372	63.728	63.427	61.321
5980m case																									
	56.018	63.155	63.648	63.806	63814	63.778	63.268	62.579	62.132	61.652	61.225	60.946	60.776	60.807	61.026	61.365	61.809	62.287	63.714	63.777	63.81	63.777	63.578	62.986	61.787
	52.969	60.598	62.152	63.252	63.897	63.897	61.403	60.892	60.893	60.767	60.606	60.471	60.367	60.404	60.501	60.644	60.792	60.876	63.835	63.899	63.674	63.081	61.881	60.23	58.339
	53.331	59.397	59.57	59.936	60.018	59.961	58.587	56.786	56.91	56.916	56.676	56.815	56.786	56.814	56.943	56.864	56.796	59.938	62.045	62.507	62.805	63.095	62.814	61.459	59.605
	53.345	61.068	62.811	62.942	62.751	62.36	58.736	58.291	58.413	58.446	58.445	58.435	58.424	58.438	58.437	58.439	58.418	58.34	62.045	62.507	62.805	63.095	62.814	61.459	59.605
	52.724	61.068	63.179	64.61	66.317	66.46	62.316	61.342	61.342	61.128	60.904	60.731	60.621	60.655	60.769	60.956	61.18	61.366	65.366	65.412	65.169	64.366	62.816	60.589	57.897
	52.873	61.291	62.131	62.822	63.569	64.286	62.774	62.037	61.788	61.516	61.277	61.106	61.036	61.029	61.14	61.329	61.573	61.829	64.25	63.962	63.298	62.642	61.977	61.039	59.287
	54.794	61.646	63.132	63.872	63.46	62.607	60.992	59.935	59.943	59.863	59.613	59.454	59.341	59.377	59.5	59.679	59.869	59.965	61.919	62.552	62.713	61.287	60.049	59.311	57.607
	51.262	60.35	62.625	63.964	64.239	63.907	60.965	59.397	59.763	59.643	59.236	56.354	56.425	56.41	56.31	56.165	55.935	55.614	63.169	63.916	64.462	64.139	62.218	59.664	57.607
	53.188	58.416	60.521	62.781	63.928	64.248	59.593	57.164	57.574	57.883	58.093	58.214	58.271	58.262	58.184	58.034	57.79	57.441	64.503	64.406	63.628	62.302	60.039	58.014	56.744
5990m case																									
	56.695	64.43	65.539	66.516	66.596	66.596	65.317	64.801	64.337	63.819	63.339	62.98	62.803	62.86	63.08	63.487	63.989	64.501	65.506	65.587	66.008	66.487	65.1	64.205	62.751
	52.622	63.664	64.721	65.229	66.354	66.354	63.305	60.431	60.305	60.301	60.122	59.974	59.892	59.931	60.004	60.169	60.322	60.403	65.402	66.448	66.174	64.673	63.43	61.177	58.702
	53.795	59.689	60.062	60.226	60.559	60.408	58.454	57.729	57.618	57.452	57.343	57.276	57.127	57.251	57.266	57.303	57.394	57.527	60.301	60.363	60.565	60.621	60.349	59.279	57.969
	53.636	61.583	62.305	62.473	62.372	62.149	58.961	57.623	57.446	57.346	57.168	57.106	57.111	57.064	57.146	57.303	57.442	57.527	60.301	60.363	60.565	60.621	60.349	59.279	57.969
	54.899	63.716	65.126	66.194	66.977	66.823	63.716	62.802	62.467	62.242	62.019	61.845	61.795	61.777	61.879	62.232	62.459	62.707	65.716	65.767	65.376	64.342	63.294	62.253	60.385
	55.243	64.376	65.508	66.325	66.919	67.481	63.952	61.868	61.006	60.353	59.909	59.737	59.755	59.979	60.021	60.503	61.219	62.107	66.706	67.435	66.984	66.232	65.347	64.099	62.103
	53.125	60.827	62.861	64.034	64.823	65.114	63.716	62.802	62.467	62.242	62.019	61.845	61.795	61.777	61.879	62.232	62.459	62.707	65.716	65.767	65.376	64.342	63.294	62.253	60.385
	54.996	62.614	64.034	64.823	65.114	65.684	63.716	62.802	62.467	62.242	62.019	61.845	61.795	61.777	61.879	62.232	62.459	62.707	65.716	65.767	65.376	64.342	63.294	62.253	60.385
	52.895	62.617	63.895	65.145	64.555	63.091	56.323	55.572	55.685	55.792	55.881	55.942	55.972	55.961	55.929	55.859	55.759	55.645	63.34	63.736	64.859	64.55	63.439	61.768	59.837
	52.786	59.366	60.533	62.717	64.995	66.761	57.462	56.545	56.739	56.876	56.959	57.012	57.035	57.037	56.985	56.918	56.806	56.637	64.632	65.596	64.532	62.467	60.081	57.988	56.133
6010m case																									
	57.266	63.375	63.848	64.168	64.36	64.459	64.294	59.847	58.929	56.216	55.768	55.318	55.553	55.906	56.44	57.222	58.186	64.395	64.442	64.332	64.101	63.771	63.256	62.453
	54.499	61.833	62.167	61.848	61.711	61.431	59.536	59.077	58.818	58.542	58.308	58.144	58.089	58.144	58.314	58.614	58.879	61.471	61.75	62.104	62.196	62.229	61.504	59.649	57.896
	52.987	60.943	63.151	64.924	66.066	66.436	61.958	61.303	61.291	61.131	60.959	60.808	60.745	60.769	60.848	60.98	61.135	61.244	66.442	66.432	65.847	64.898	62.725	60.414	58.029
	49.979	56.496	58.93	60.593	61.339	61.649	58.483	58.325	58.437	58.328	58.066	58.066	58.094	58.157	58.337	58.269	61.757	61.703	65.716	65.376	64.363	63.764	61.69	58.846	56.321
	58.151	64.232	65.114	66.121	66.465	66.023	63.428	60.767	60.048	59.502	59.162	58.973	58.923	59.024	59.243	59.64	60.243	66.657	66.875	66.383	65.311	63.764	63.023	62.076	58.963
	50.475	59.724	60.466	60.891	60.636	60.611	56.964	56.095	56.167	56.273	56.375	56.447	56.522	56.473	56.397	56.291	56.147	55.994	60.54	60.628	60.648	60.65	60.431	59.494	57.771
	53.979	59.467	60.514	62.767	64.348	65.055	58.909	57.914	58.56	59.107	59.4	59.522	59.839	59.404	59.494	59.273	58.886	58.287	65.35	65.734	64.262	62.452	60.046	58.116	56.879
	51.279	57.861	59.928	61.593	62.424	62.786	58.065	57.091	57.792	58.342	58.666	58.596	59.03	58.824	58.544	58.417	58.06	57.442	63.232	62.941	62.231	61.27	59.665	57.441	55.685
6300m case																									
	54.339	57.685	56.515	55.534	54.644	53.86	50.633	49.984	49.618	49.335	49.133	49.009	48.966	48.993	49.094	49.275	49.53	49.864	53.39	54.048	54.826	55.718	56.718	57.911	59.292
	54.046	63.312	64.669	65.171	65.143	64.804	63.86	59.659	59.291	59.042	58.871	58.76	58.695	58.711	58.783	58.901	59.074	59.313	64.566	64.906	65.155	65.1	64.65	63.141	60.519
	54.864	61.779	62.728	63.212	63.229	63.095	61.459	60.214	60.3	60.123	59.897	59.741	59.657	59.745	59.916	60.117	60.222	62.917	63.165	63.296	63.114	62.579	61.519	59.853	
	52.178	62.178	64.148	64.519	63.897	63.121	59.316	59.508	59.517	58.471	58.413	58.363	58.34	58.375	58.472	58.424	58.49	62.718	63.467	63.987	64.471	63.87	61.885	59.907	
	51.572	59.195	61.571	63.896	63.839	63.227	59.055	57.777	57.91	57.925	57.804	57.863	57.871	57.902	57.913	57.866	62.496	64.322	64.287	63.606	62.377	60.867	59.743	58.746	56.607
	52.036	59.907	61.149	62.707	63.844	64.309	57.847	57.316	57.596	57.804	57.938	58.009	58.042	58.028	57.981	57.88	57.711	57.457	63.177	64.995	63.547	61.884	59.746	58.964	
	51.304	56.4	57.833	59.025	59.882	60.452	58.508	58.107	58.104	58.177	58.189	58.143	58.428	58.257	58.101	58.09	58.016	57.871	60.63	60.341	59.721	58.8	57.866	56.104	54.7
	52.024	62.693	62.945	64.338	64.62	63.352	57.114	57.104	57.617	57.965	58.185	58.309	58.367	58.345	58.266	58.107	57.84	57.429	62.823	63.472	64.263	64.379	62.943	62.562	61.342
	52.896	58.28	60.054	61.663	62.36	62.78	61.527	59.266	59.862	60.046	60.029	59.93	59.792	59.891	59.922	59.958	59.913	59.625	63.077	62.738	62.248	61.206	59.689	59.09	57.622

Table 3.5: Receiver depth averaged beamformer values [dB] for steering angle $-10^0 \div +10^0$

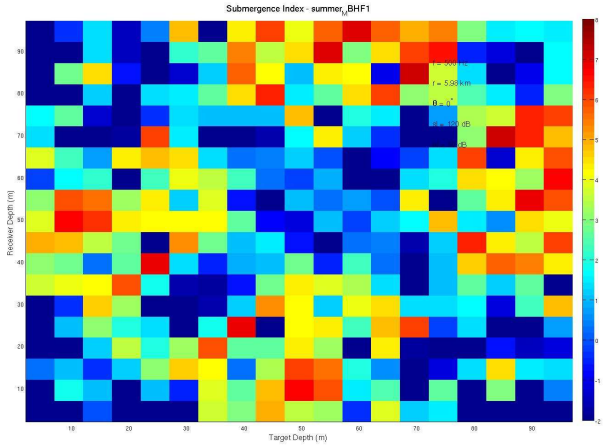

(a) SI for all depth/ receiver depth combinations

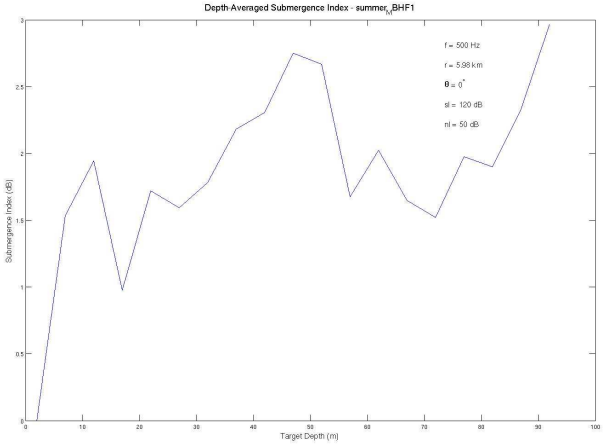

(b) Averaged receiver depth SI

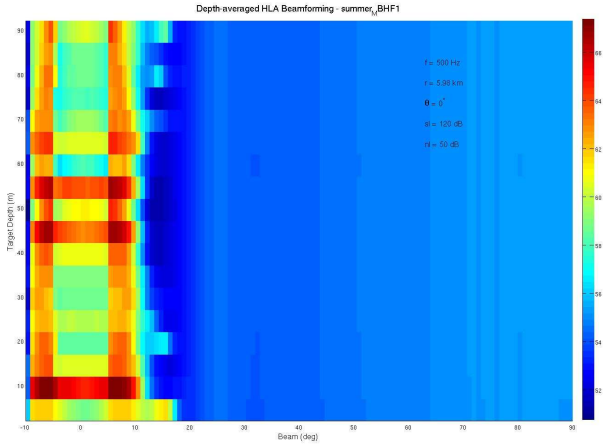

(c) Averaged receiver depth beamformer output

Figure 3.50: SI algorithm output for 500Hz source, 20 layers averaging, range 5.98km

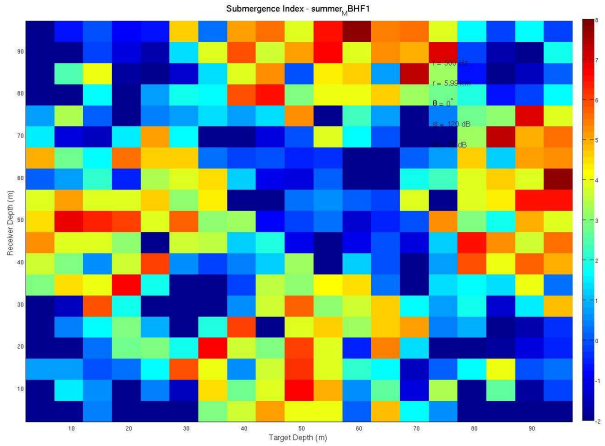

(a) SI for all depth/ receiver depth combinations

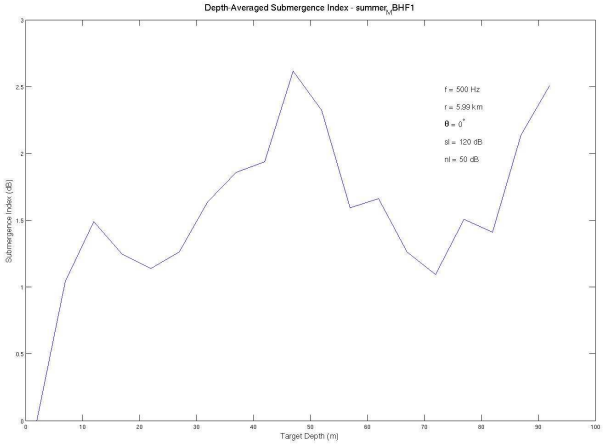

(b) Averaged receiver depth SI

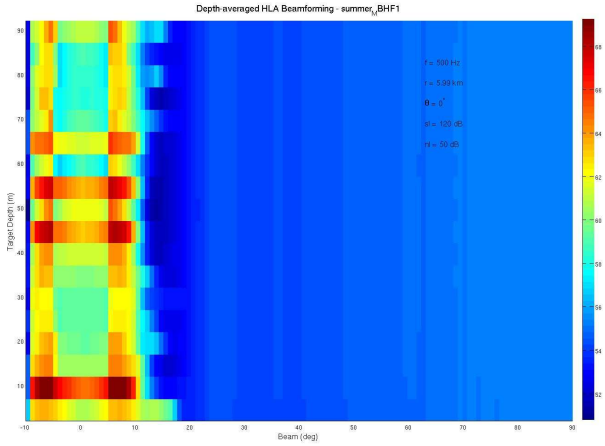

(c) Averaged receiver depth beamformer output

Figure 3.51: SI algorithm output for 500Hz source, 20 layers averaging, range 5.99km

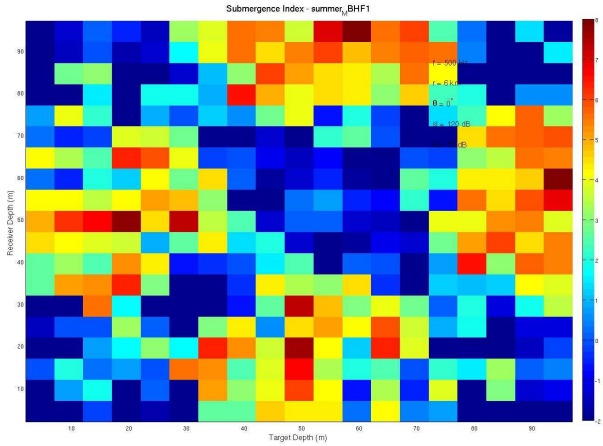

(a) SI for all depth/ receiver depth combinations

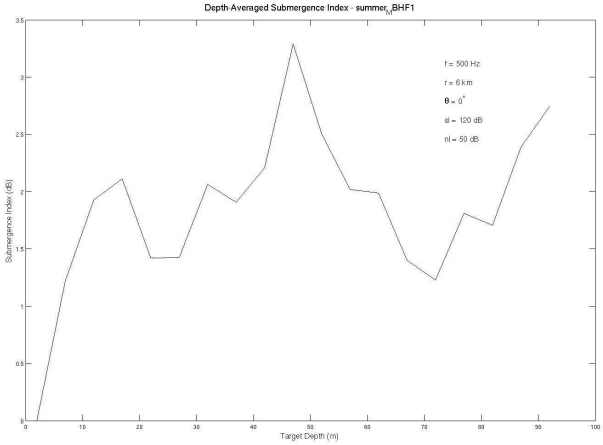

(b) Averaged receiver depth SI

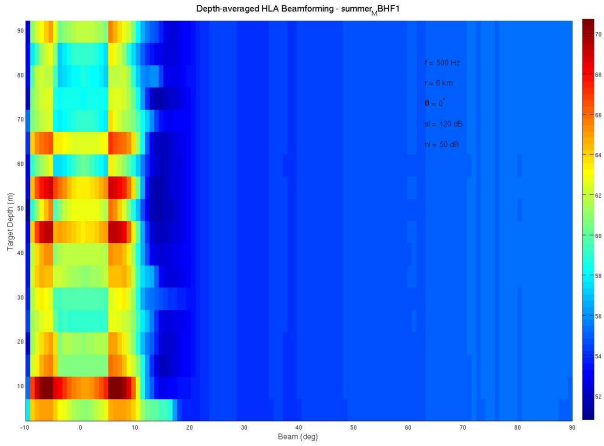

(c) Averaged receiver depth beamformer output

Figure 3.52: SI algorithm output for 500Hz source, 20 layers averaging, range 6.0km

depth sampling points had been suggested as a solution to a range instability with the price of a significant increase in calculation time. A number of propagation model iterations during an SI calculation is n^2, where n is the number of stratified layers, so in our case a multiplication of the number of layers by 2 requires additional 300 iterations. The price is relatively high, so we will try to solve the problem by adding an averaging process through range to the algorithm.

An initial range had been defined for a receiver in surface location (first depth level). For each next receiver depth level a range to the target had been decreased by a factor of $\Delta r = \frac{\Delta d}{\tan \alpha} + comp$, where $\Delta d, \alpha, comp$ are: changes in the depth, a diving angle, and a constant compensation factor respectively. The compensation factor is added as a consideration of a 'tail' (towed array) length. It had been set to 50m.

The depth averaged SI results of a 6km initial range for a 500Hz target were most interesting. Depth-range averaged SI results for the same initial parameters are shown in Fig. 3.53 for 45^0diving angle case. An initial range to the the target was 6km and a final range for 82m depth was 5.451km. Let's compare results in Fig. 3.53 to results of a depth averaging in Fig. 3.36. It's arises immediately that the depth-range averaging improved SI results with no need for any additional calculations.Therefore it is reasonable to assume that a range sensitivity problem of the algorithm can be solved by range averaging without trade-off, on the contrary there is a benefit - the process makes simulation condition more realistic. We will explore this subject more by investigating some other scenarios as a preliminary step to final conclusions.

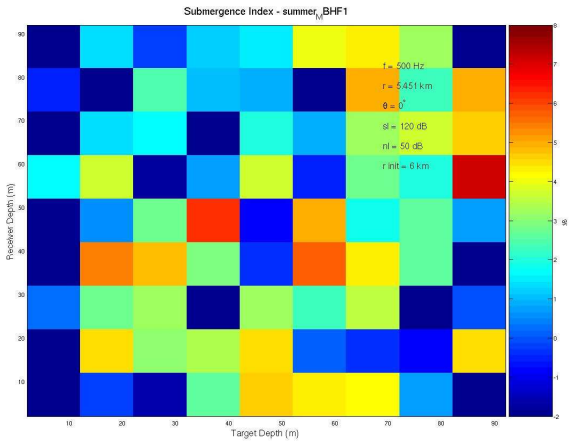

(a) SI for all depth/ receiver depth combinations

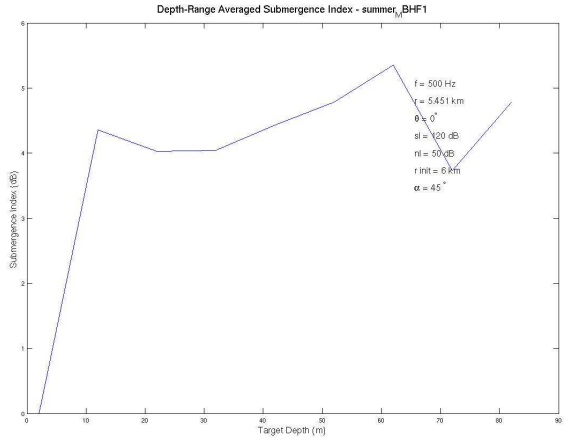

(b) Averaged receiver range-depth SI

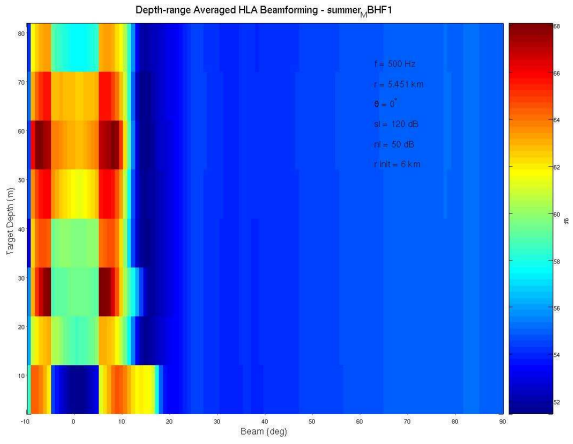

(c) Averaged receiver range-depth beamformer output

Figure 3.53: SI algorithm output for 500Hz source, depth-range averaging, range $6km, \alpha = 45^0$

In Fig. 3.54 and 3.55 a range of 6km with $\alpha = 60^0$ and $\alpha = 75^0$cases are shown.

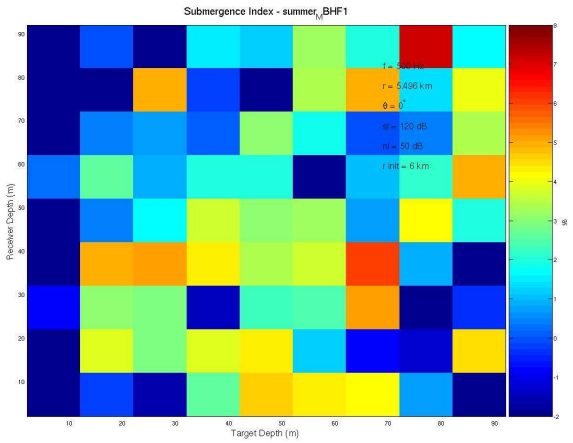

(a) SI for all depth/ receiver depth combinations

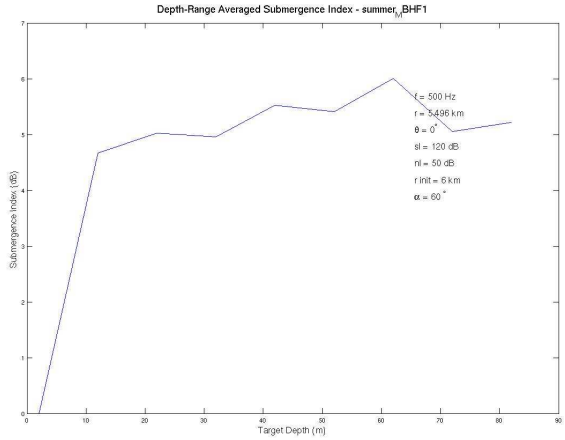

(b) Averaged receiver range-depth SI

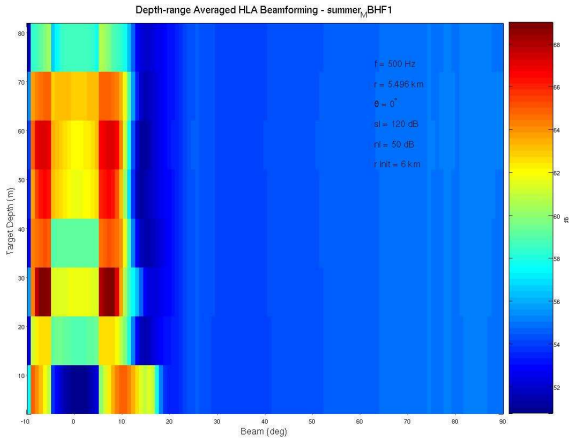

(c) Averaged receiver range-depth beamformer output

Figure 3.54: SI algorithm output for 500Hz source, depth-range averaging, range $6km, \alpha = 60^0$

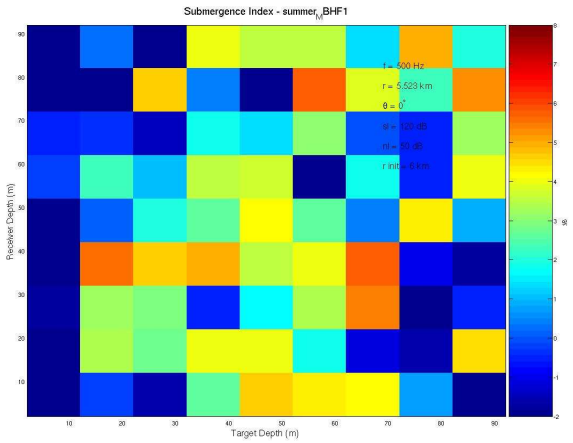

(a) SI for all depth/ receiver depth combinations

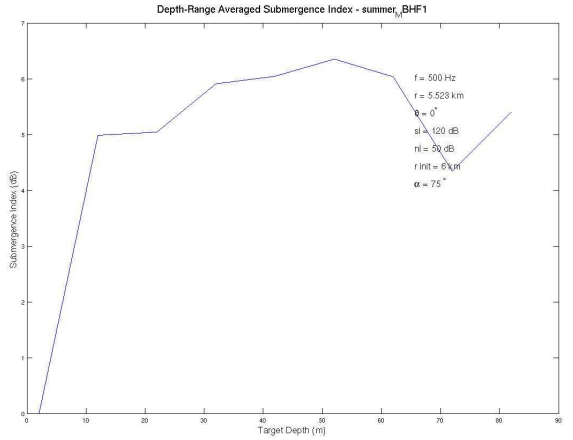

(b) Averaged receiver range-depth SI

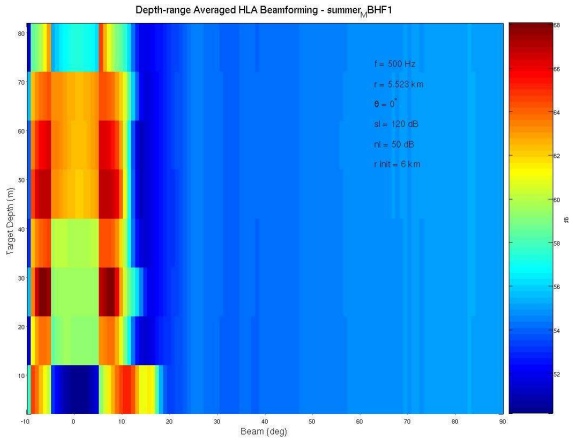

(c) Averaged receiver range-depth beamformer output

Figure 3.55: SI algorithm output for 500Hz source, depth-range averaging, range $6km, \alpha = 75^0$

The SI results are very satisfying in both $\alpha = 60^0$ and $\alpha = 75^0$ cases. An SI for a surface target can be easily distinguished among other cases and differences between represented diving angles are insignificant. The last can be explained by relatively small differences in a total averaging range area. The final range to the target is changing from 5.451km to 5.496km and to 5.523km for all three cases respectively. A 'tail' compensation factor part in range changes is more significant, therefore an influence of diving angle changes is less significant for final results. Nevertheless a diving angle can be very useful as a parameter of AUV behavior to submit the optimal SI results when the 'tail' length stays fixed and it is a function of an array angle resolution3.1.

We used 45^0as a diving angle for some other ranges (ranges of previously described cases of a depth averaging were used). The results can be found in Fig. 3.56, 3.57, 3.58 for 8.3km, 9km, 12km ranges respectively.

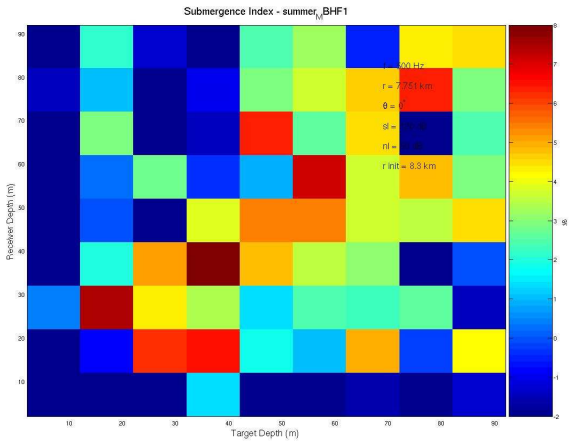

(a) SI for all depth/ receiver depth combinations

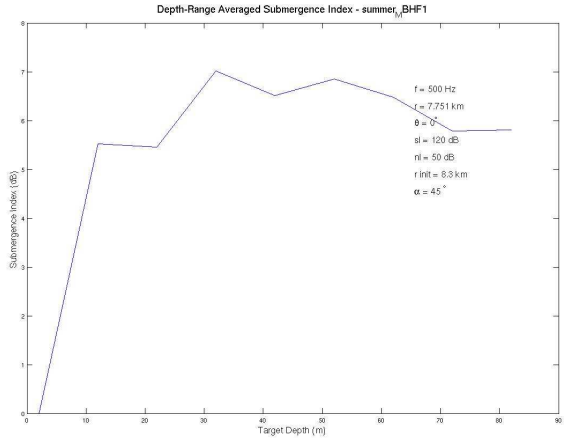

(b) Averaged receiver range-depth SI

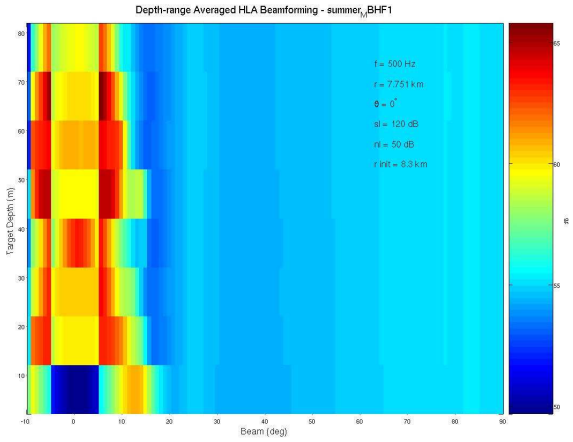

(c) Averaged receiver range-depth beamformer output

Figure 3.56: SI algorithm output for 500Hz source, depth-range averaging, range $8.3km, \alpha = 45^0$

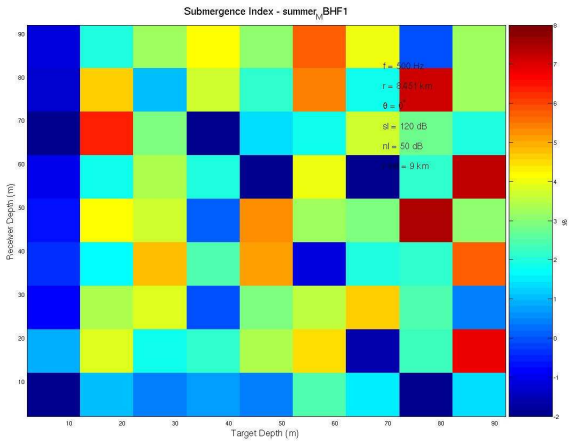

(a) SI for all depth/ receiver depth combinations

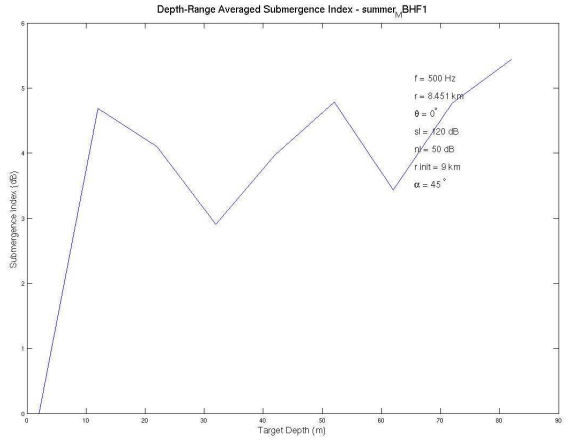

(b) Averaged receiver range-depth SI

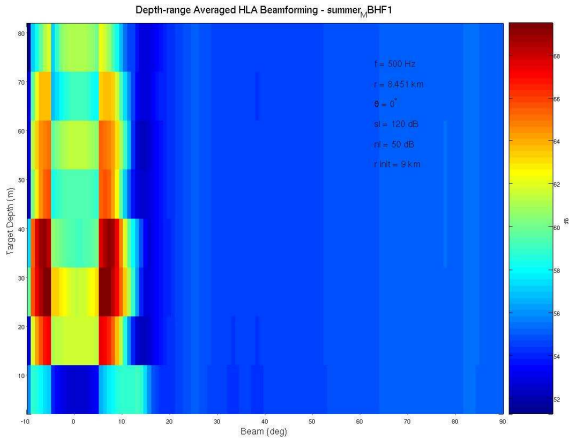

(c) Averaged receiver range-depth beamformer output

Figure 3.57: SI algorithm output for 500Hz source, depth-range averaging, range $9.0km, \alpha = 45^0$

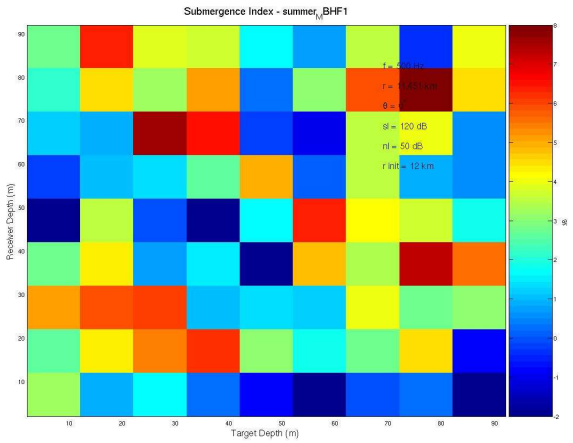

(a) SI for all depth/ receiver depth combinations

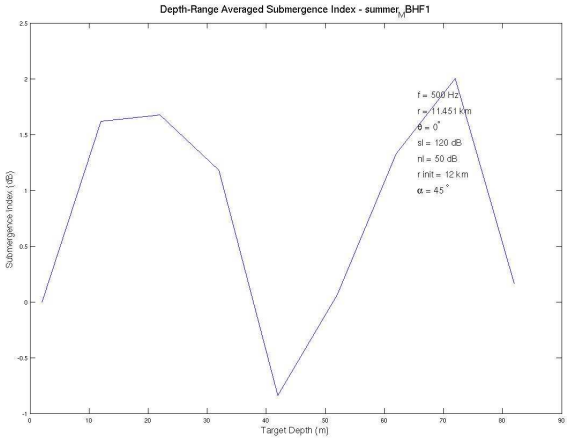

(b) Averaged receiver range-depth SI

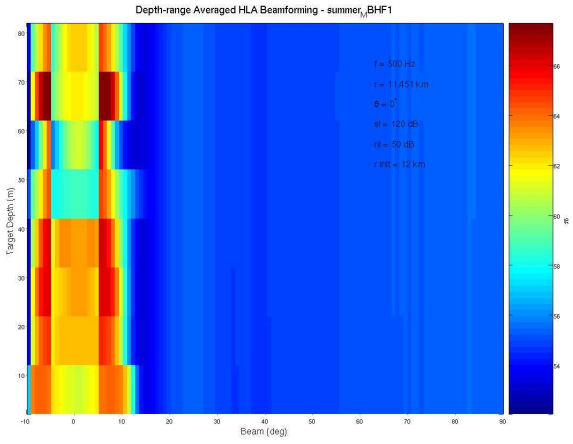

(c) Averaged receiver range-depth beamformer output

Figure 3.58: SI algorithm output for 500Hz source, depth-range averaging, range $12km, \alpha = 45^0$

The most interesting result is the last one (12km range) (Fig.3.58). As we can see a 42m deep target looks the same as a surface target. The SI results are misleading as was in a depth averaging case for 6 km range. We tried this time to solve the issue by a different approach. Instead of adding depth sampling points we decided to increase a total area of range averaging. This can accomplished by diving angle decreasing, a trade-off is a AUV maneuvering time and therefore a total SI calculation time. A diving angle was set to $\alpha = 15^0$, meaning that averaging area was extended by $\sim 250m$. Results are shown in Fig.3.59 and an improvement can be noticed.

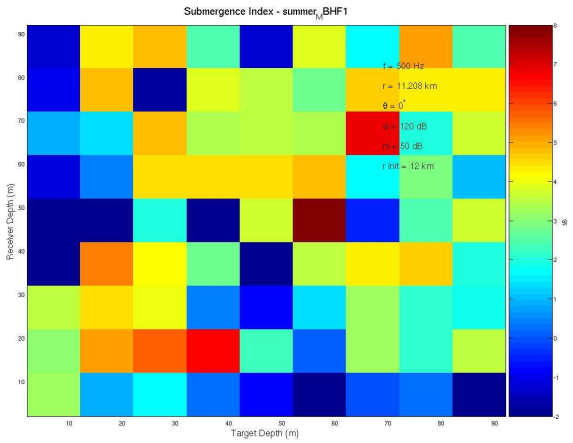

(a) SI for all depth/ receiver depth combinations

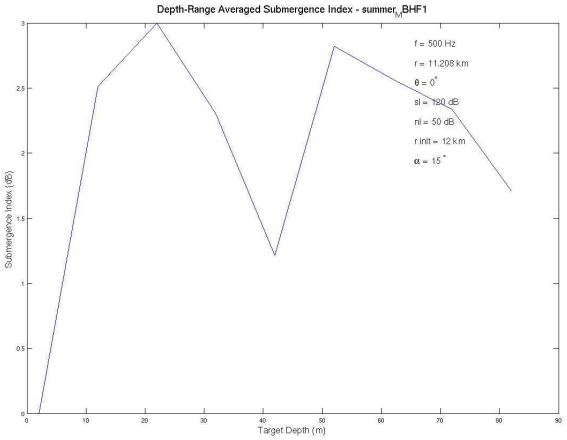

(b) Averaged receiver range-depth SI

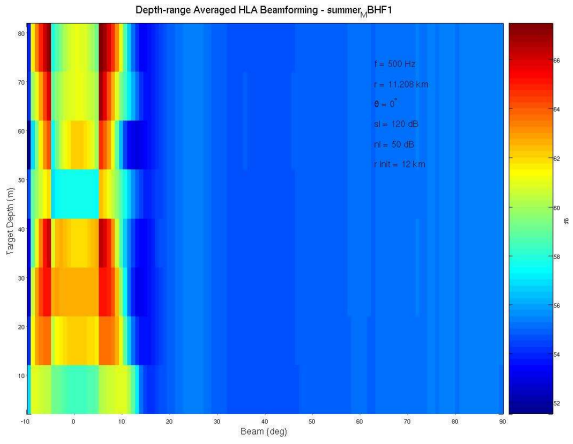

(c) Averaged receiver range-depth beamformer output

Figure 3.59: SI algorithm output for 500Hz source, depth-range averaging, range $12km, \alpha = 15^0$

In the next step, the range-depth averaging approach had been applied to 1kHz source. Different range to the target cases had been tested. Results are shown in Fig. 3.60, 3.61, 3.62 for 5km, 7.4km and 12.3km respectively. For a 12.3km range the SI results are misleading as was in case of a 12km range and a 500Hz source.

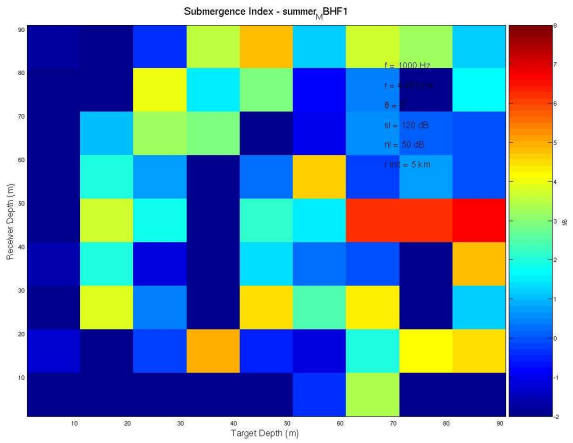

(a) SI for all depth/ receiver depth combinations

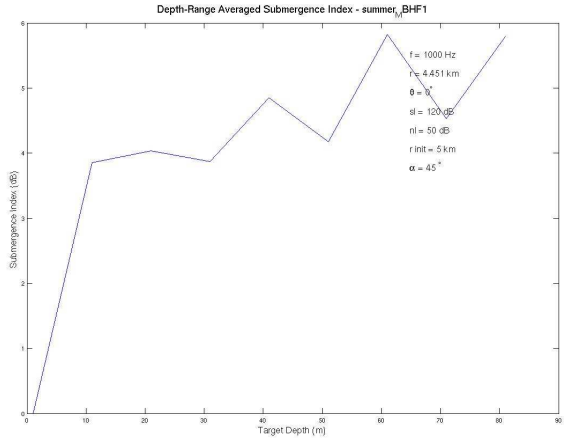

(b) Averaged receiver range-depth SI

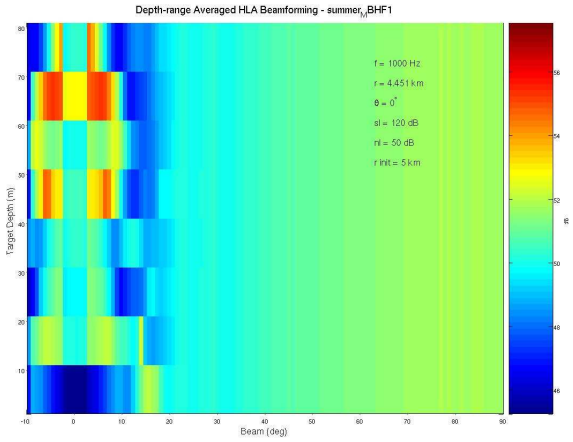

(c) Averaged receiver range-depth beamformer output

Figure 3.60: SI algorithm output for 1kHz source, depth-range averaging, range $5km, \alpha = 45^0$

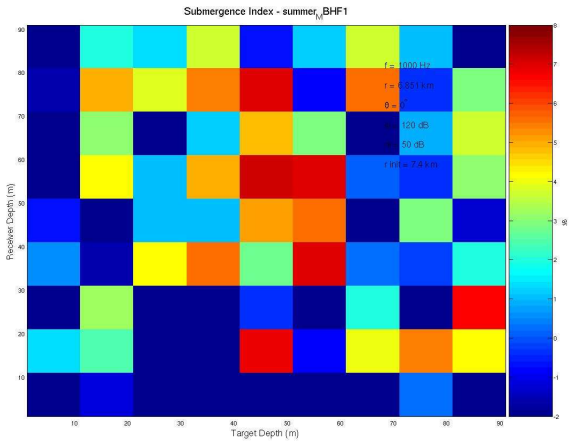

(a) SI for all depth/ receiver depth combinations

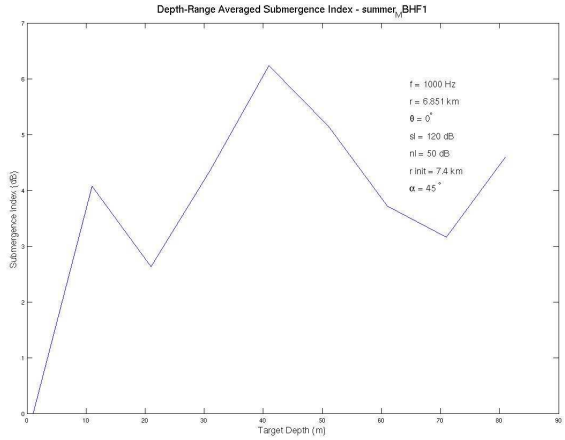

(b) Averaged receiver range-depth SI

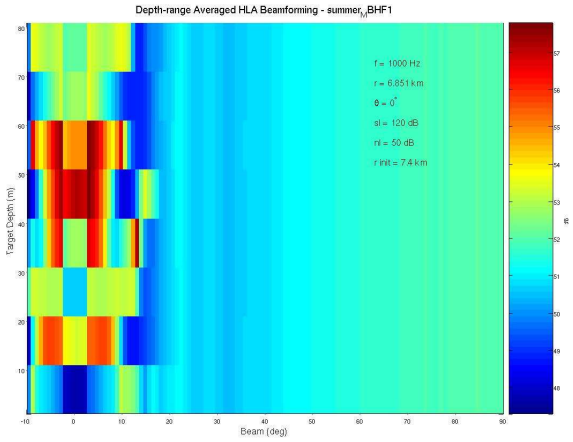

(c) Averaged receiver range-depth beamformer output

Figure 3.61: SI algorithm output for 1kHz source, depth-range averaging, range $7.4km, \alpha = 45^0$

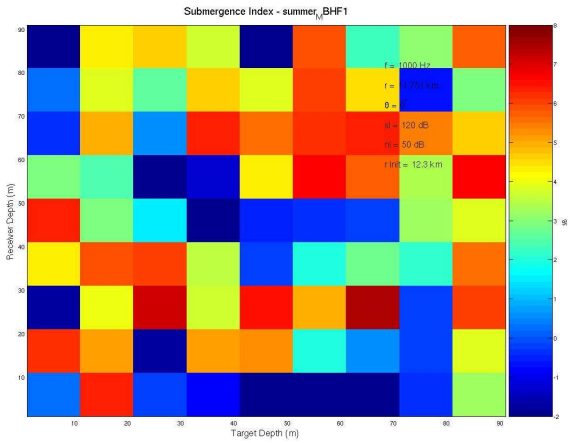

(a) SI for all depth/ receiver depth combinations

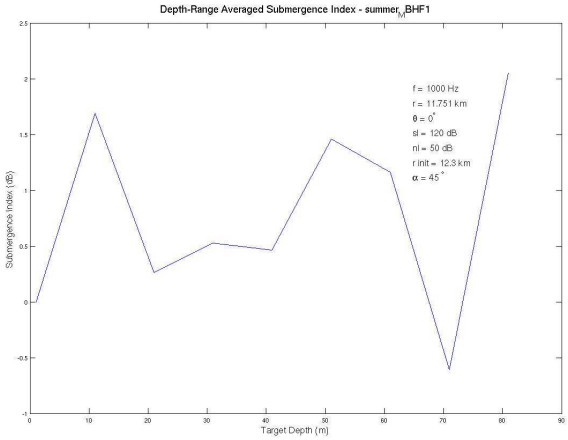

(b) Averaged receiver range-depth SI

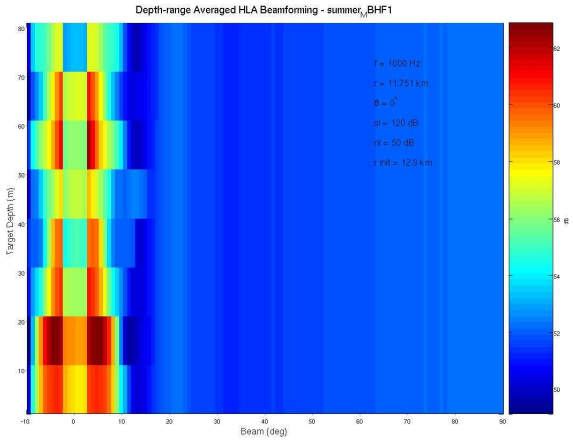

(c) Averaged receiver range-depth beamformer output

Figure 3.62: SI algorithm output for 1kHz source, depth-range averaging, range $12.3km, \alpha = 45^0$

We will adopt here the same approach as before of an averaging area increasing. Decreasing of diving angle to 15^0will give us satisfying results shown in Fig. 3.63. Therefore a diving angle of 15^0 looks as optimal angle from SI optimization point of view.

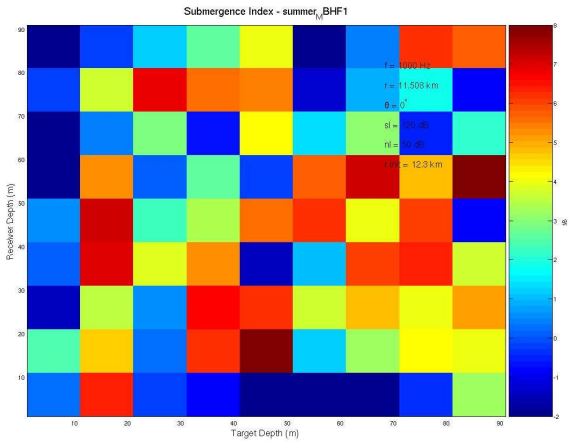

(a) SI for all depth/ receiver depth combinations

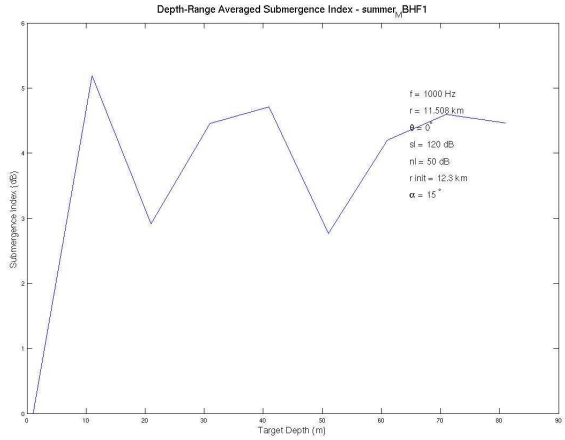

(b) Averaged receiver range-depth SI

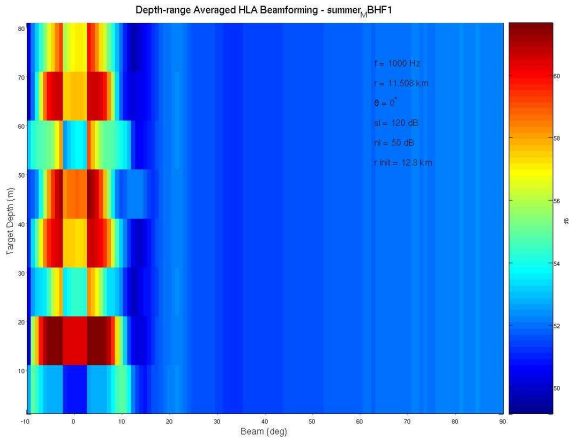

(c) Averaged receiver range-depth beamformer output

Figure 3.63: SI algorithm output for 1kHz source, depth-range averaging, range $12.3km, \alpha = 15^0$

The range averaging addition to the SI algorithm had been checked on some other scenarios and for all the cases the SI separation capabilities between surface and submerged sources were stable.

3.2.9 SI behavior in range-independent environment - summary.

We can generalize based on the results presented in 3.2 that SI algorithm is robust enough to distinguish between surface and submerged targets. The algorithm is indifferent to a windowing technique process. The algorithm can provide accurate results for a source frequency range between 100Hz and 1kHz in environmental conditions of Monterrey Bay and for bearing angles up to $\sim 20^0$. Although the algorithm relies generally on averaging through 10 stratifying layers for most of the ranges, to get more accurate results 20 layers stratification and averaging is recommended.

Range-depth averaging approach has some advantages over regular depth averaging approach. The range-depth averaging allows more accurate simulation of a depth changing process in most cases (except the static diving case, which is irrelevant in the current discussion) and improves substantially SI algorithm stability for various target-receiver range separation cases. From the studied cases arises that a diving angle of 15^0will be optimal to maintain SI capabilities.

Chapter 4

SI Calculation for Range-Dependent Case

In this chapter SI results for a range-dependent environment will be presented. Range-dependent environment will be simulated by an upslope/ downslope bottom. Simulation results will be discussed and applicable conclusions will be made to ensure an SI algorithm stability for coastal areas with range-dependent characteristics. A brief theoretical explanation of a wave propagation mechanism in a wedge-shaped ocean will be also provided.

4.1 Essence of upslope/ downslope sound propagation.

Our current discussion can't be complete without a study of a SI behavior in a range-dependent environment. Our particular interest is to investigate an impact of a wedge-shaped coastal area on an SI capability to recognize surface and submerged targets. It will be useful, for our further discussion about SI simulation results, to summarize main effects of a shallow water sound propagation in presence of the downslope/ upslope geometry.

The subject has been studied extensively, and a wide selection of publications covering the area can be found[8, 9, 22, 23, 24, 25, 26]. Special attention of authors usually has been given to modeling issues, and relatively simple cases of few modes has been discussed to provide a good understanding of a modal energy conversion (mode coupling) mechanism. We will try to re-catch the most essential ideas of the sound propagation in the wedge-shaped environment for further analysis of SI simulation results.

Our recent discussion 3 about SI simulation results for a range-independent environment was based on the dependence of a pressure field modal distribution on the source location (see 3.1). We can rely on the same effect for the current environment. For either downslope or upslope cases the modal distribution of the energy at the source location will be a depth dependent, yet the SI results at the receiver location are expected to be different as long as the receiver is distant from the source.

An intuitive explanation for this is obvious. The SI algorithm is based on calculations of a ratio between energy concentrated in shallow and steep propagating angles. In range-independent environment the modal angle doesn't change it's value due to bottom interaction so the modal angle ratio generally keeps it's value through the range. It easier to think about it using ray theory concepts. For a range-independent case each mode can be represented by a particular family of rays with equal grazing angles. In the presence of the bottom slope the situation is completely different. By simple geometry consideration it can be easily seen that every interaction with a slope will reduce a ray propagation angle for a downslope case and increase the angle for an upslope case. Therefore we can't be sure anymore that the angle ratio (SI) will be a true indicator of the source location. We can simplify a downslope/ upslope effect's explanation from SI point of view by thinking that the energy is shifting to the shallow/ steep angles subspace directions respectively as the sound propagates to the receiver.

Although the subject of a mode coupling is obviously more complicated than the current presentation and it is incomplete without a modal analysis and coupling criterias' examination (could be found in [9, 8, 23]),

it will be satisfying for a purpose of our study to understand that the previously presented results cannot be sustained in a wedge-shaped ocean. It is hard to make some definite conclusions based on the analytical analysis about how constructive or destructive a slope presence can be for SI capabilities, mainly because of a relatively high number of modes that will be excited at the frequencies of a interest (500Hz and 1kHz). Yet we can assume that for a surface target with relatively low energy concentration in a shallow angles subspace, which is a main property for recognizing it among other targets, the downslope will have destructive influence. The upslope on other hand can be constructive element for SI capabilities. These assumptions are preliminary and based on intuition only, therefore we need to test their correctness through SI simulations.

4.2 SI simulations range-dependent environments

For a range-dependent case we had to change a propagation model from a previously used OASES to a RAM (Parabolic equation) algorithm. Therefore an SI calculation procedure had been changed slightly too. The AcTUP (Acoustic Toolbox)[27] was used as an interface to the RAM algorithm. By using AcTUP we were able to calculate propagating pressure field in the watercolumn with resolution of 0.75m in range and 10m in depth. Instead of recalling an OASES algorithm for each particular geometry combination for source and receiver locations as it was for a range-independent case, we implemented a routine which multiplies a steering vector with pressure field values pre-calculated by RAM. Beside these changes the main structure for the SI calculations remained the same.

Frequencies of 500Hz and 1kHz have been studied for a range-dependent environment for ranges up to 10 km. Both downslope and upslope cases have been simulated for shallow slope angles up to 2 degrees. The slope has been defined by changing a watercolumn depth in every 1250 m segment of the range so the total number of eight areas with different watercolumns had been 'stitched' together. Exact soundspeed profiles for each of simulation cases and the simulation results will be presented in next sections. Bottom parameters remained the same as for a range-independent case, though a bottom attenuation influence has been studied too for a downslope environment, and for this purpose the bottom attenuation value was increased.

Although the SI algorithm was based on the depth averaging exclusively, small fluctuations in range values have been assumed due to limits to reallocate AUV to some fixed point in the watercolumn as a part of a maneuver between pre-defined sampling depth levels. Therefore area of 17m was defined to simulate these fluctuations. The depth averaging process had been based on a sampling process of a pressure field between 1m and 90m depth without consideration of a watercolumn's total depth at array location. For practical reasons it is highly time-consuming process to sample pressure at depth levels that are uniformly distributed through the watercolumn, specially if the watercolumn has been rapidly increased.

4.3 SI results for a downslope environment

The first case of range-dependent part of our study was for a 0.5 degree downslope bottom environment. The slope is extremely mild and could be found in various reference articles as a weak coupling case. We set an initial watercolumn's depth to 100m (same as for a range-independent case) at a source location and a final watercolumn at a range of 8750m was set to 187.5m. The soundspeed profile is shown in Fig. 4.1. A bottom soundspeed was set to $c_b = 1612\frac{m}{s}$ with attenuation of $\alpha = 0.4\frac{dB}{\lambda}$.

The SI results were tested for source frequencies of 500Hz and 1kHz. Pressure field excited by a surface 500 Hz source was calculated by the RAM and the results are shown in Fig. 4.2

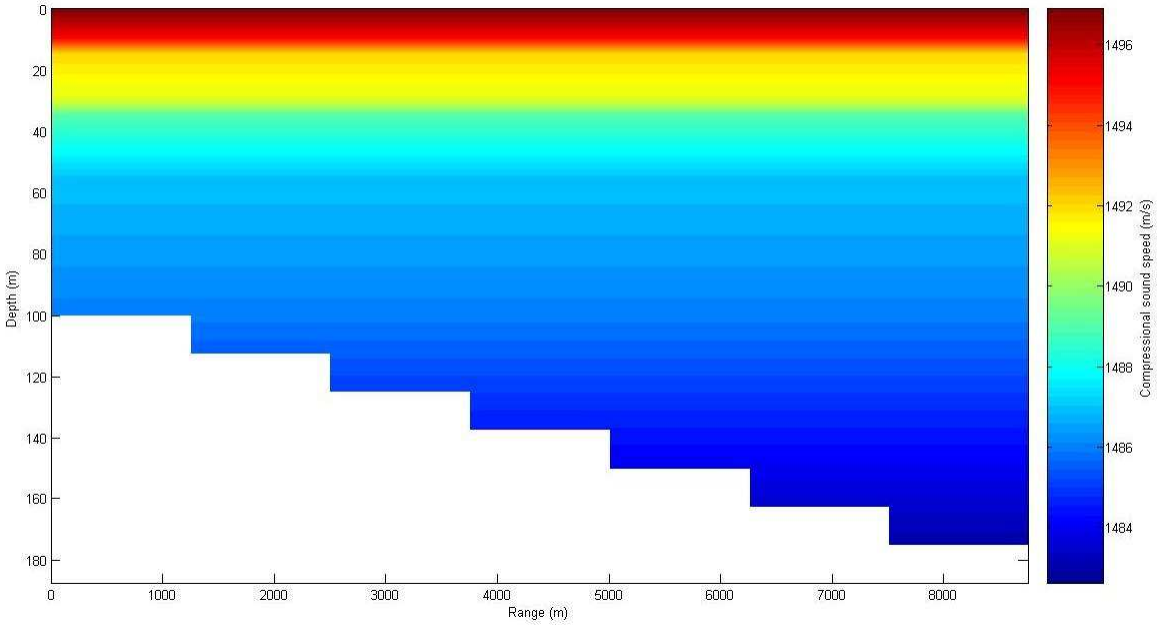

Figure 4.1: Downslope half degree watercolumn soundspeed profile

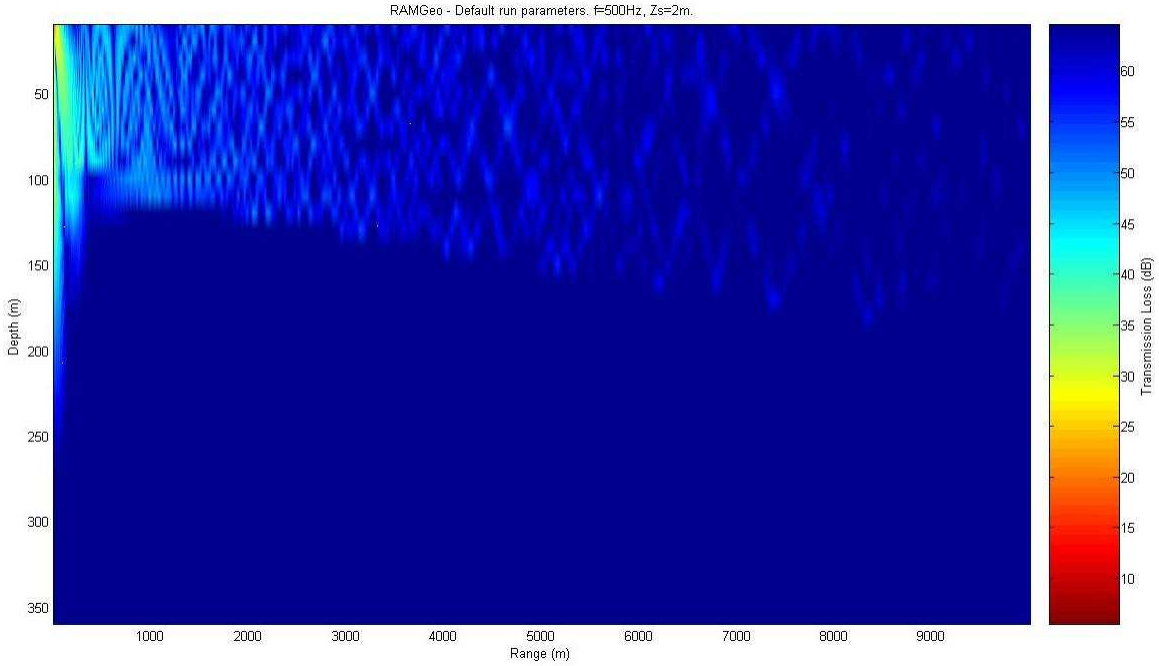

Figure 4.2: Total pressure field, downslope 0.5^0, 2m depth target, 500Hz

The SI simulation results (pre-averaged and final) for a frequency of $f_0 = 500Hz$ are presented in Fig.4.3-4.7 for a range separation from 1km to 5km.

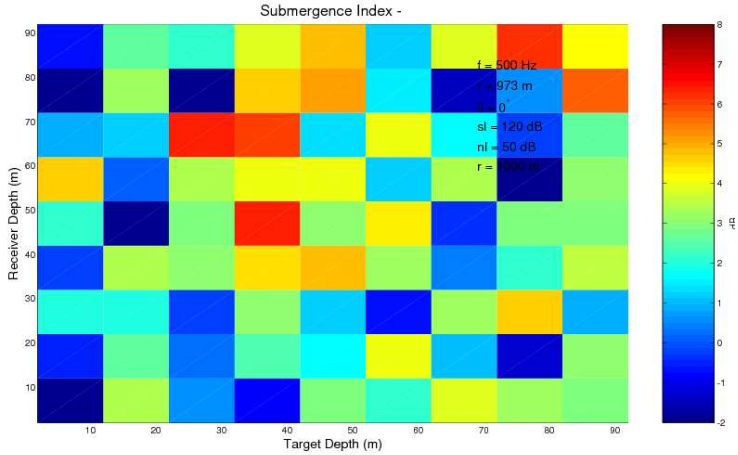

(a) SI for all depth/ receiver depth combinations

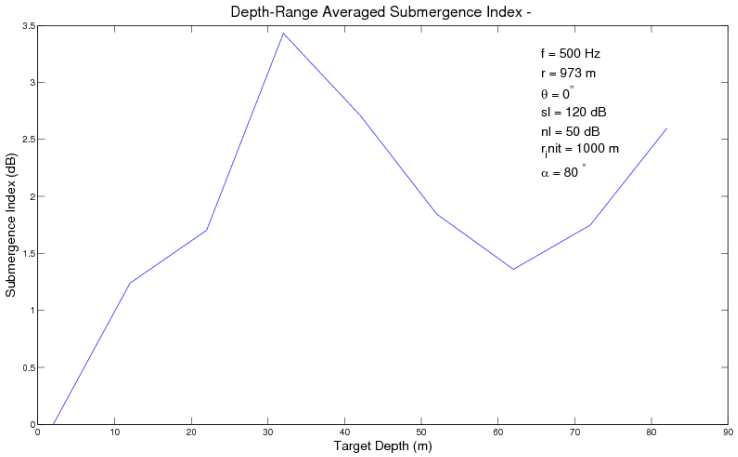

(b) Averaged SI results

Figure 4.3: SI ,500Hz source, downslope 0.5^0, range $1km$

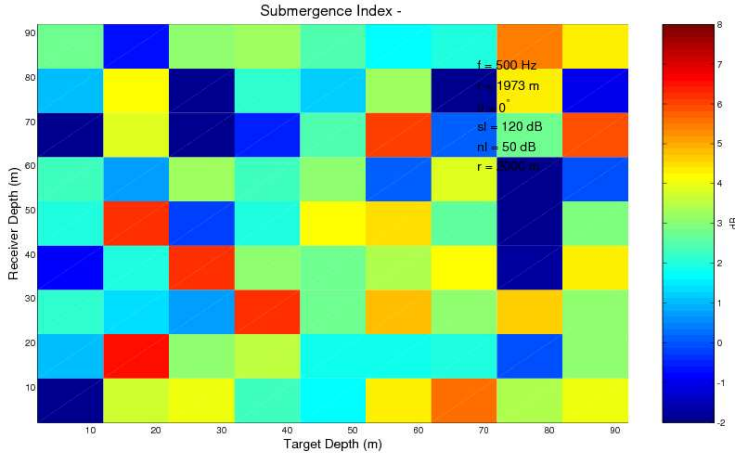

(a) SI for all depth/ receiver depth combinations

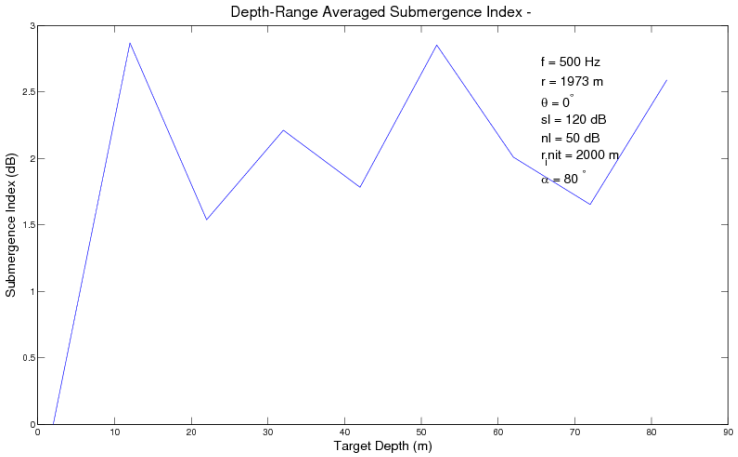

(b) Averaged SI results

Figure 4.4: SI ,500Hz source, downslope 0.5^0, range $2km$

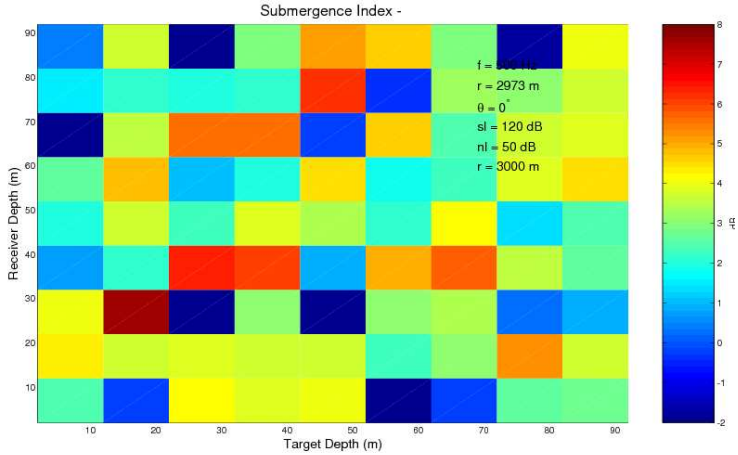

(a) SI for all depth/ receiver depth combinations

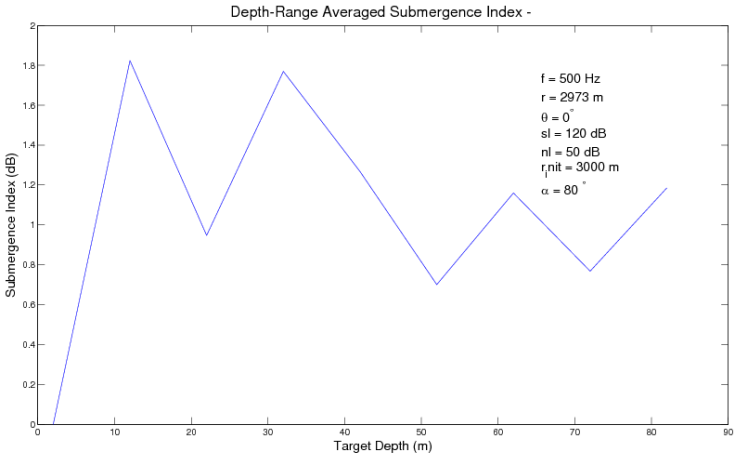

(b) Averaged SI results

Figure 4.5: SI ,500Hz source, downslope 0.5^0, range $3km$

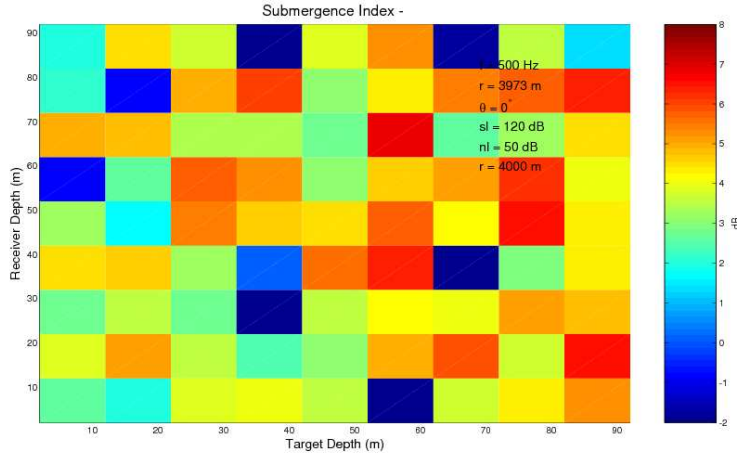

(a) SI for all depth/ receiver depth combinations

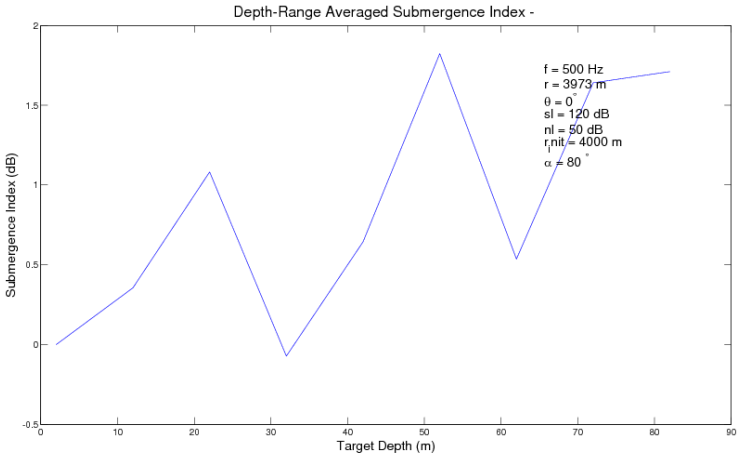

(b) Averaged SI results

Figure 4.6: SI ,500Hz source, downslope 0.5^0, range $4km$

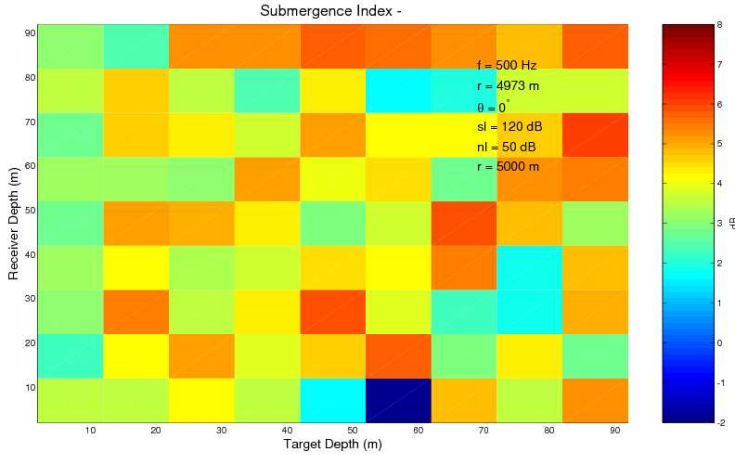

(a) SI for all depth/ receiver depth combinations

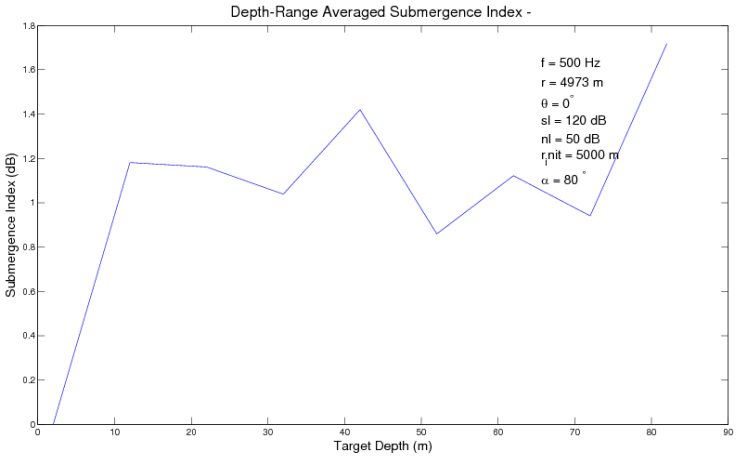

(b) Averaged SI results

Figure 4.7: SI ,500Hz source, downslope 0.5^0, range $5km$

From the results we can conclude that SI behavior can be expected to be very unstable if a receiver is moving farther away from a source and a slope interaction effect is getting more significant. Although the simulation results are supporting our previously made assumptions about a destructive impact of a downslope presence on SI capabilities, it is surprising that even for a mild slope of a half degree this destructive pattern can be immediately seen.

We will test the SI results in the same environment but for 1kHz source. The pressure field for a surface 1kHz target case is shown in Fig.4.8 and SI results are in Fig.4.9-4.13 for the same ranges as in the 500Hz case.

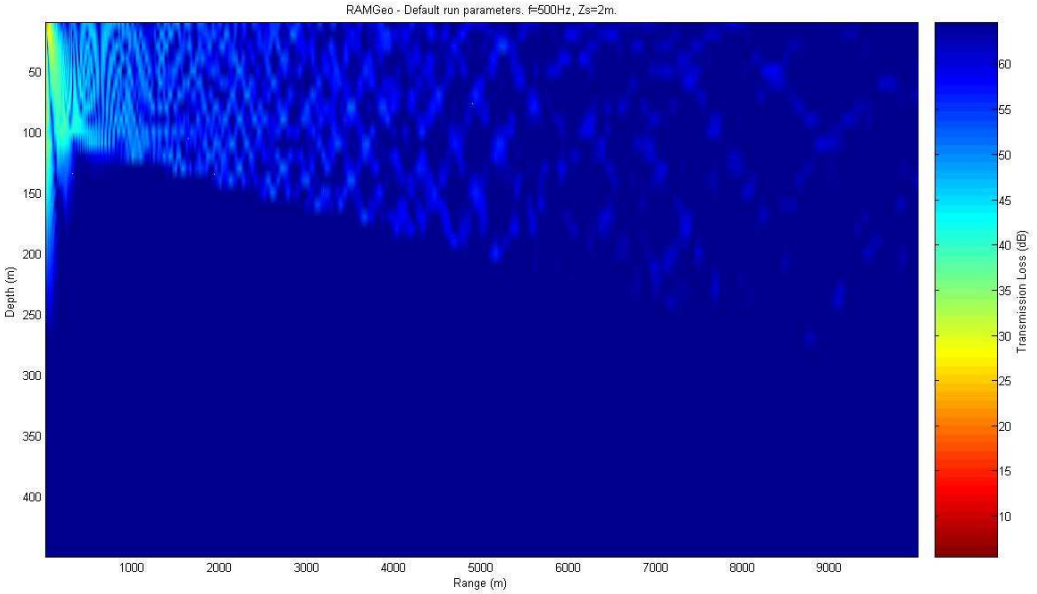

Figure 4.8: Total pressure field, downslope 0.5^0, 1m depth target, 1kHz

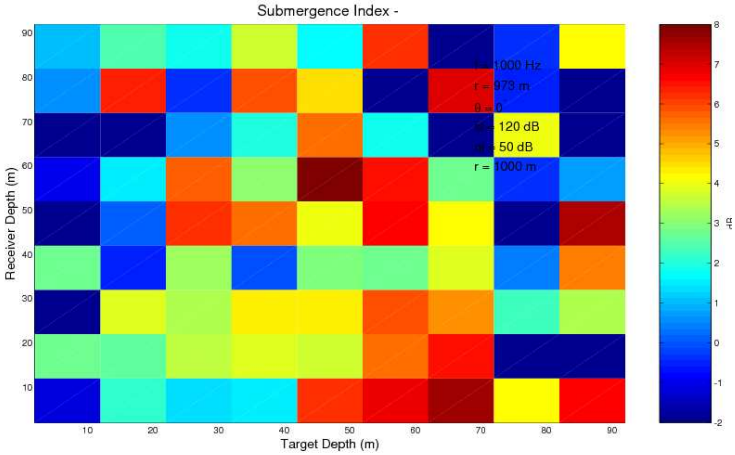

(a) SI for all depth/ receiver depth combinations

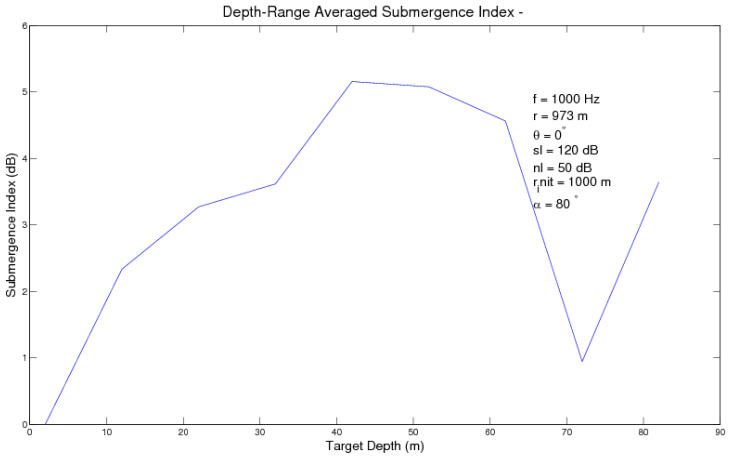

(b) Averaged SI results

Figure 4.9: SI ,1kHz source, downslope 0.5^0, range $1km$

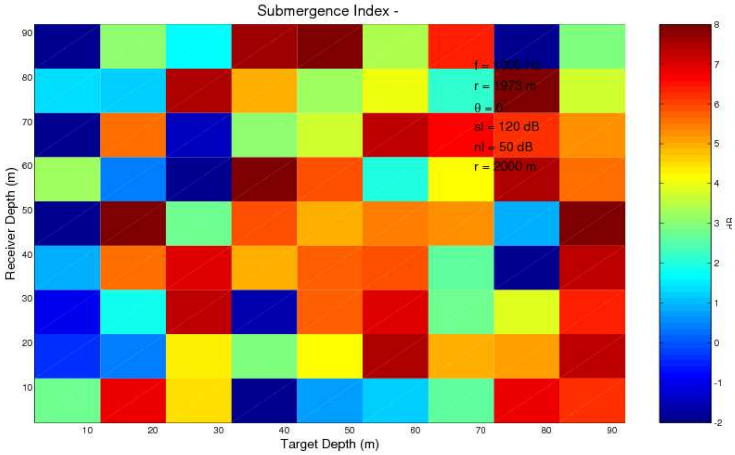

(a) SI for all depth/ receiver depth combinations

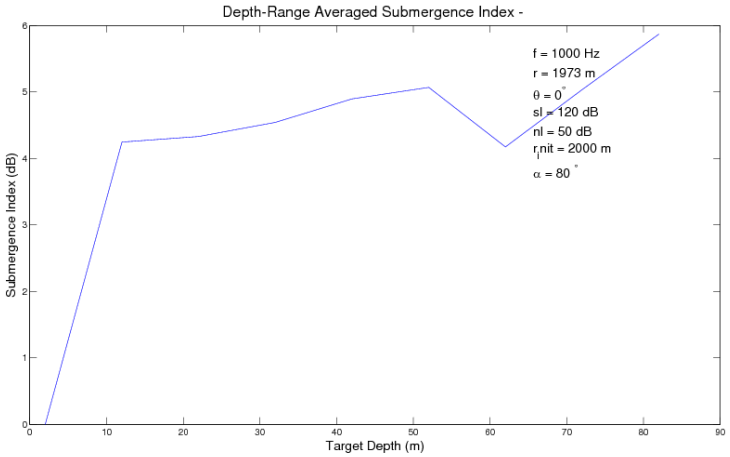

(b) Averaged SI results

Figure 4.10: SI ,1kHz source, downslope 0.5^0, range $2km$

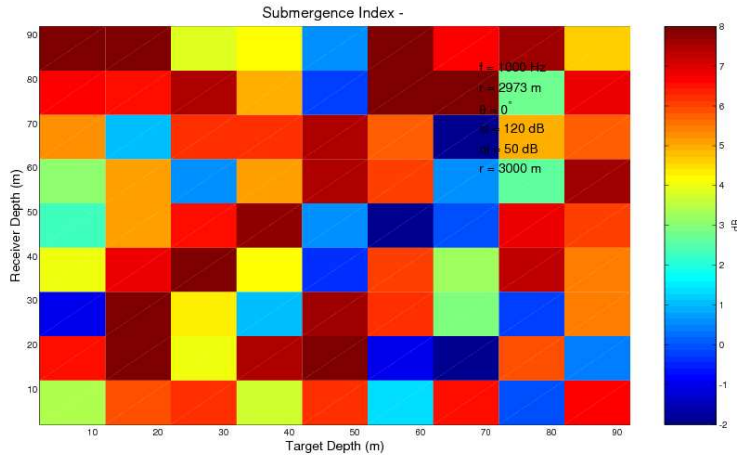

(a) SI for all depth/ receiver depth combinations

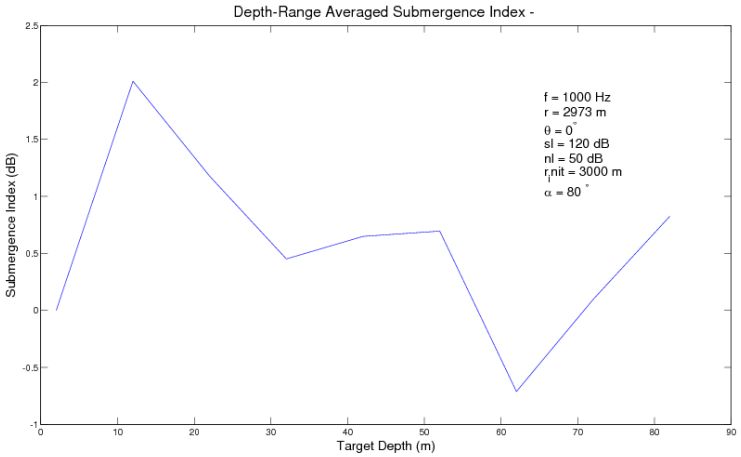

(b) Averaged SI results

Figure 4.11: SI ,1kHz source, downslope 0.5^0, range $3km$

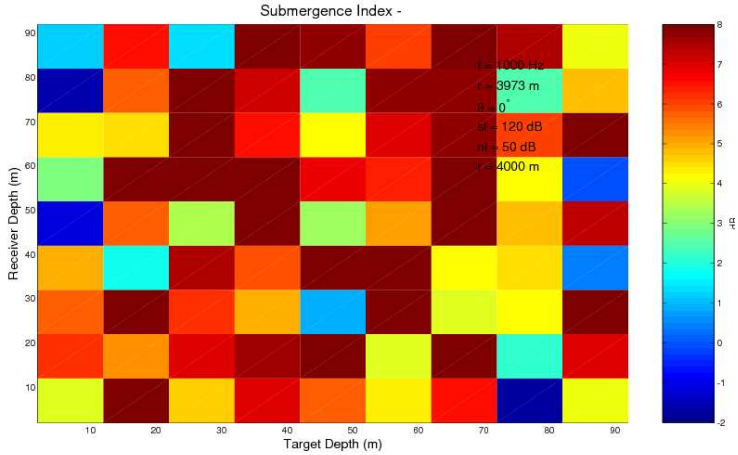

(a) SI for all depth/ receiver depth combinations

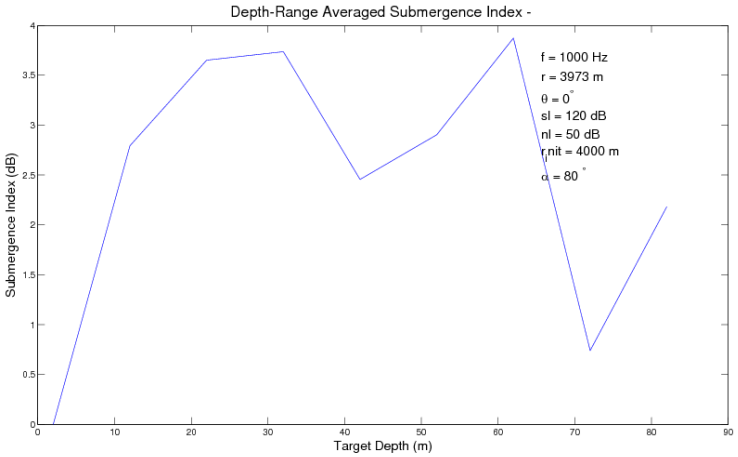

(b) Averaged SI results

Figure 4.12: SI ,1kHz source, downslope 0.5^0, range $4km$

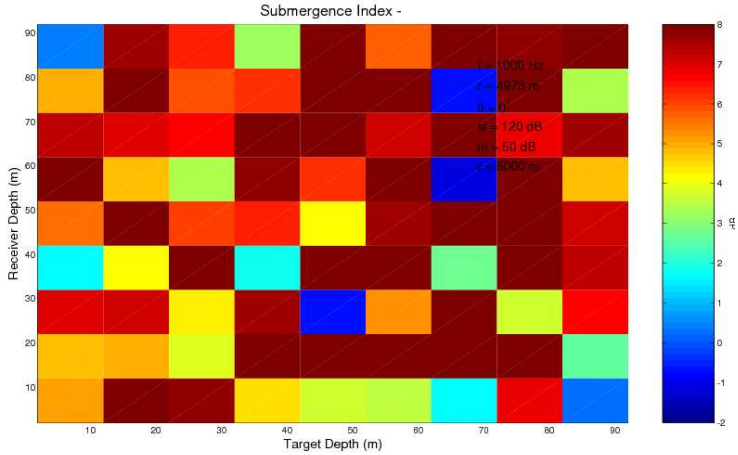

(a) SI for all depth/ receiver depth combinations

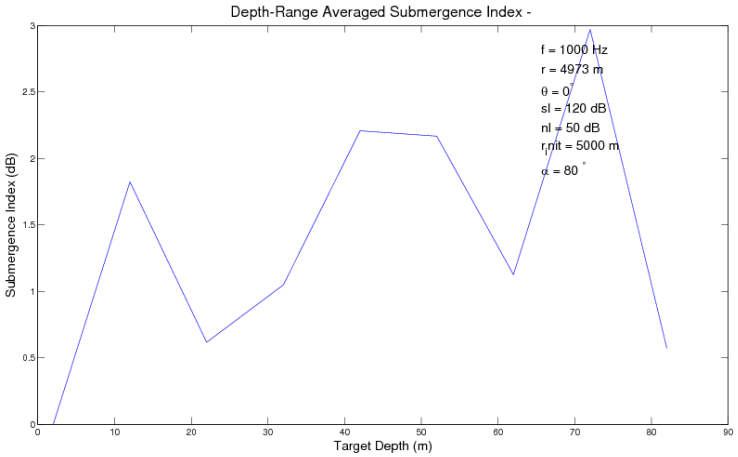

(b) Averaged SI results

Figure 4.13: SI ,1kHz source, downslope 0.5^0, range $5km$

From the results it appears that the SI capabilities to recognize a 1kHz surface target are degrading relatively to 500Hz source in the same environment. Therefore it can be summarized that a downslope presence will reduce SI capabilities for 500Hz and 1kHz sources even to the level of a complete incapability for some ranges. We will check if our preliminary conclusions are correct by examining 1 degree downslope simulation results. We should expect at this point that a downslope angle growing will cause additional degrading of SI capabilities.

The soundspeed profile described by Fig.4.14 was defined according to the same protocol as for the half degree. The final watercolumn depth at range of 8.5km from the target was set to 275m.

Pressure field and SI results for a 500Hz source are shown in Fig.4.15-4.20. It can be noticed from the results that the destructive impact of the downslope angle on the SI capabilities became stronger as a slope angle grew.

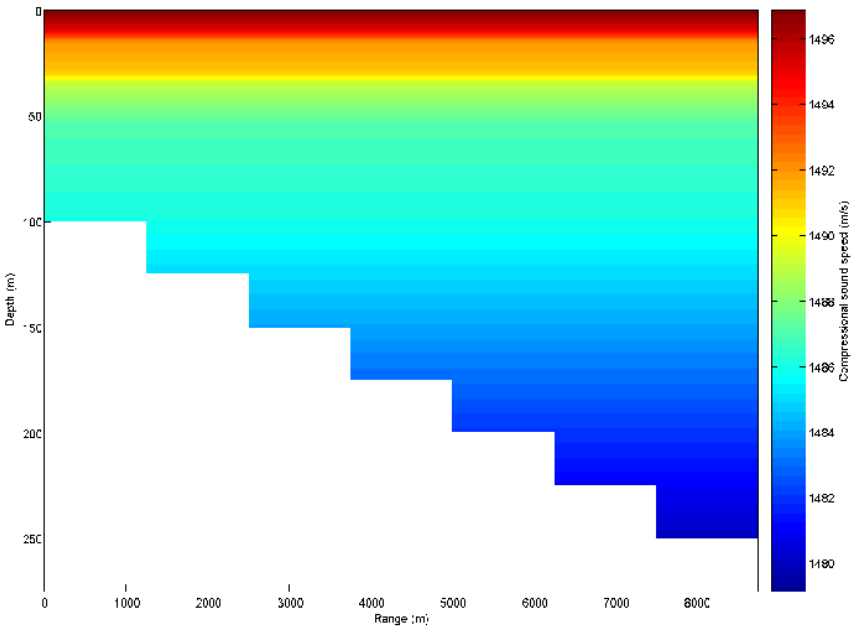

Figure 4.14: Downslope 1 degree watercolumn soundspeed profile

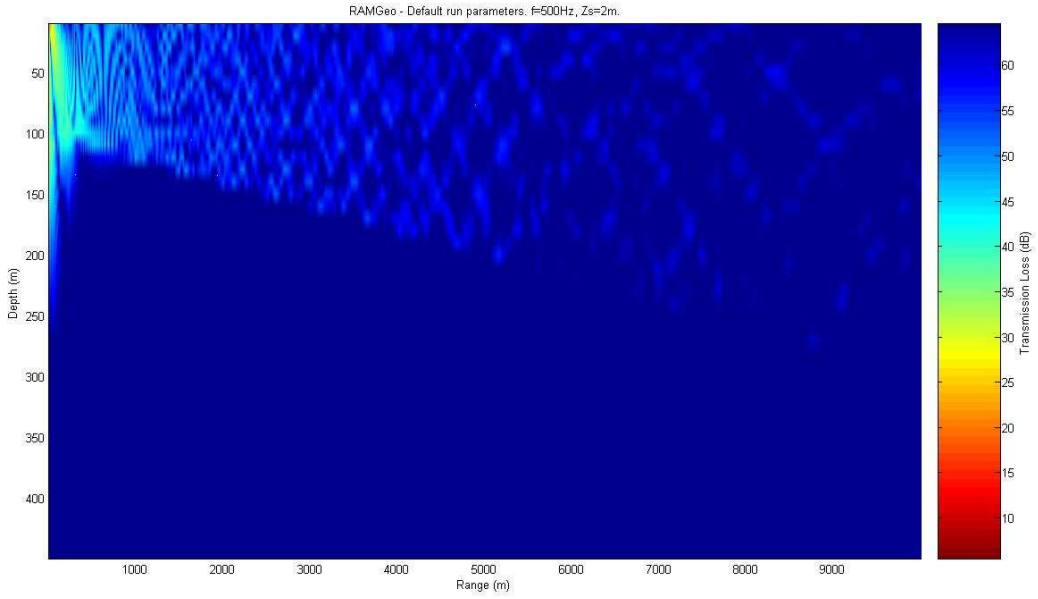

Figure 4.15: Total pressure field, downslope 1^0, 2m depth target, 500Hz

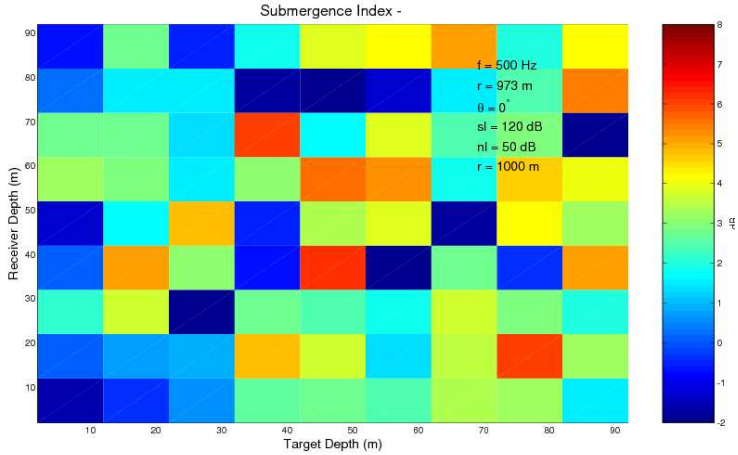

(a) SI for all depth/ receiver depth combinations

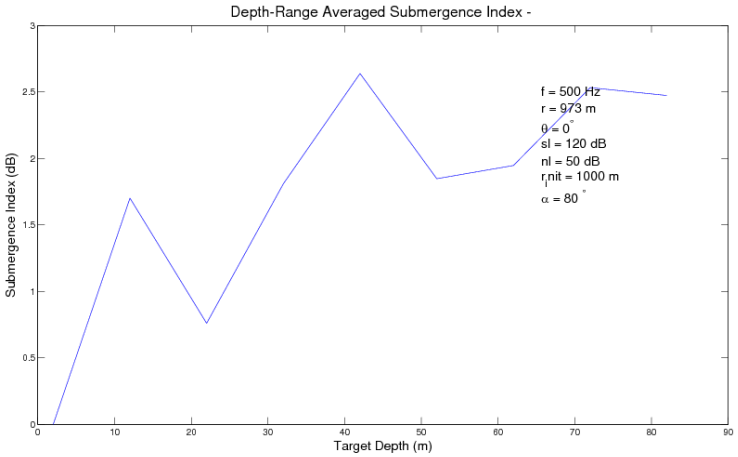

(b) Averaged SI results

Figure 4.16: SI ,500Hz source, downslope 1^0, range $1km$

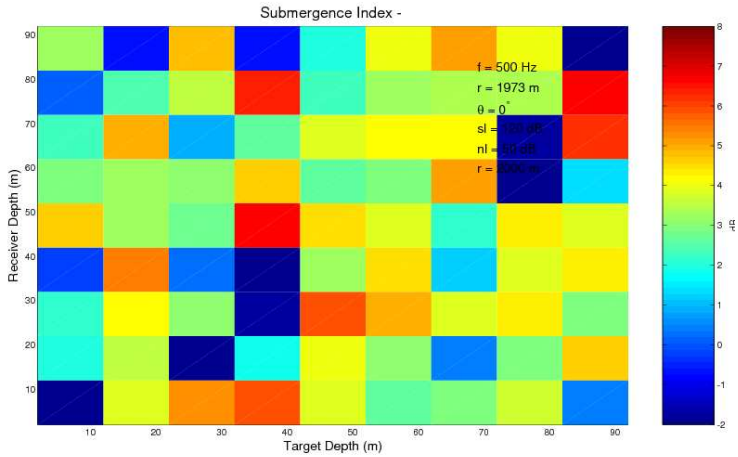

(a) SI for all depth/ receiver depth combinations

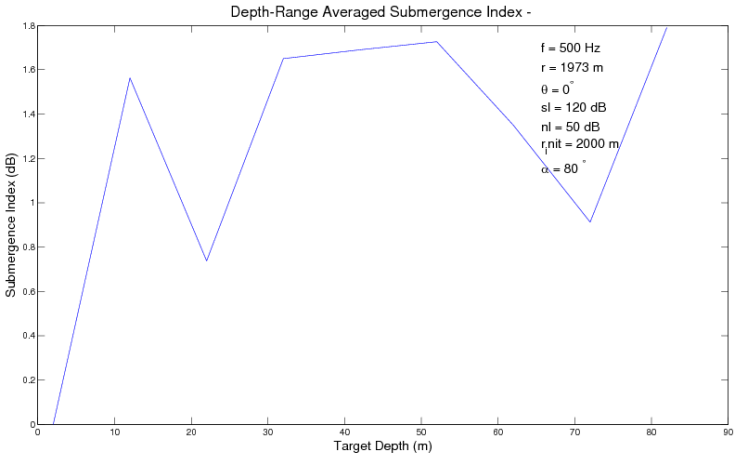

(b) Averaged SI results

Figure 4.17: SI ,500Hz source, downslope 1^0, range $2km$

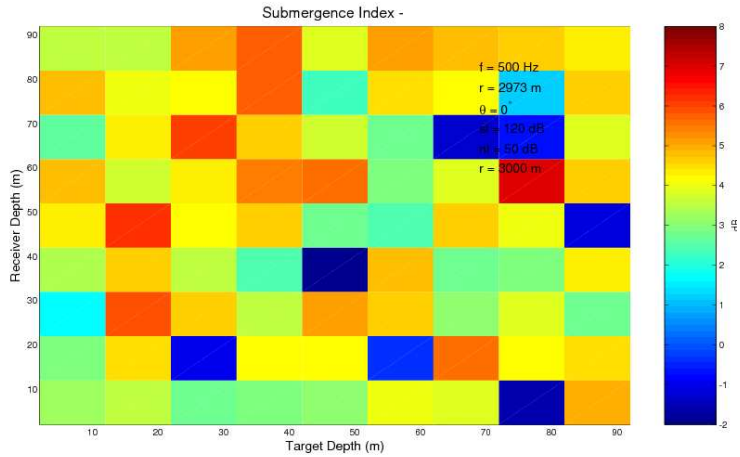

(a) SI for all depth/ receiver depth combinations

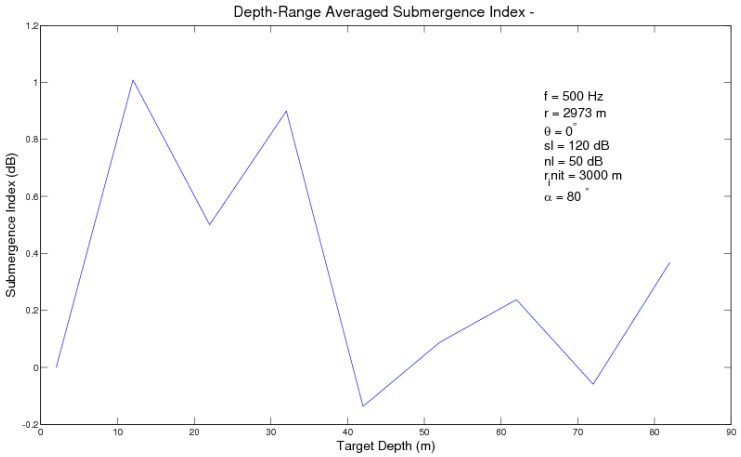

(b) Averaged SI results

Figure 4.18: SI ,500Hz source, downslope 1^0, range $3km$

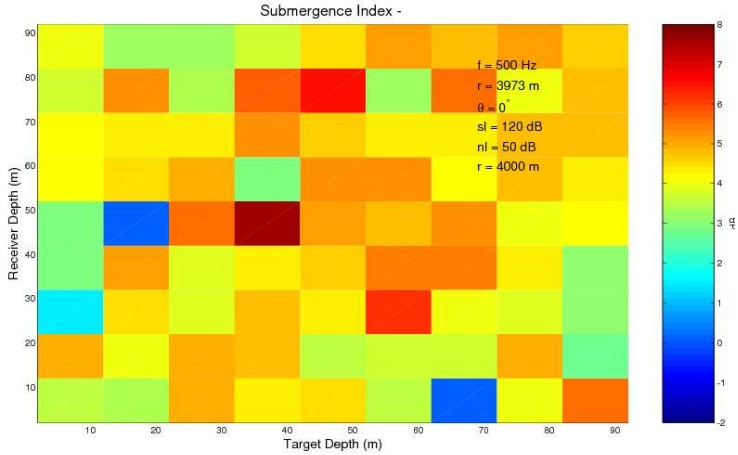

(a) SI for all depth/ receiver depth combinations

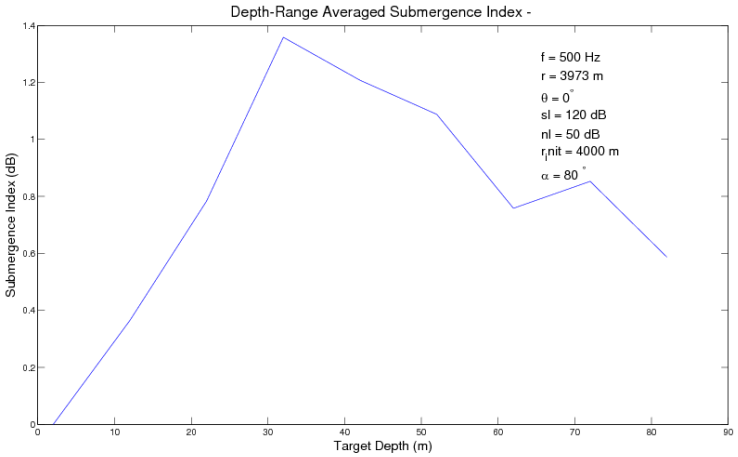

(b) Averaged SI results

Figure 4.19: SI ,500Hz source, downslope 1^0, range $4km$

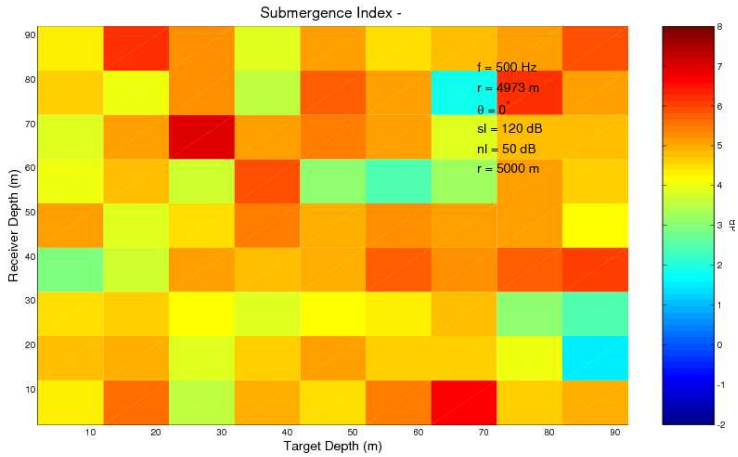

(a) SI for all depth/ receiver depth combinations

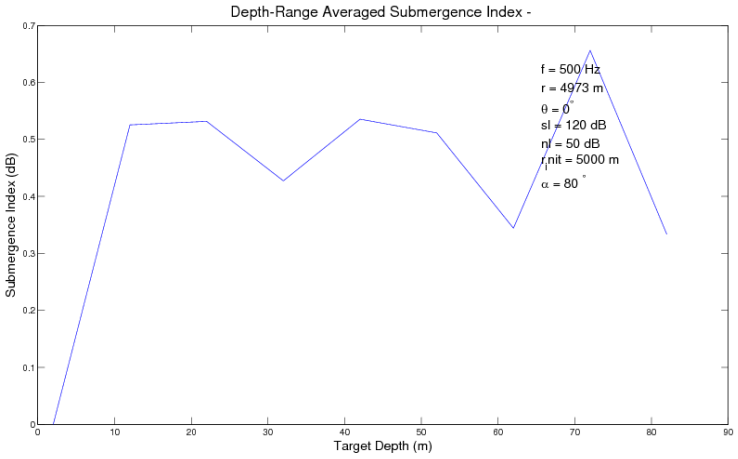

(b) Averaged SI results

Figure 4.20: SI ,500Hz source, downslope 1^0, range $5km$

The results for 1kHz source (Fig.4.21-4.26) also support our assumptions. The results justified our initial intuitive assumptions concerning the downslope impact. However, an upslope environment examination is required before the final conclusions about a range-dependent case can be made.

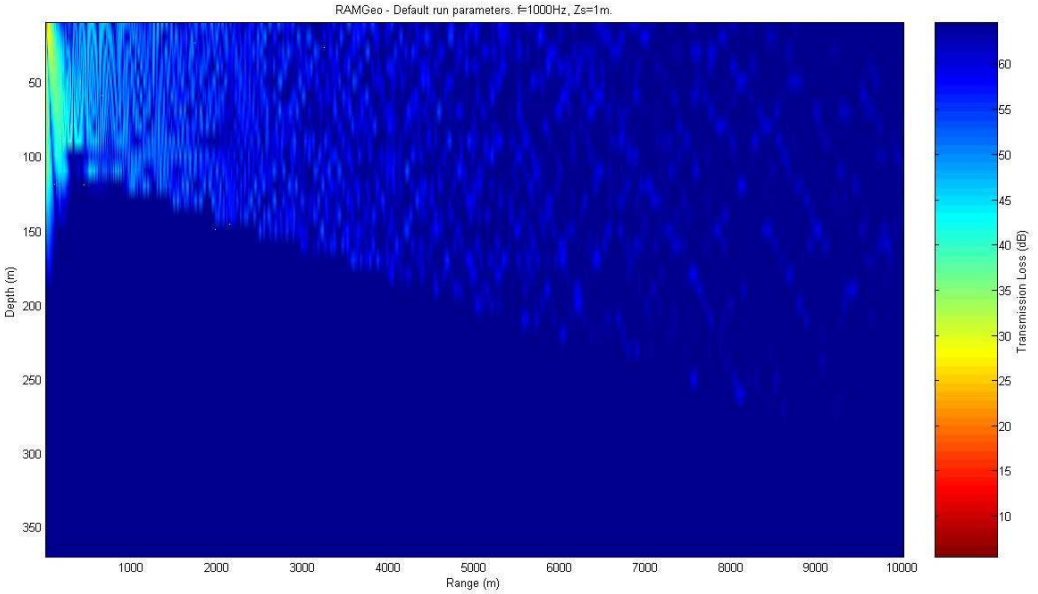

Figure 4.21: Total pressure field, downslope 1^0, 1m depth target, 1kHz

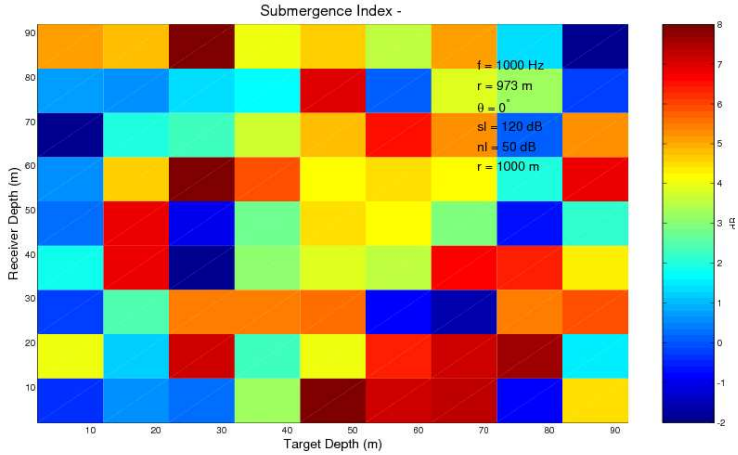

(a) SI for all depth/ receiver depth combinations

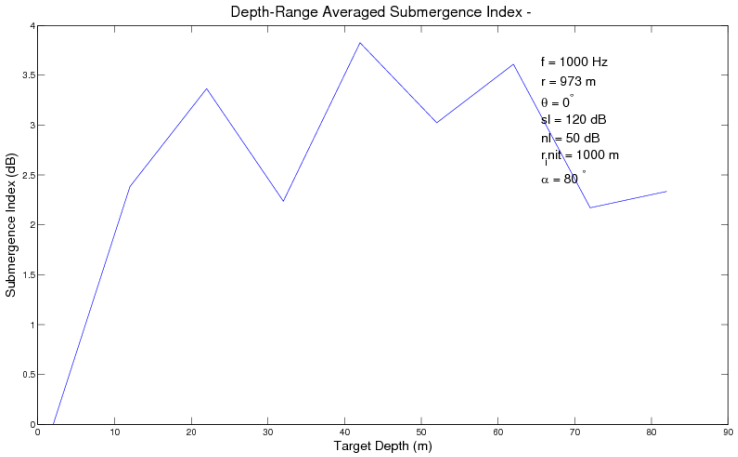

(b) Averaged SI results

Figure 4.22: SI ,1kHz source, downslope 1^0, range $1km$

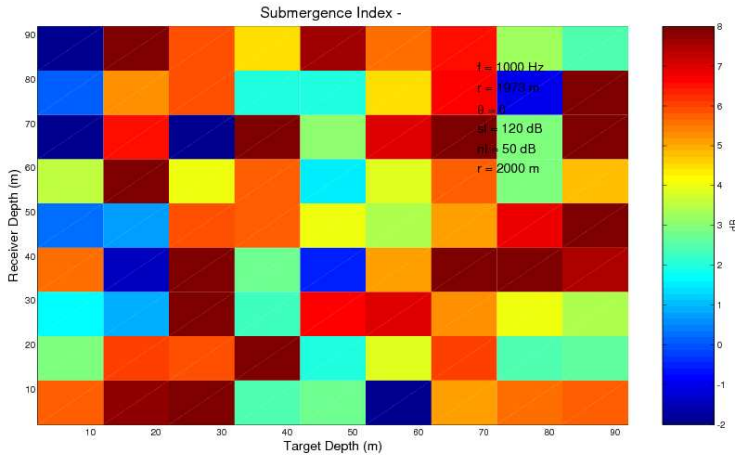

(a) SI for all depth/ receiver depth combinations

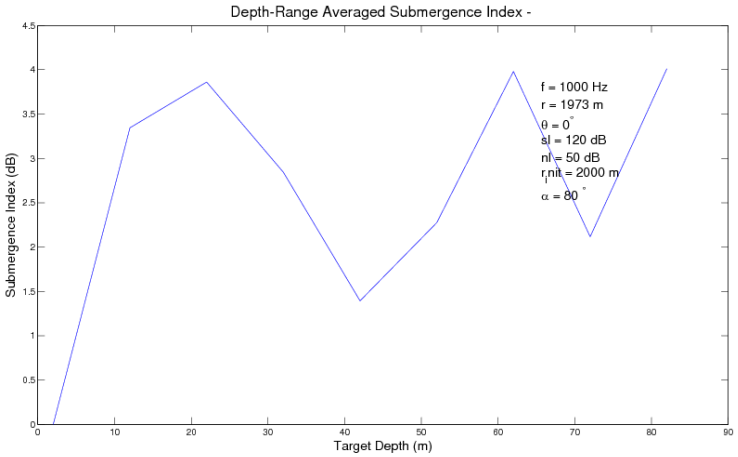

(b) Averaged SI results

Figure 4.23: SI ,1kHz source, downslope 1^0, range $2km$

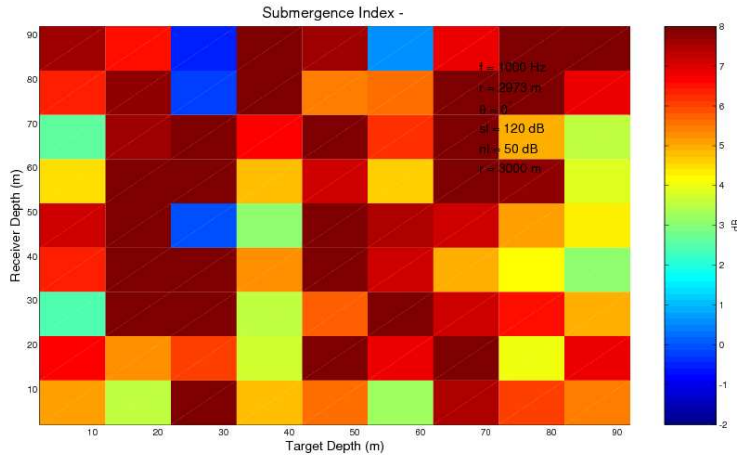

(a) SI for all depth/ receiver depth combinations

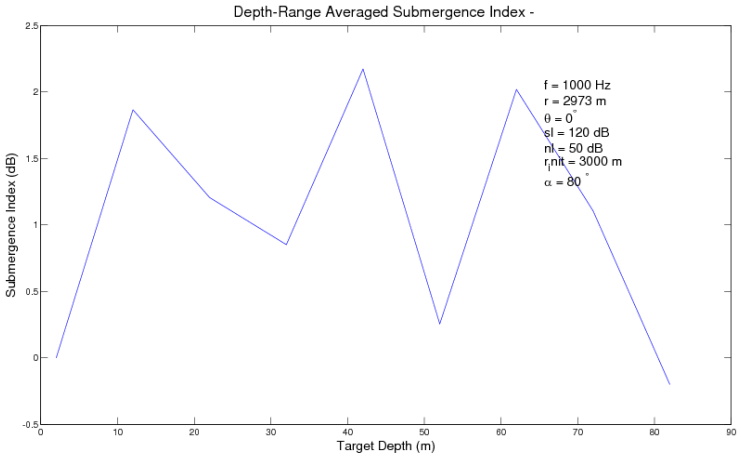

(b) Averaged SI results

Figure 4.24: SI ,1kHz source, downslope 1^0, range $3km$

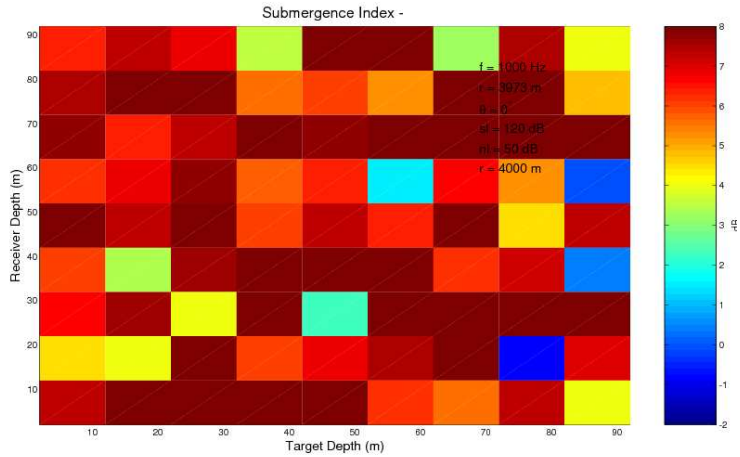

(a) SI for all depth/ receiver depth combinations

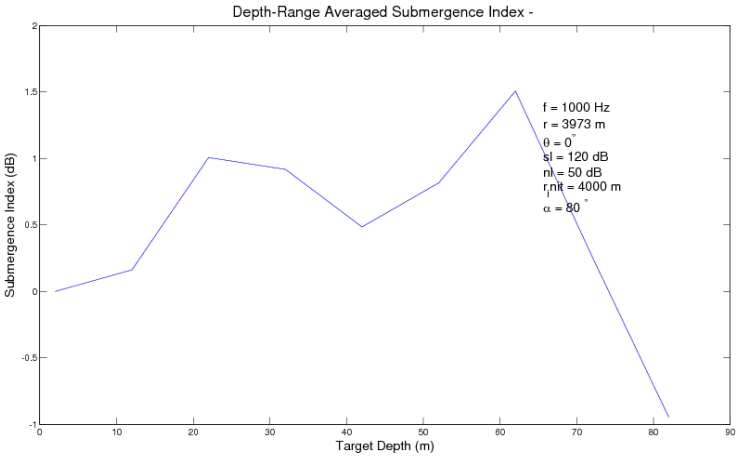

(b) Averaged SI results

Figure 4.25: SI ,1kHz source, downslope 1^0, range $4km$

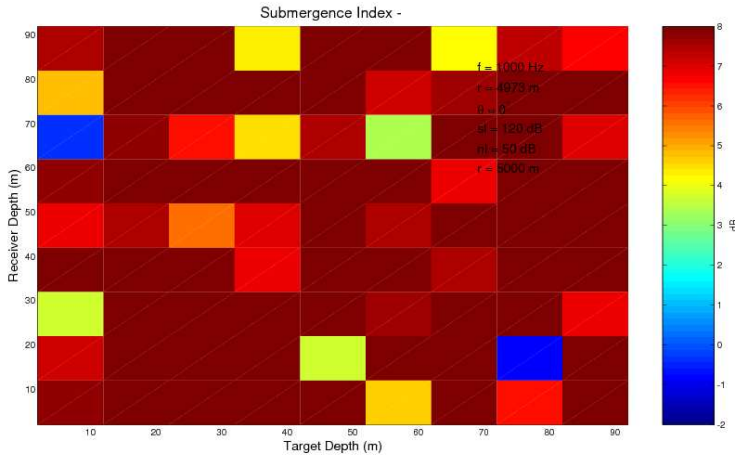

(a) SI for all depth/ receiver depth combinations

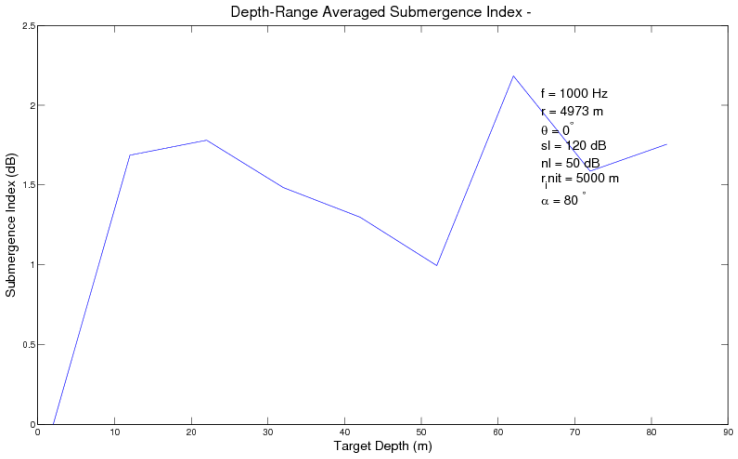

(b) Averaged SI results

Figure 4.26: SI ,1kHz source, downslope 1^0, range $5km$

4.4 SI results for a upslope environment

We started an upslope environment analysis by setting an upslope angle to 1 degree. This case is a 'mirror' case of 1 degree downslope case. A watercolumn depth at a source location has been set to 275m and at range of 8570m the depth has been set to 100m.

The environmental settings are shown in Fig.4.27.

We tested SI results for the same frequencies and ranges as for the downslope cases in order to allow us to compare between the two environmental scenarios. The 500Hz simulation results are shown in Fig. 4.28-4.33.

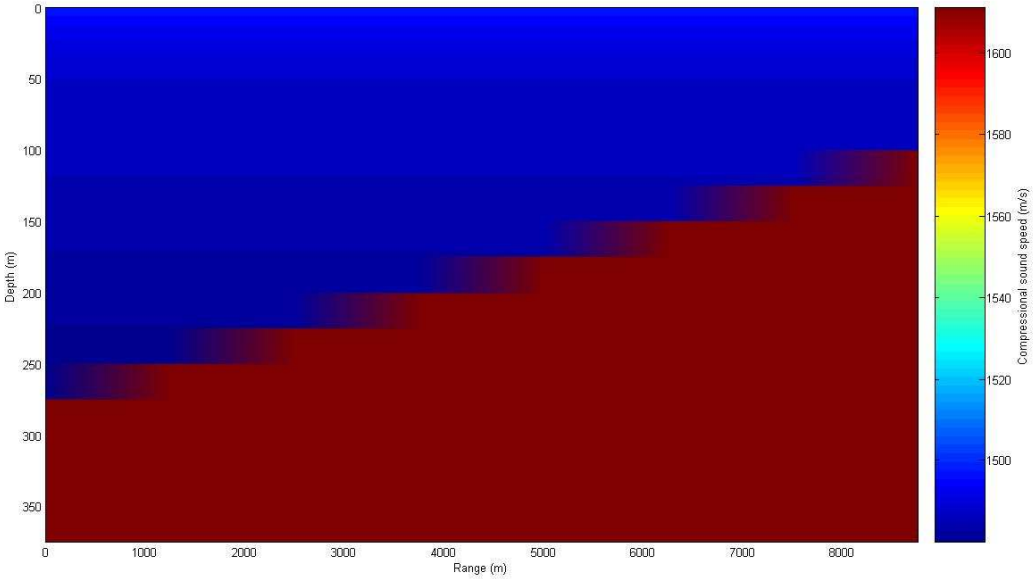

Figure 4.27: Upslope 1 degree, soundspeed profile

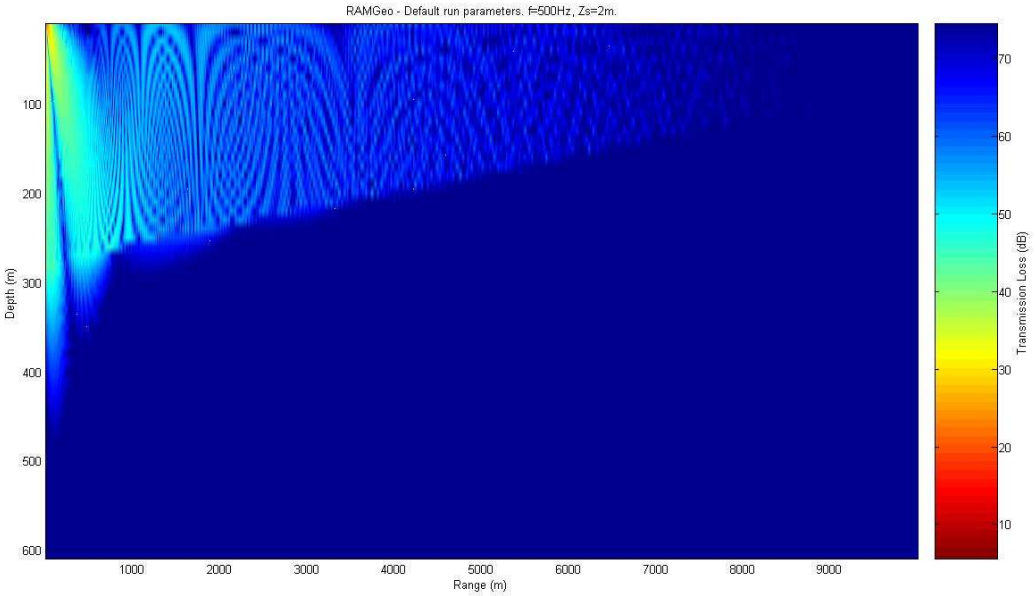

Figure 4.28: Total pressure field, upslope 1^0, 2m depth target, 500Hz

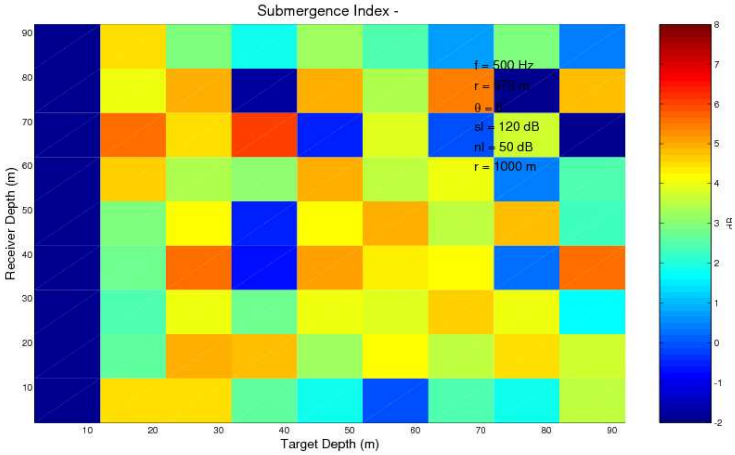

(a) SI for all depth/ receiver depth combinations

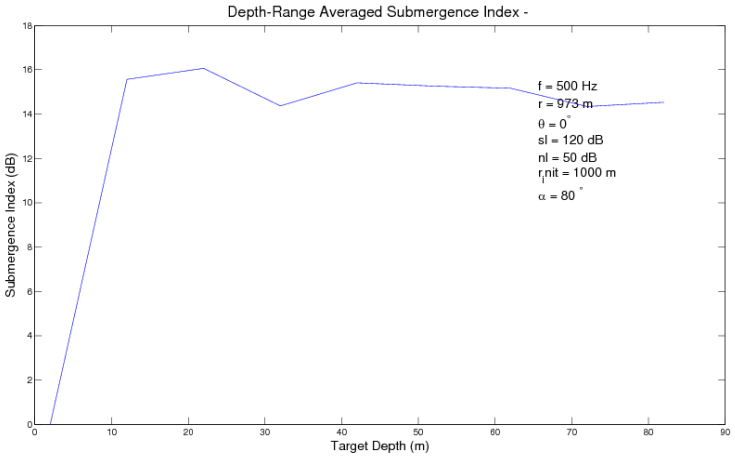

(b) Averaged SI results

Figure 4.29: SI ,500Hz source, upslope 1^0, range $1km$

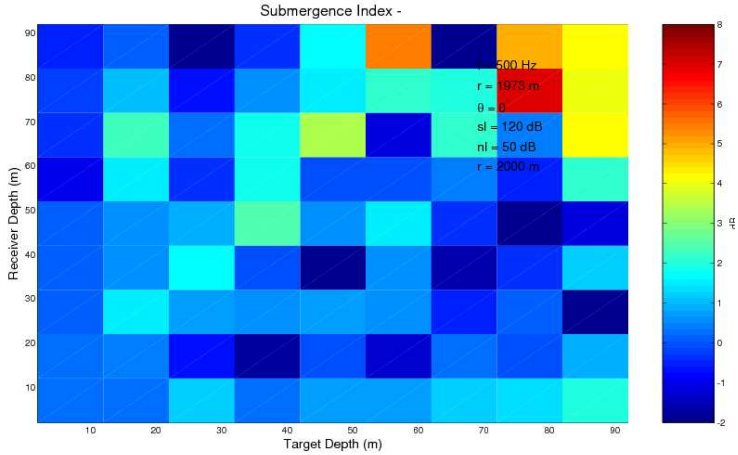

(a) SI for all depth/ receiver depth combinations

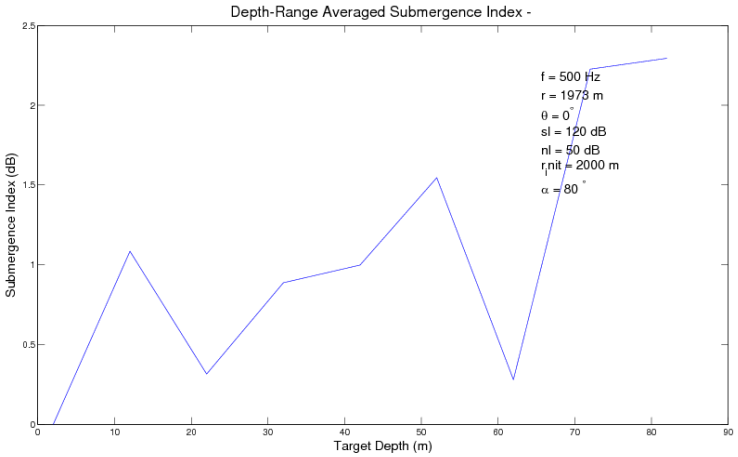

(b) Averaged SI results

Figure 4.30: SI ,500Hz source, upslope 1^0, range $2km$

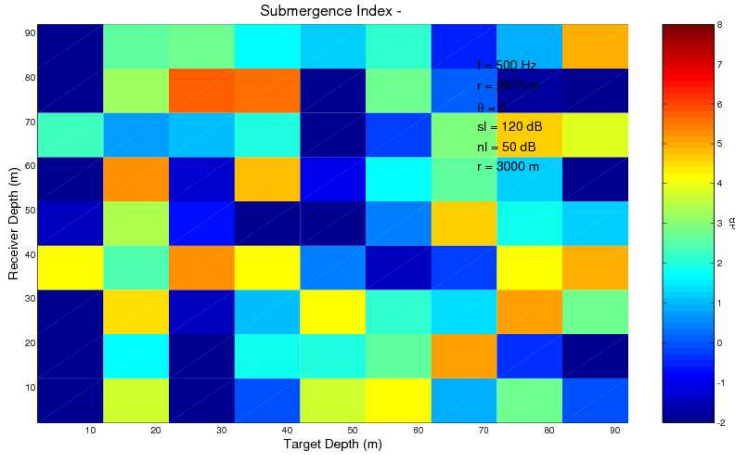

(a) SI for all depth/ receiver depth combinations

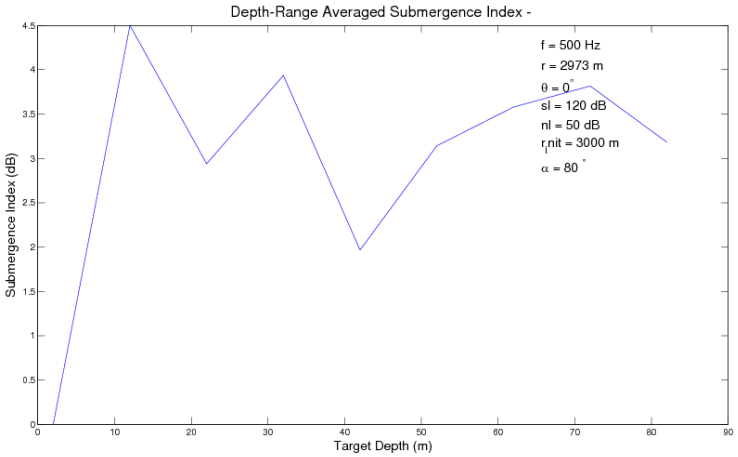

(b) Averaged SI results

Figure 4.31: SI ,500Hz source, upslope 1^0, range $3km$

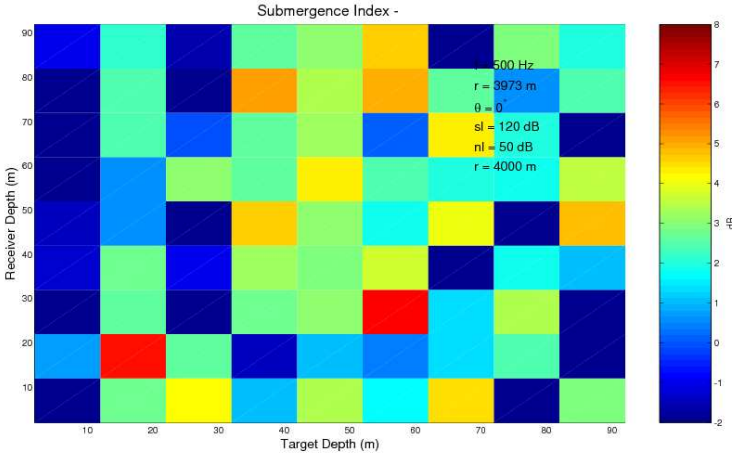

(a) SI for all depth/ receiver depth combinations

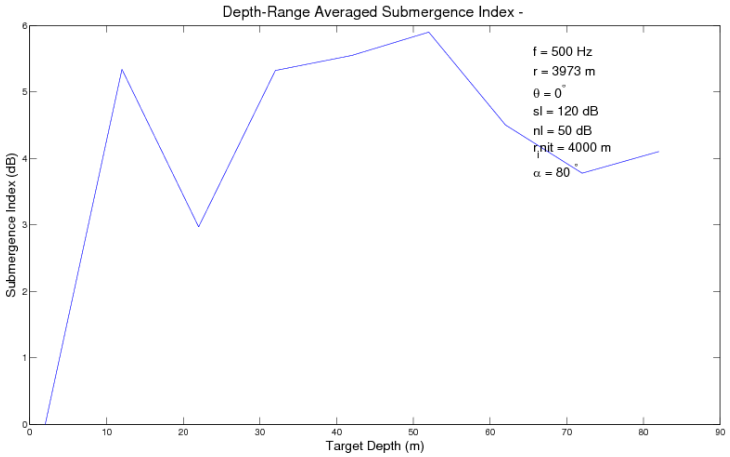

(b) Averaged SI results

Figure 4.32: SI ,500Hz source, upslope 1^0, range $4km$

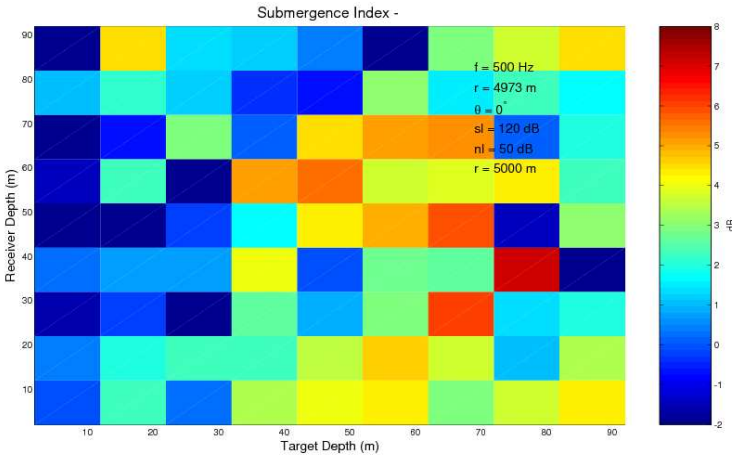

(a) SI for all depth/ receiver depth combinations

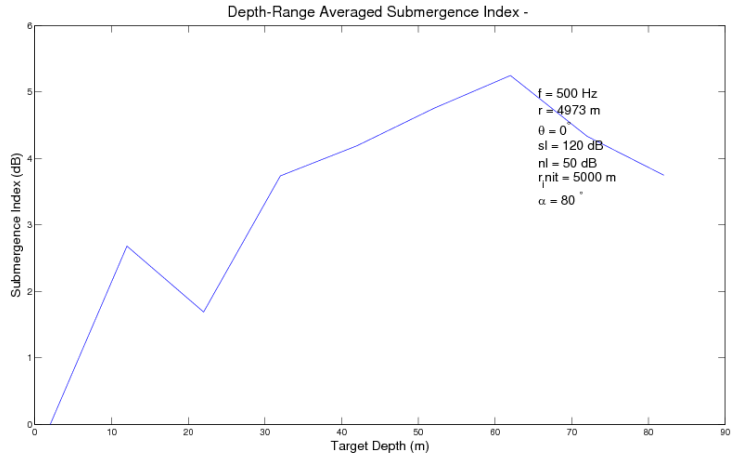

(b) Averaged SI results

Figure 4.33: SI ,500Hz source, upslope 1^0, range $5km$

The results are indicating tremendous improvement of SI capabilities in mild upslope environment. We continued to test the results for farther than 5km's from the source and for all of them up to 9km we found that the SI separation value is 2dB at least between surface and submerged targets. However, we can't disregard from misleading SI results at range of 2km (Fig.4.30). To explain this anomaly we have to analyze a pressure field at this range (Fig.4.28) as we did in the range-independent case. The pressure field's value drops at 2km range. Therefore this specific range belongs to a category of the 'shadow' area and we already learned that these areas can lead to errors in the SI estimation of a target location. The first study case outcome is definitely supporting our previous assumptions, yet additional scenario's examination is required.

We will investigate now 1kHz source under the same environmental conditions. The results are shown in Fig.4.35-4.39. The high level of correlation between SI values of the two frequencies can be noticed. Although it is possible to make the final conclusions even at this stage, to strengthen them we will test a 2 degrees upslope case.

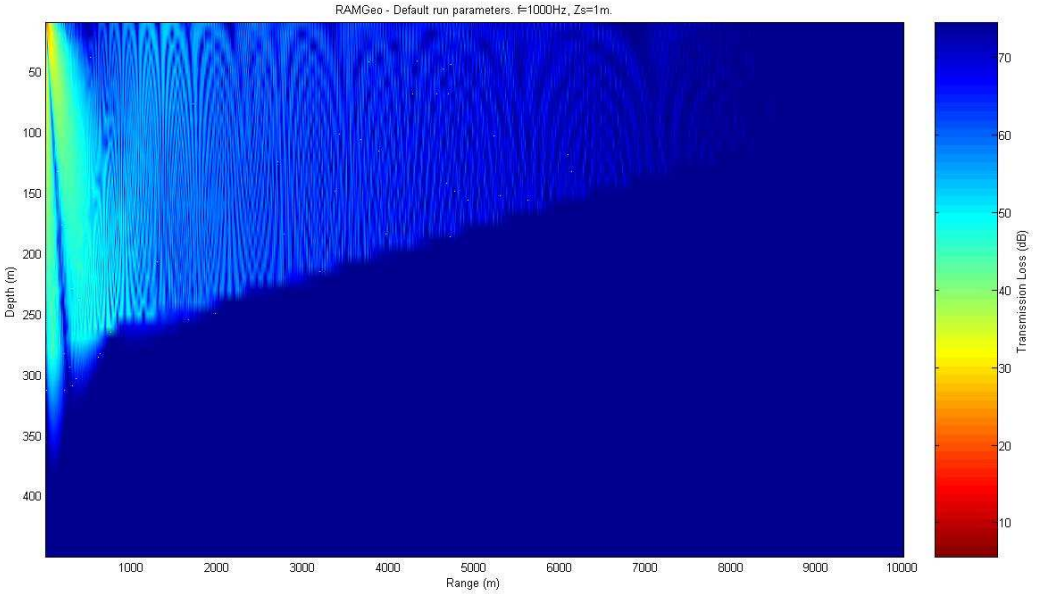

Figure 4.34: Total pressure field, upslope 1^0, 1m depth target, 1kHz

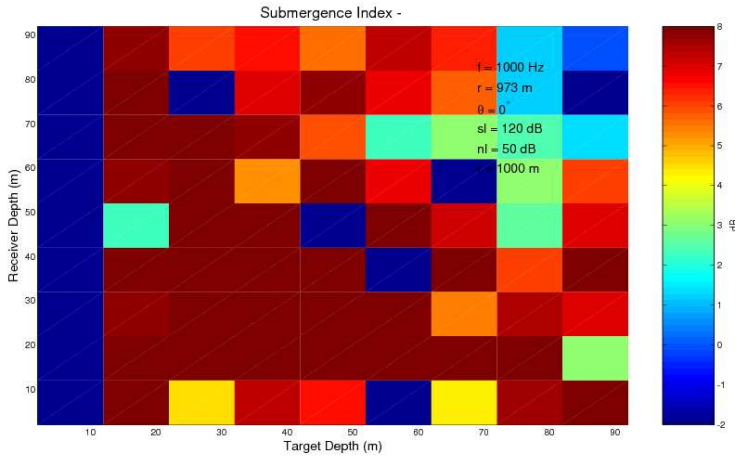

(a) SI for all depth/ receiver depth combinations

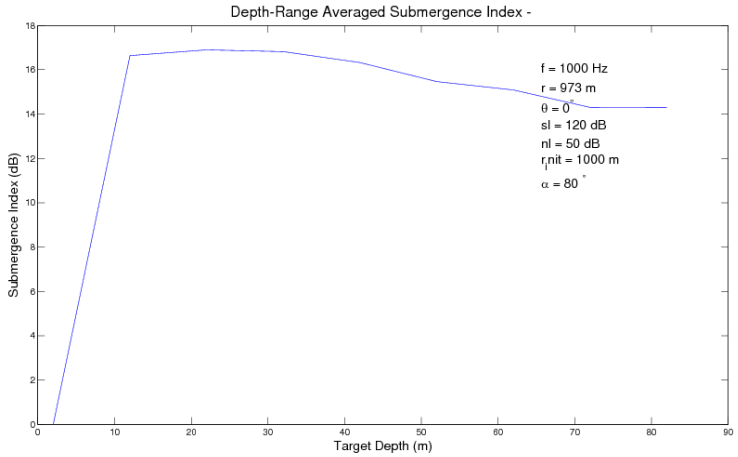

(b) Averaged SI results

Figure 4.35: SI ,1kHz source, upslope 1^0, range $1km$

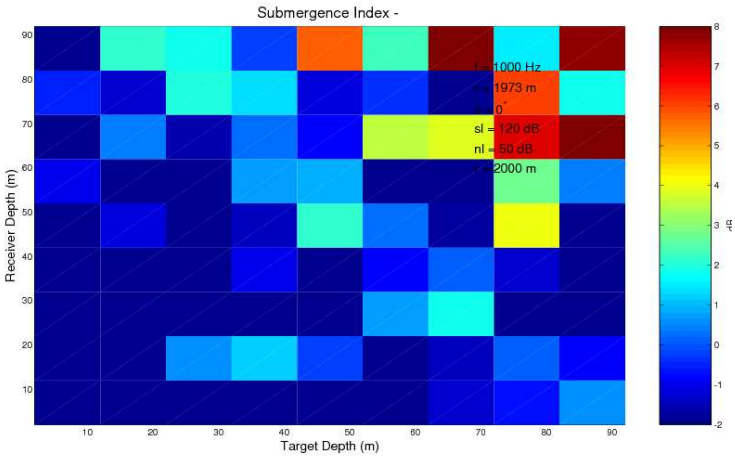

(a) SI for all depth/ receiver depth combinations

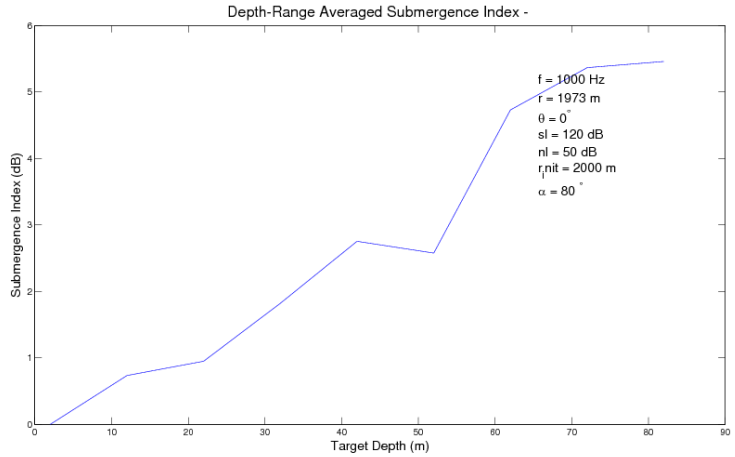

(b) Averaged SI results

Figure 4.36: SI ,1kHz source, upslope 1^0, range $2km$

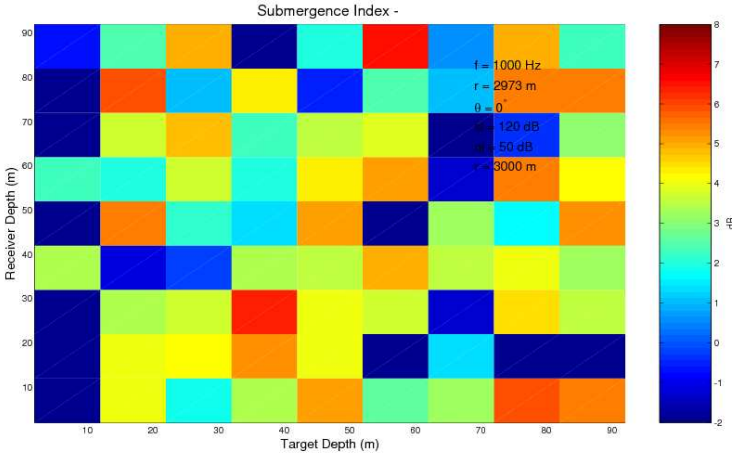

(a) SI for all depth/ receiver depth combinations

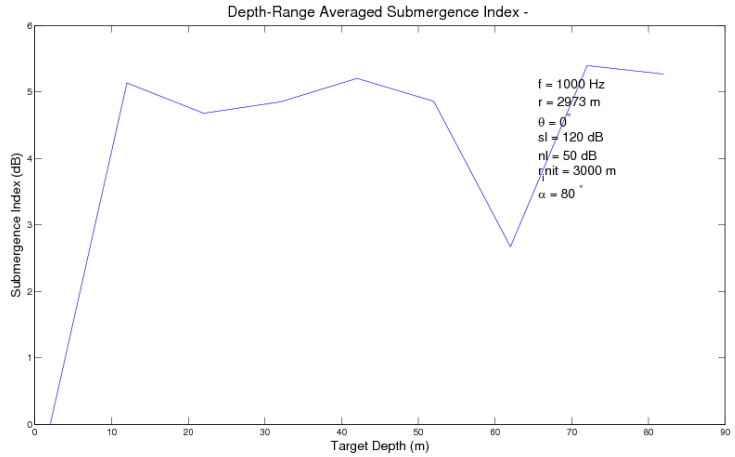

(b) Averaged SI results

Figure 4.37: SI ,1kHz source, upslope 1^0, range $3km$

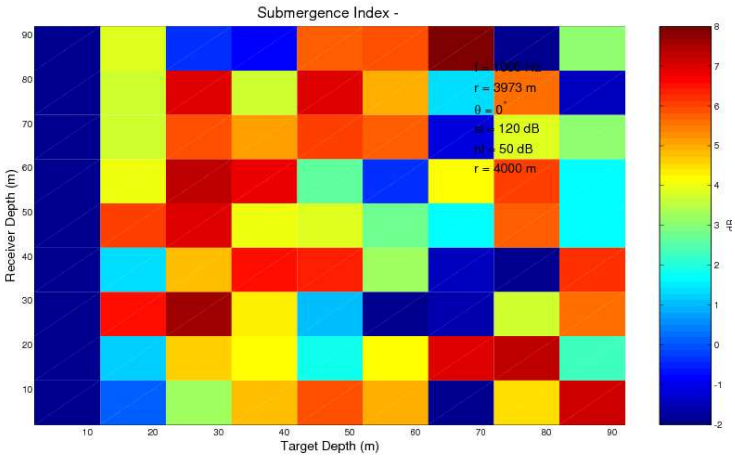

(a) SI for all depth/ receiver depth combinations

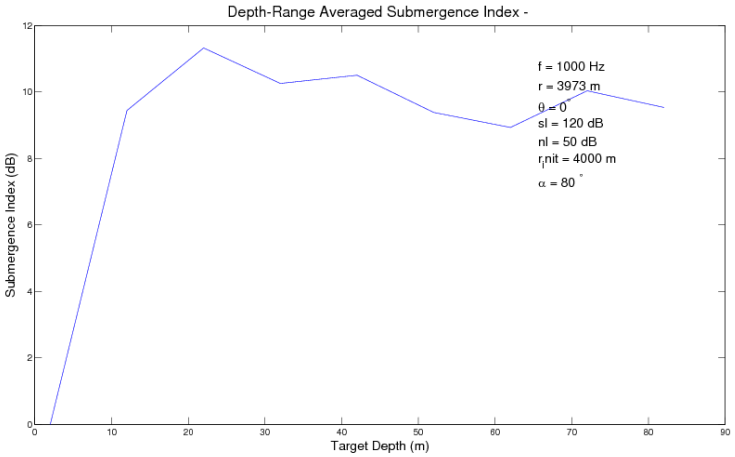

(b) Averaged SI results

Figure 4.38: SI ,1kHz source, upslope 1^0, range $4km$

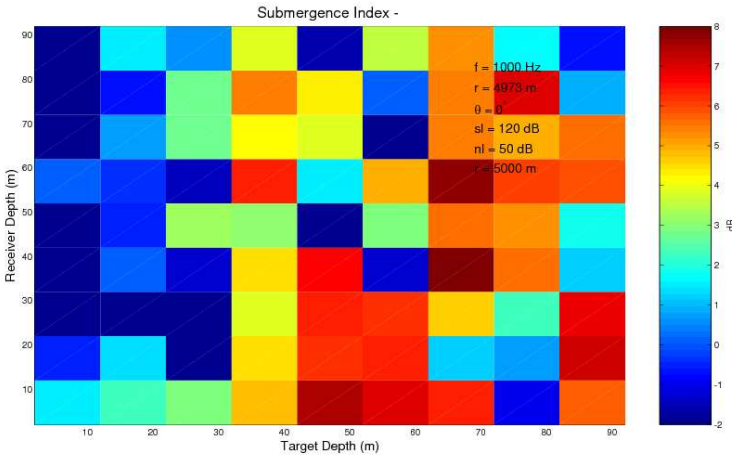

(a) SI for all depth/ receiver depth combinations

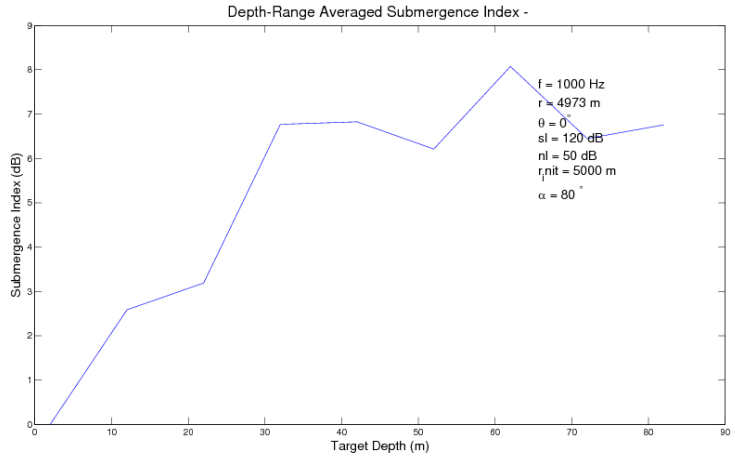

(b) Averaged SI results

Figure 4.39: SI ,1kHz source, upslope 1^0, range $5km$

The environmental settings for the 2 degrees upslope are shown in Fig.4.40 and the simulation results for 500Hz and 1kHz case up to 5km ranges are in Fig.4.41-4.52. We can learn from the results that a higher slope elevation will deliver reasonable SI capabilities, though for some ranges (1km and 3km) a downgrade of performances can be expected. The reason for the problematic ranges is hidden in the phenomena of a destructive interference of normal modes that can cause a creation of the 'shadow' areas in these ranges. An examination of ranges above 5km limit supplied satisfying results with averaged separation values of 2dB at least.

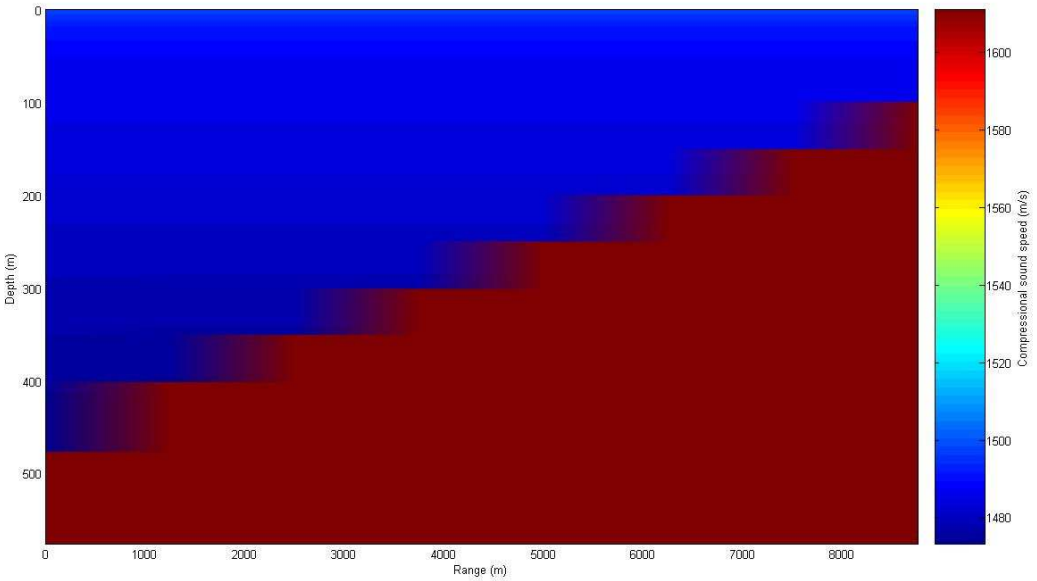

Figure 4.40: Upslope 2 degrees, soundspeed profile

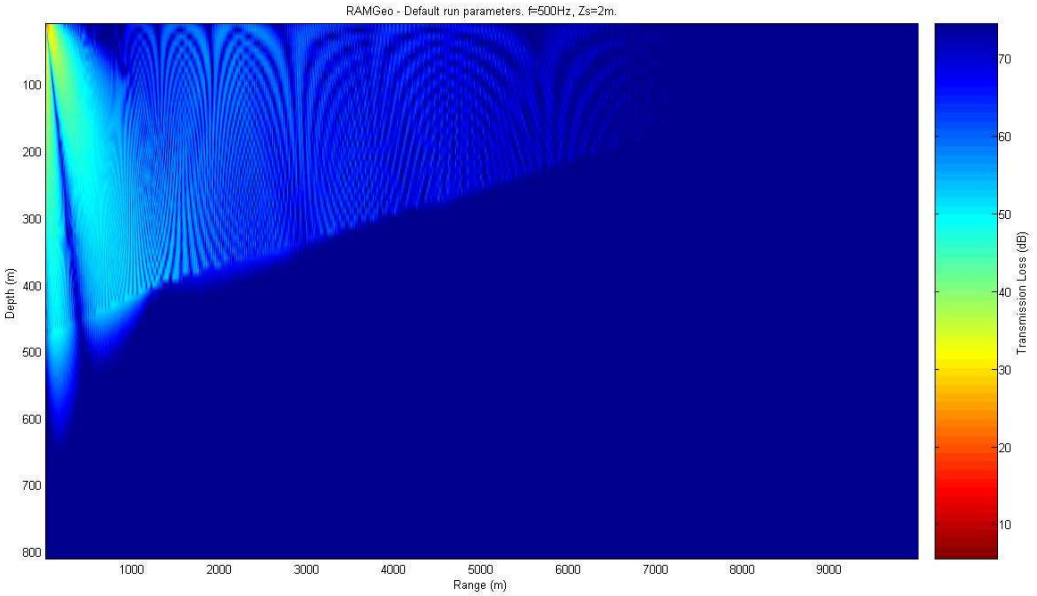

Figure 4.41: Total pressure field, upslope 2^0, 2m depth target, 500Hz

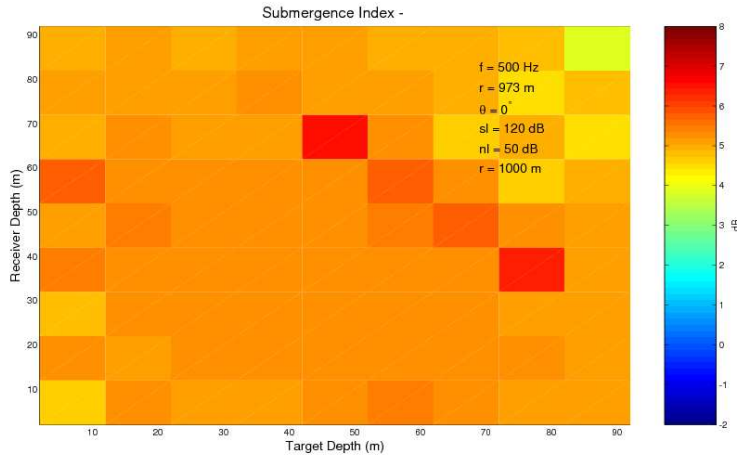

(a) SI for all depth/ receiver depth combinations

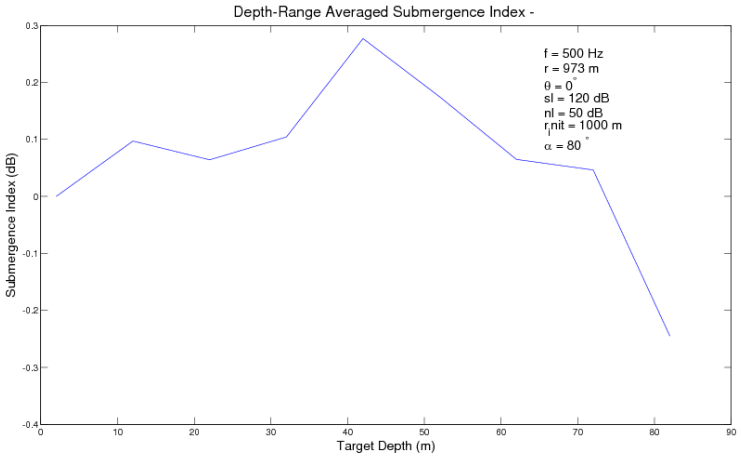

(b) Averaged SI results

Figure 4.42: SI ,500Hz source, upslope 2^0, range $1km$

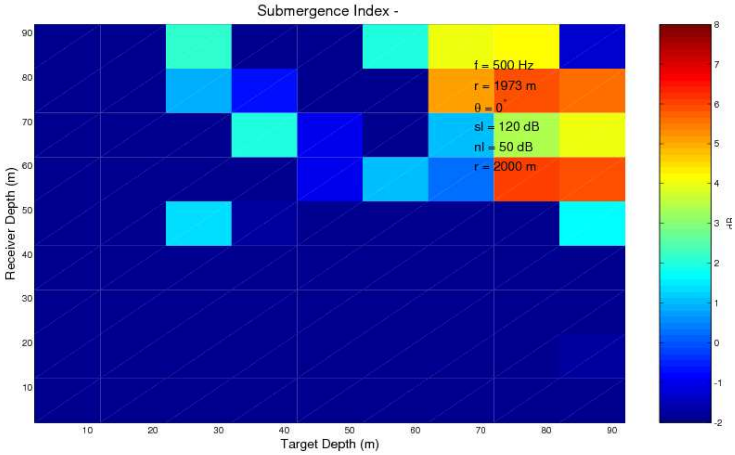

(a) SI for all depth/ receiver depth combinations

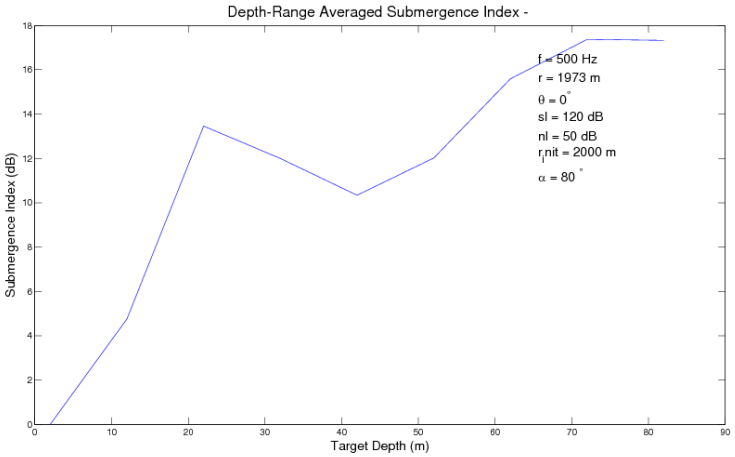

(b) Averaged SI results

Figure 4.43: SI ,500Hz source, upslope 2^0, range $2km$

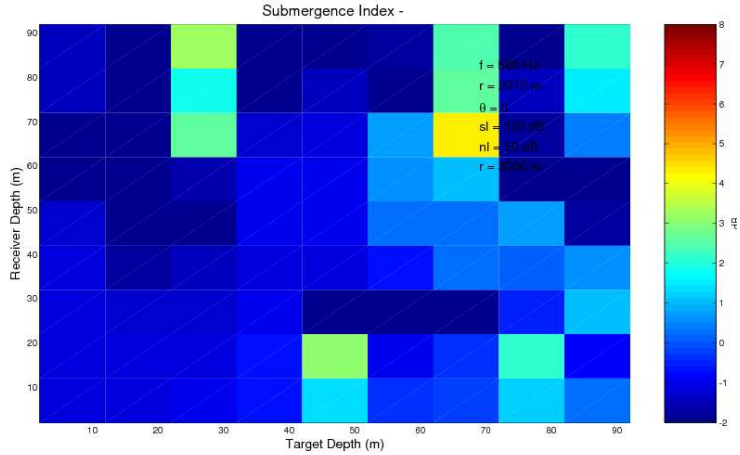

(a) SI for all depth/ receiver depth combinations

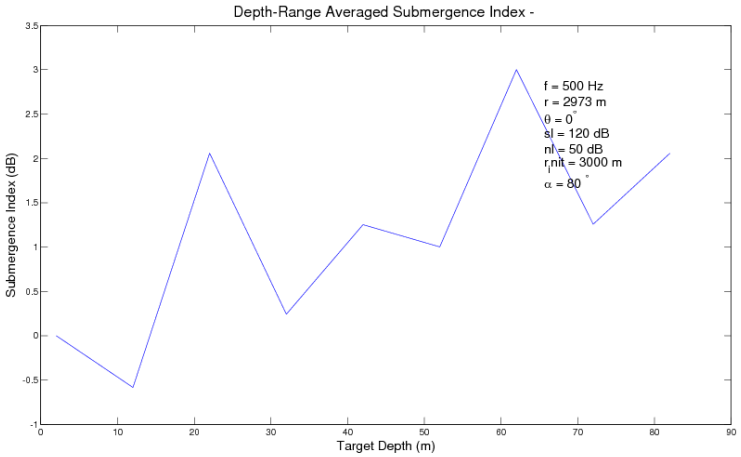

(b) Averaged SI results

Figure 4.44: SI ,500Hz source, upslope 2^0, range $1km$

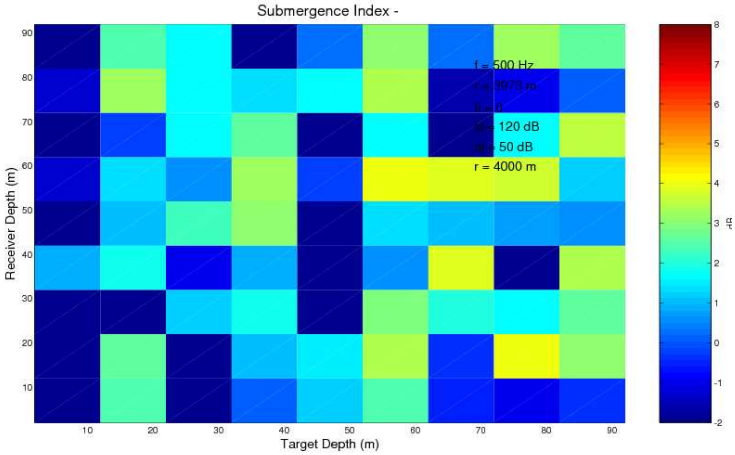

(a) SI for all depth/ receiver depth combinations

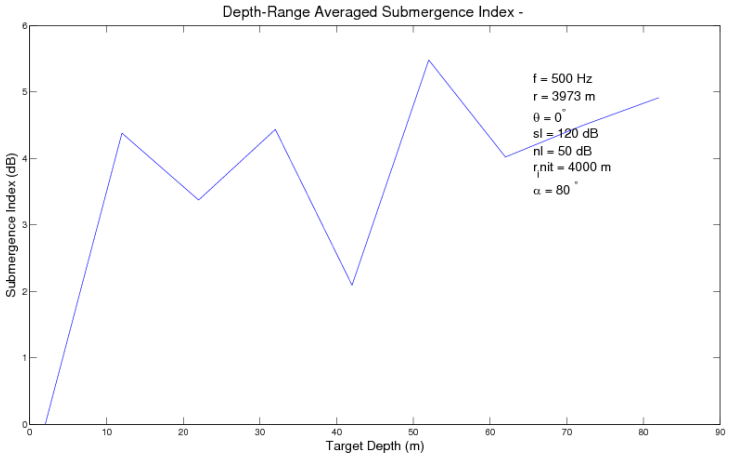

(b) Averaged SI results

Figure 4.45: SI ,500Hz source, upslope 2^0, range $4km$

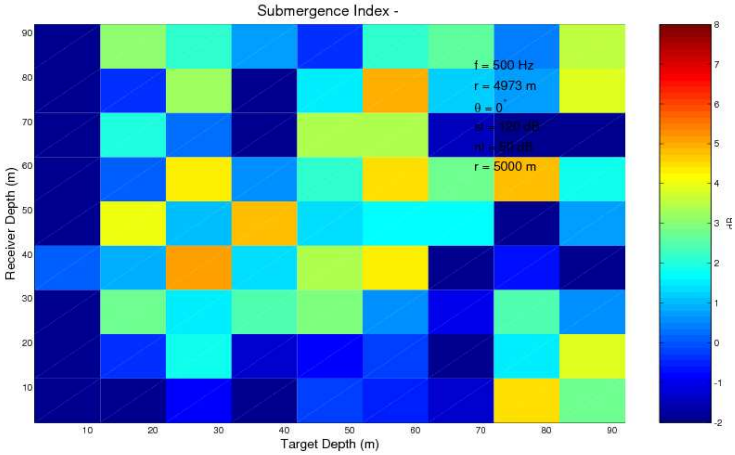

(a) SI for all depth/ receiver depth combinations

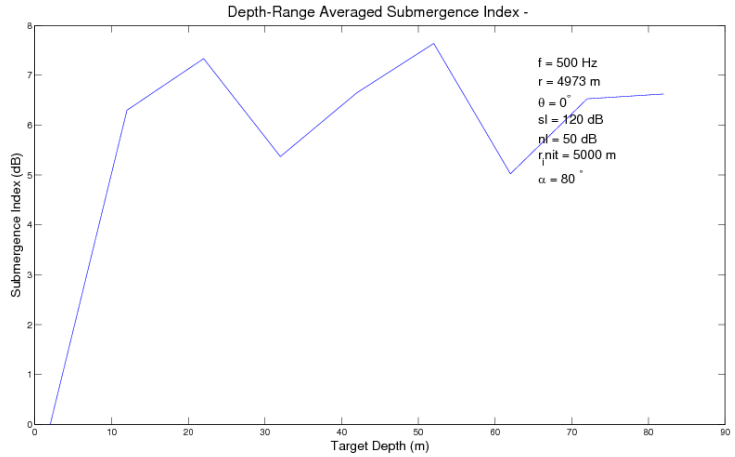

(b) Averaged SI results

Figure 4.46: SI ,500Hz source, upslope 2^0, range $5km$

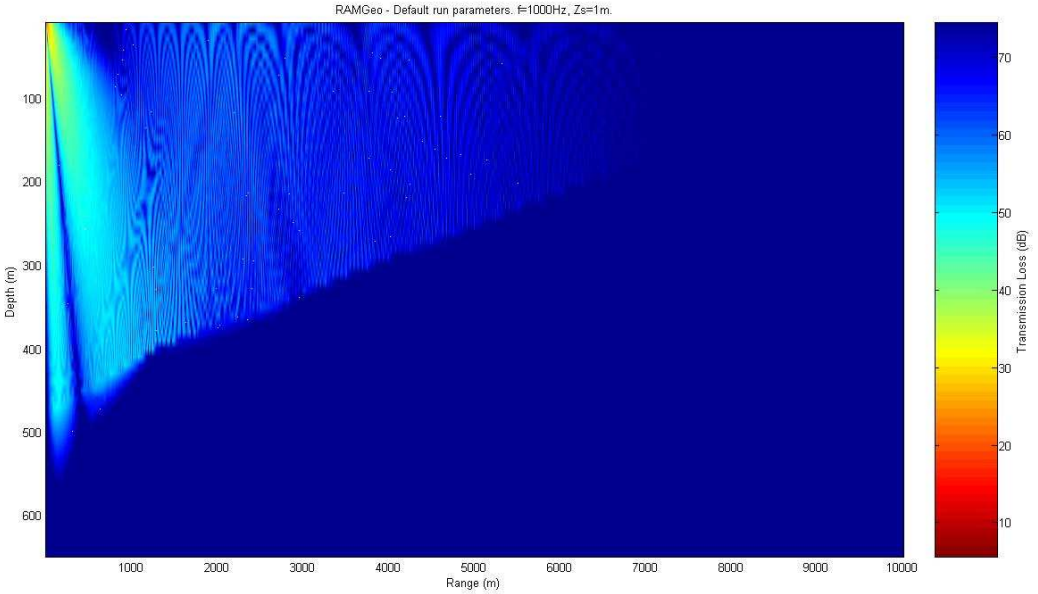

Figure 4.47: Total pressure field, upslope 2^0, 1m depth target, 1kHz

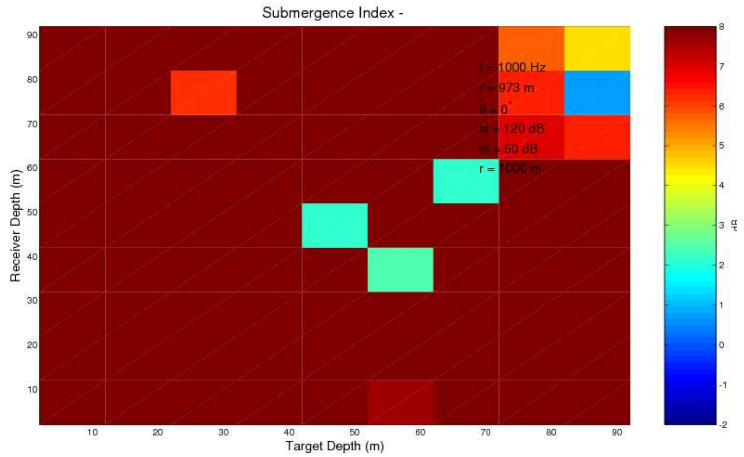

(a) SI for all depth/ receiver depth combinations

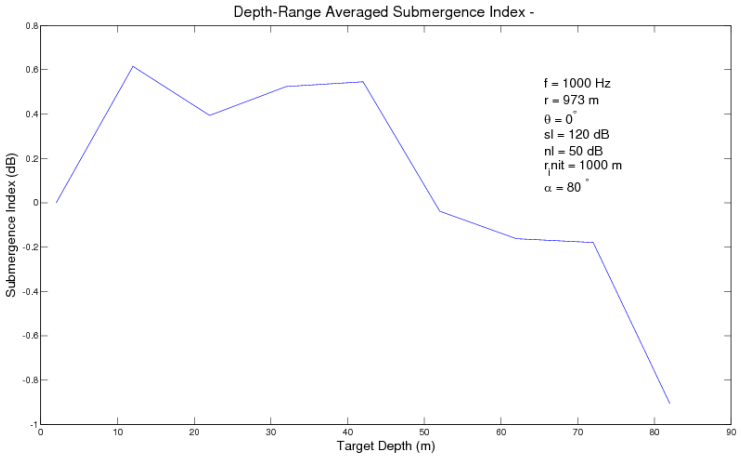

(b) Averaged SI results

Figure 4.48: SI ,1kHz source, upslope 2^0, range $1km$

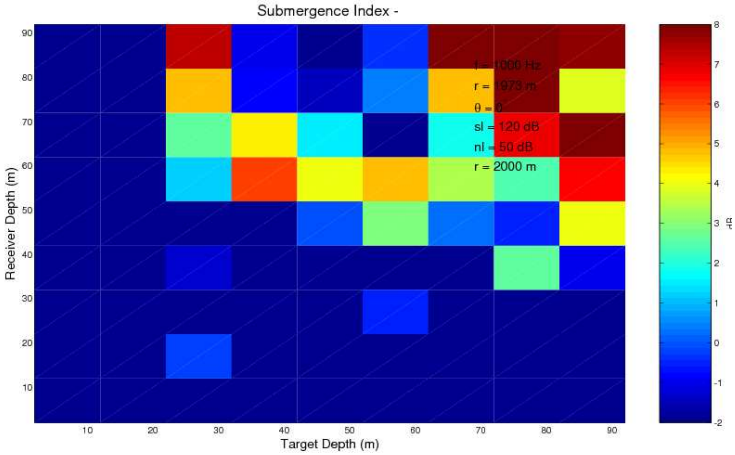

(a) SI for all depth/ receiver depth combinations

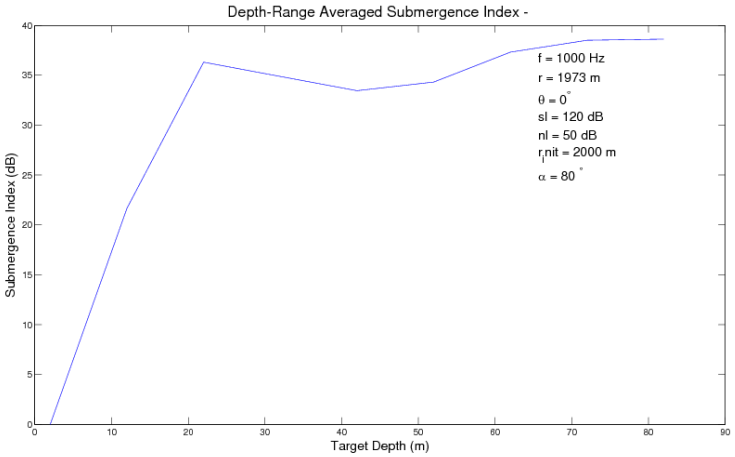

(b) Averaged SI results

Figure 4.49: SI ,1kHz source, upslope 2^0, range $2km$

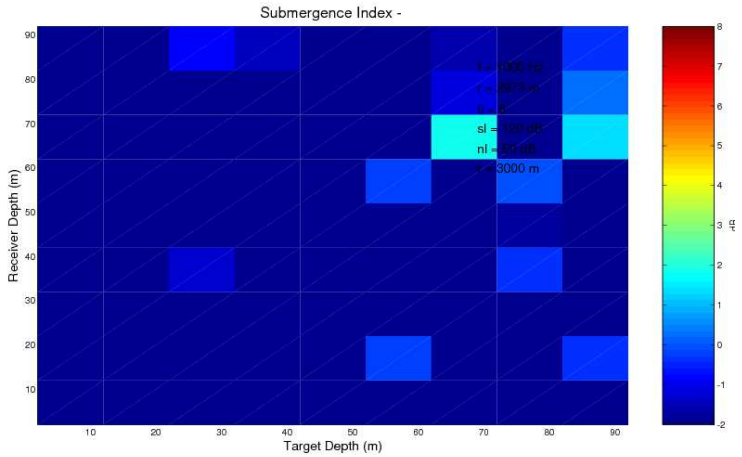

(a) SI for all depth/ receiver depth combinations

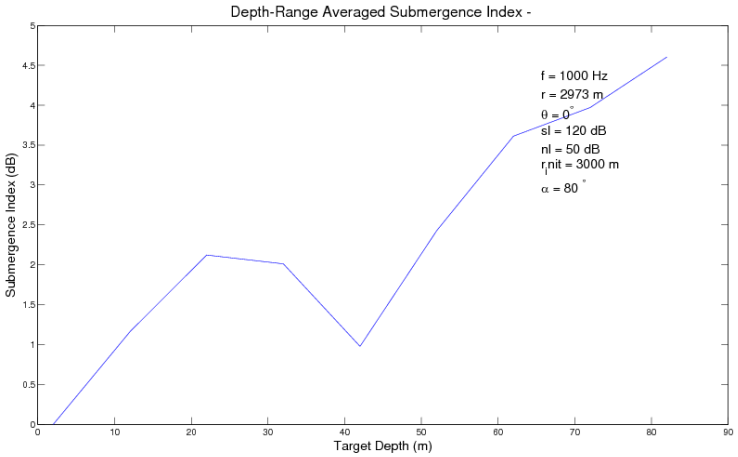

(b) Averaged SI results

Figure 4.50: SI ,1kHz source, upslope 2^0, range $3km$

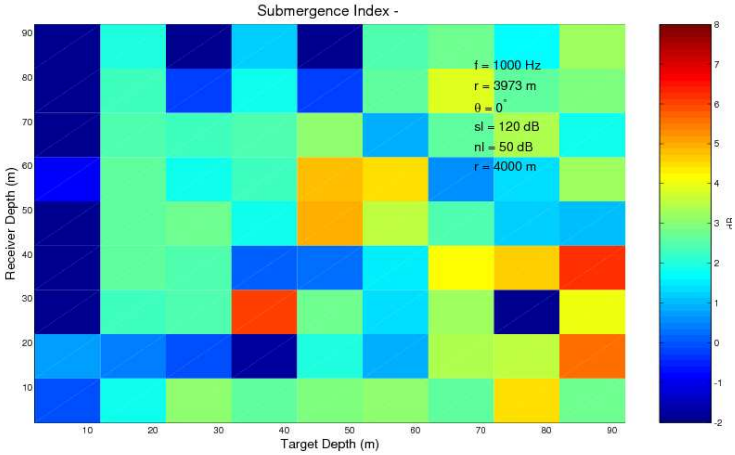

(a) SI for all depth/ receiver depth combinations

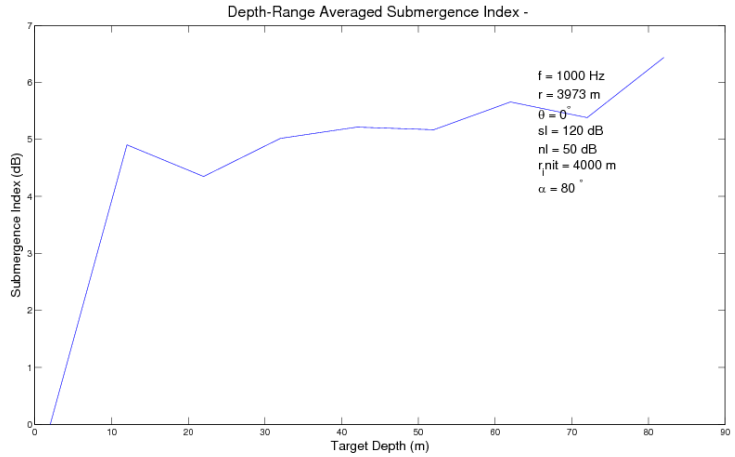

(b) Averaged SI results

Figure 4.51: SI ,1kHz source, upslope 2^0, range $4km$

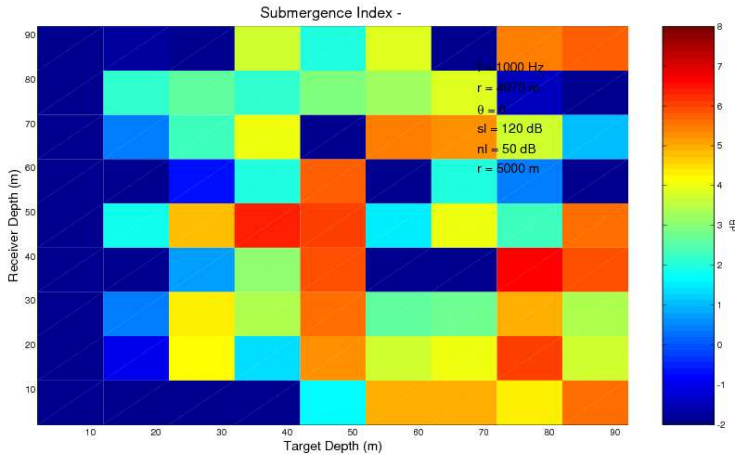

(a) SI for all depth/ receiver depth combinations

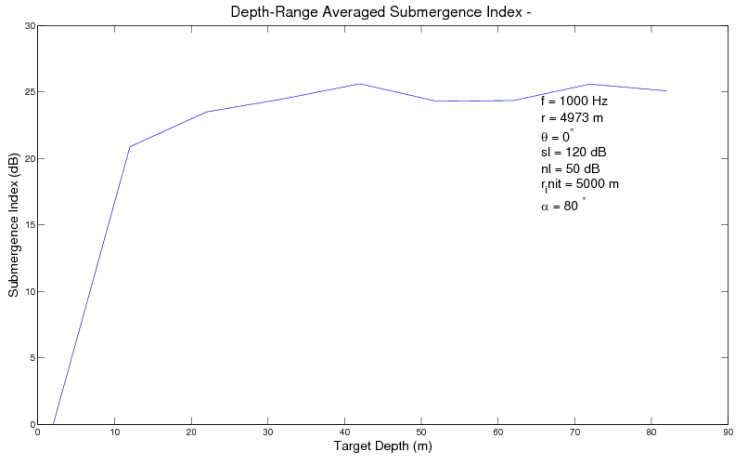

(b) Averaged SI results

Figure 4.52: SI ,1kHz source, upslope 2^0, range $5km$

We can summarize at this point that the upslope environment has a constructive influence on SI performances and this fact can be very useful for future applications. This conclusion also supports our preliminary assumptions about the impact of a wedge on SI calculations.

4.5 Bottom attenuation

We next to explore the SI dependency on bottom attenuation. It is reasonable to assume that a losy bottom could cause to some changes in modal energy distribution, and as a result, the SI performance could be questionable. We tried to examine this assumption for both downslope and upslope cases by increasing a bottom attenuation value twice, up to $0.8\frac{dB}{\lambda}$. By comparing our new results to the previously presented results we hardly found any differences as long in SI performance, in particular for ranges up to 5 km. The

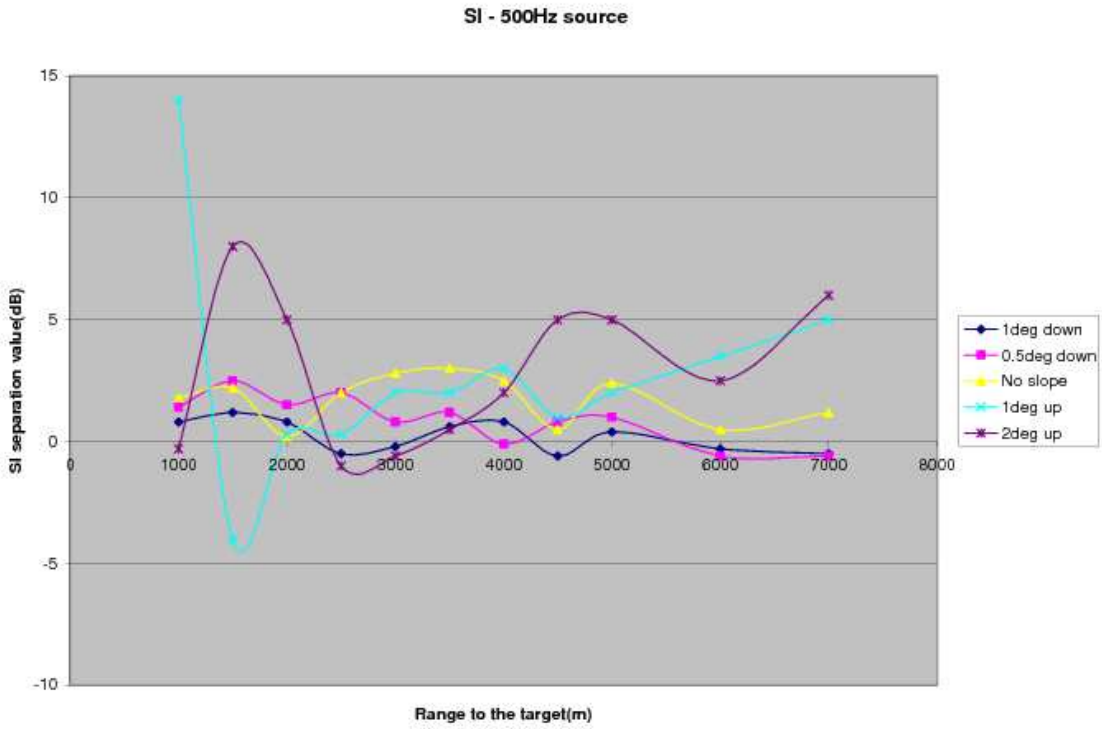

Figure 4.53: SI separation capabilities for range-dependent/independent cases, 500Hz source

quantitative comparison of the results will be presented in the next section.

4.6 Quantitative comparison of range-dependent results.

Although many cases were presented, it's still hard to decide what will be an optimal range for a target recognition just by looking at separate cases. Some criterias for comparing results are required. We decided to identify in each case the worst separation value result. For example, if any non-surface target in the specific scenario produced an SI value of 0.1dB relatively to a surface target, the worst separation value for this scenario will be equal to 0.1dB. By creating this parameter we can compare all the cases and to define a general behavior pattern.

Results for a 500Hz source are collected in Fig.4.53. It is clear from the results that for a 500Hz target the depth discrimination will be more effective for upslope geometry and allocation of a receiver between 3.5 and 7.0 km at range.

The pattern repeats itself for 1kHz source (Fig. 4.54). Here again the upslope presence has a positive impact on SI separation performance.

It is interesting to notice that the slope presence creates some oscillating pattern in the SI values. The same oscillating pattern has been noticed by S.T. McDaniel [24] during an investigation of mode coupling and modal energy distribution. One of McDaniel results are shown in Fig.4.55. The results in Fig. 4.55

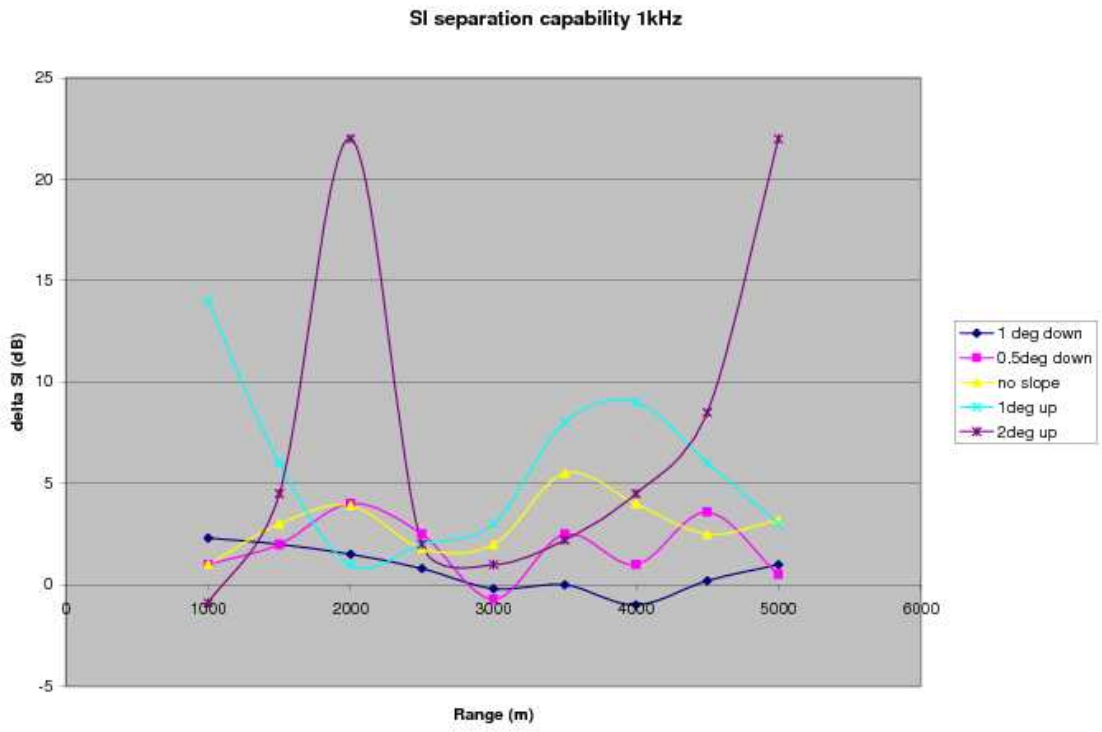

Figure 4.54: SI separation capabilities for range-dependent/independent cases, 1kHz source

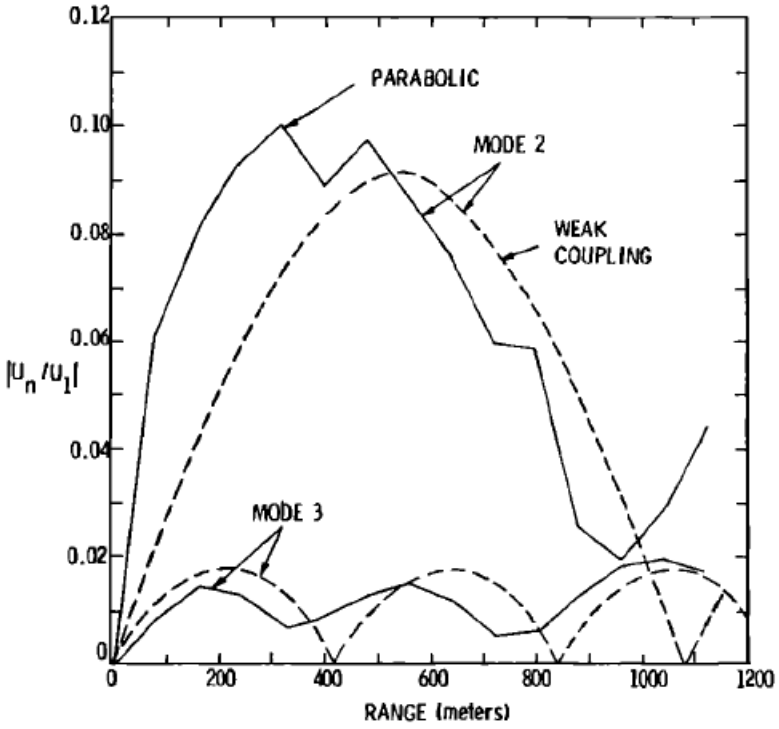

FIG. 8. Comparison of parabolic split step and weak coupling results.

Figure 4.55: Results are taken from [24]

represent a energy relation in modes 2 and 3 relatively to energy in the first mode. We can recall that the SI is based on an averaged ratio between the energy in higher and lower modes, for example, in the case of only 3 excited modes SI is equal to averaged value of the Mcdaniel result (Fig.4.55). The average of two oscilating outputs will be oscillating too.

We investigated here more complicated cases with a relatively large number of modes, yet the principle of SI as a ratio between energy in higher and lower modes remains the same, therefore McDaniel results are relevant and provide an additional support for the results in Fig.4.53, 4.54.

We compared also different attenuation cases. We found that the bottom attenuation values will have a negligible effect on SI performances (4.5). The results are shown in Fig.4.56.

Presented above results supply additional quantitative support for our previous assumptions and conclusions and they are very useful in defining optimal conditions for the depth discrimination process. We can state that for an efficient use of the SI method in the range-dependent environment a receiver/ source geometry has to satisfy upslope conditions so the watercolumn depth value at the receiver location will be higher than at the source location. Range separation of 3.5-7.0 km between the two will provide more accurate estimate concerning a category of the target (surface/ submerged).

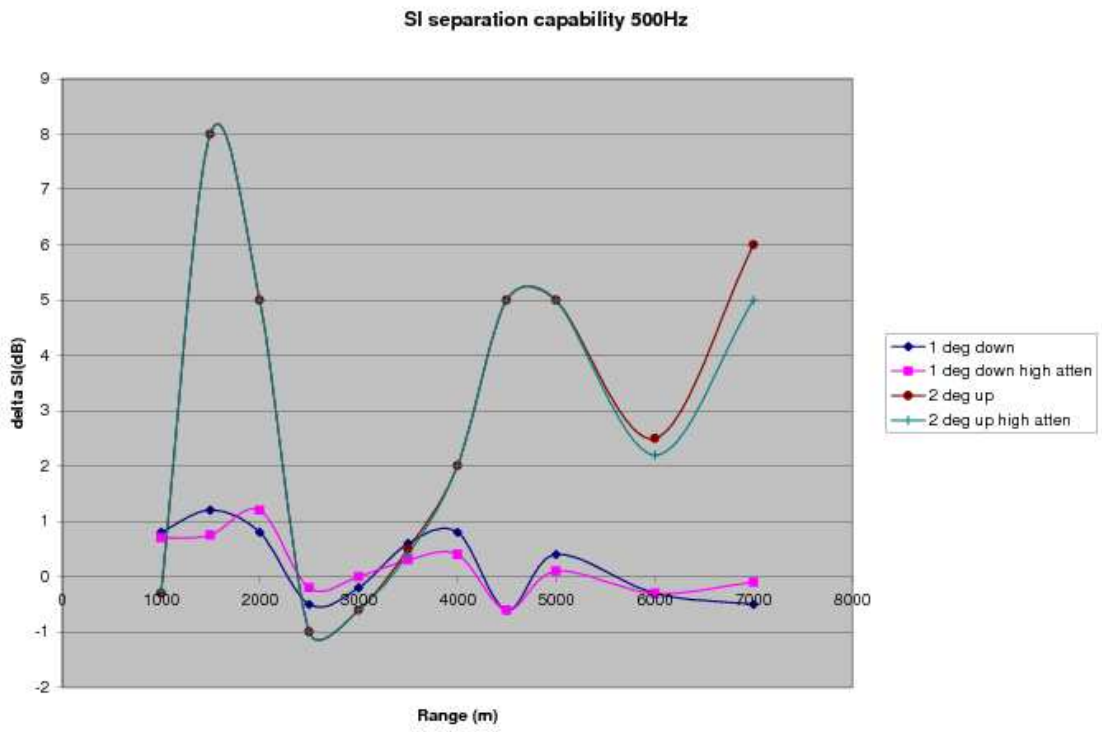

Figure 4.56: SI separation capabilities,high to low bottom attenuation comparison, 500Hz source

Chapter 5

Summary and Conclusions

In this work we examined a specific approach to the classification of sources. It is based on the angle distribution of the energy excited by a source in a shallow water environment. We were interested mainly to establish a method of a depth discrimination for sources with frequencies up to 1kHz for a typical summer soundspeed profile (Monterey Bay) . The method was applied for an array towable by an AUV . Two environmental cases were studied. The first was a range-independent case for which the OASES (wavenumber integration) propagation model was used. The second, range-dependent case, was examined using the RAM (PE) propagation model.

By modal decomposition of the pressure field we found a strong dependence of lower mode energy on a source location. Simulation results identified a relatively small contribution of low modes in the pressure field excited by a surface source. Based on this connection a general method of a depth discrimination has been suggested[28]. The method relies on a relation between normal modes and plane wave representation of the field, so the low modes can be described as plane waves with shallow propagation angles. The new concept of Submergence Index (SI) is defined as a ratio between the energy in the low and high propagation angles and uses it to classify a source as a surface or a submerged target.

We learned that SI value can be used as an indicator for a target's depth location. Although we found that the initial SI method is generally stable and robust enough for a target depth discrimination process, some additional considerations are required. From a range-independent case analysis we found that a low angle's subspace should be defined by modal energy concentrated in the first 30% of a trapped modes' total energy for optimum depth discrimination performances. A target should be located at end-fire of the array to provide the most accurate estimation. However, bearing angles of up to 20 degrees can be considered as relevant cases to apply the SI method.

Probably the most surprising outcome of the range-independent case study was a discovery of 'shadow' areas. Array allocation at such areas can't assure success of the standard SI procedure and actually can provide misleading results. To overcome this obstacle we suggested two alternatives to improve robustness of the SI procedure. We showed that by increasing a watercolumn sampling resolution in depth, the SI procedure will be improved even in the 'shadow' areas. The second approach can be even more efficient from a time and computational resources optimization point of view. We found that by sampling not only different depth levels at a fixed range but also by slightly changing range's value for each sampling, and by averaging the samplings, SI capabilities can be fully restored. We also explored a mechanism of a 'shadow' areas creation by using pressure field modal analysis for these areas. As a result of a destructive inter-modal interference, areas of pressure characterized by sufficiently depressed high modes can be found in the watercolumn. This mechanism can unbalance a modal energy distribution and cause an SI method to fail.

The range-dependent case was the most interesting and important part of the research. We found good correlation with our preliminary assumptions concerning a slope presence impact on SI capabilities. We concentrated our efforts in two source frequencies: 500Hz and 1kHz. We showed that for a downslope case is extremely difficult to find an array position that produce reliable SI results. Even for a mild downslope of a half degree the SI simulation results were unstable. However, the upslope scenario presented sufficient stability. Therefore from a practical point of view, a presence of the slope demands array allocation in deeper areas of the ocean than a receiver. This finding should guide the development of concepts for autonomous

distributed systems.

Although a preference of an upslope environment is obvious, methods for improvement of SI capabilities in downslope environment can be considered as a future goals of the research.The performance in these cases may be improved by an increase in depth sampling resolution, as was the case in the range-independent case. It can be also useful to compare efficiency of every suggested SI modification for a range-independent case in combination with AUV hydrodynamic behavior simulation. This will allow us to estimate the efficiency in light of overall system performances.

Bibliography

[1] E.C. Shang, "Source depth estimation in waveguides", J. Acoust. Soc. Am. 77(4): 1413-1418, 1985.

[2] T.C. Yang, "A method of range and depth estimation by modal decomposition", J. Acoust. Soc. Am. 82(5): 1736-1745, 1987.

[3] Homer P. Bucker, "Use of calculated sound fields and matched field detection to locate sound sources in shallow water", J. Acoust. Soc. Am. 59(2): 368-373, 1976.

[4] A.B. Baggeroer, W.A. Kuperman, Henrik Schmidt, "Matched field processing:Source localization in correlated noise as an optimum parameter estimation problem", J. Acoust. Soc. Am. 83(2): 571-587, 1988.

[5] Michael B. Porter "The KRAKEN normal mode program". SACLANT ASW Research Centre, La Specia, Italy, 1991.

[6] L.M. Brekhovskikh, Yu.P. Lysanov, Fundamentals of Ocean Acoustics, Springer-Verlag,2nd edition, 1991

[7] Harish M. Chouhan, G.V. Anand, "A new technique of acoustic mode filtering in shallow sea", J. Acoust. Soc. Am. 89(2): 735-744, 1991

[8] Finn B. Jensen, Henrik Schmidt, "Spectral decomposition of PE fields in a wedge-shaped ocean", In Progress in Underwater Acoustics, Ed. H.M. Merklinger, Plenum Press, 1987

[9] Ching-Sang Chiu, "Downslope modal energy conversion", J. Acoust. Soc. Am. 95(3): 1654-1657, 1994

[10] C.B. Officer, "Introduction to the Theory of Sound Transmission With Application to the Ocean", McGRAW-HILL, 1958

[11] M. Abramowitz, I.A. Stegun, "Handbook of Mathematical Functions", US Gov. Printing Office, 1972

[12] G. Strang, "Introduction to Applied Mathematics", Wellesley-Cambridge, 1987

[13] George V. Frisk, "Ocean and Seabed Acoustics", Prentice-Hall, 1994

[14] G. Arfken, "Mathematical Methods for Physicists", Academic Press, 1985

[15] Henrik Schmidt, "OASES. Version 3.1.User Guide and Reference Manual", MIT, 2004.

[16] Henrik Schmidt, A.B. Baggeroer, W.A. Kuperman, E.K. Scheer, "Environmentally tolerant beamforming for high-resolution matched field processing: Deterministic mismatch", J. Acoust. Soc. Am. 88(4): 1851-1862, 1990.

[17] A.V. Oppenheim, R.W. Schafer, J.R. Buck, "Discrete-Time Signal Processing", Prentice Hall, 1999

[18] J.G. Proakis, D.K. Manolakis, "Digital Signal Processing", Prentice Hall, 1996.

[19] F.J. Harris, "On the Use of Windows for Harmonic Analysis with the Discrete Fourier Transform", Proc. IEEE, Vol.66, 51-84, 1978

[20] A.H. Nutall, "Some Windows with Very Good Sidelobe Behavior", IEEE Trans. on Acoustics, Speech, and Signal Processing, Vol. 29, 84-91, 1981

[21] S.L. Tantum, L.W. Nolte, "On array design for matched field processing", J. Acoust. Soc. Am. 107(4): 2101-2111, 2000.

[22] R.B. Evans "A coupled mode solution for acoustic propagation in a waveguide with stepwise depth variations of a penetrable bottom", J. Acoust. Soc. Am. 74(1): 188-195, 1983.

[23] F.B. Jensen, W.A. Kuperman "Sound propagation in a wedge-shaped ocean with a penetrable bottom", J. Acoust. Soc. Am. 67(5): 1564-1566, 1980.

[24] S.T. McDaniel "Mode coupling due to interaction with the seabed", J. Acoust. Soc. Am. 72(3): 916-923, 1982.

[25] C.T. Tindle, H. Hobaek, T.G. Muir "Downslope propagation of normal modes in a shallow water wedge", J. Acoust. Soc. Am. 81(2): 275-286, 1987.

[26] T.W. Yudichak, G.S. Royal, D.P. Knobles, M. Gray, R.A. Koch and S.A. Stotts "Broadband modeling of downslope propagation in a penetrable wedge", J. Acoust. Soc. Am. 119(1): 143-152, 2006.

[27] A.L. Maggi, A.J. Duncan "AcTUP v.2.2l. Acoustic toolbox. User interface and post-processor. Installation and user guide", Curtin University of Technology, Centre for Marine Science and Technology, 2006.

[28] Henrik Schmidt "Distributed acoustic sensing in shallow water", 152 Meeting of ASA, Honolulu, Hawaii, December 2006.